



STATION DESIGN REPORT

Document number..... SKA-TEL-LFAA-0300034
Context AL-PPP
Revision.....0.7
Author E. de Lera Acedo et al.
Date 2018-10-30
Document Classification
Status Released

INTELLECTUAL PROPERTY DISCLAIMER

The design work described in this document was performed by the authors as members of the LFAA consortium contributing to the SKA project and is subject to the SKA IP policy.

TABLE OF CONTENTS

1	INTRODUCTION.....	12
1.1	Purpose of the document	12
1.2	Scope of the document	12
1.3	Structure of the document	12
1.4	Status of the document.....	13
1.5	Authorship of the document.....	13
1.5.1	Main authors	13
1.5.2	Main contributors to the document and work	13
2	REFERENCES.....	14
2.1	Applicable documents.....	14
2.2	Reference documents	15
3	DEFINITIONS	19
3.1	The SKA1-LOW field station	19
4	COMPLIANCE WITH REQUIREMENTS	21
4.1	SKA1-LFAA_FN_REQ-195 Antenna spacing.....	21
4.2	SKA1-LFAA_FN_REQ-123 Antennas per field node	21
4.3	SKA1-LFAA_FN_REQ-196 Distribution of collecting area within field nodes.....	21
4.4	SKA1-LFAA_FN_REQ-197 Field Station Effective Diameter	22
4.5	SKA1-LFAA_FN_REQ-132 Field Node sensitivity	22
4.6	SKA1-LFAA_FN_REQ-133 Sensitivity for off zenith angles	23
4.7	SKA1-LFAA_FN_REQ-120 Cross polarisation purity	24
4.8	SKA1-LFAA_MCCS_REQ-89 Aperture Array DDE	24
5	DESIGN OF THE ARRAY STATION.....	25
5.1	Antenna element design	25
5.2	Sparse random array	25
5.2.1	Sparse random array layout algorithm	26
5.2.1.1	Final optimization.....	28
5.3	Mutual coupling	29
5.4	Sidelobes and Gratinglobes.....	32
5.4.1	Alternative configurations.....	33
5.5	The 512 SKA1-LOW stations.....	36
6	EM MODELING	43
6.1	Commercial codes	44
6.2	HARP.....	44
6.2.1	Meshing SKALA4 in HARP and comparison with commercial codes	45
6.2.1.1	Single element validation	46
6.2.1.2	Small array validation	47
6.2.1.3	SKA1-LOW station validation.....	48
6.2.1.4	Further validation.....	49
7	STATION PERFORMANCE.....	54

7.1	Sensitivity	54
7.2	Beams.....	58
7.2.1	Mutual coupling, beams and nulling	62
7.2.2	Mutual coupling and array size	63
7.2.3	Polarization and IXR	66
7.3	Sub-station beams.....	71
7.3.1	Spatial Smoothness and array beam modelling and predictability (AAVS1)	76
7.3.2	Smoothness of the Embedded Patterns (AAVS1 and SKALA4).....	78
7.3.2.1	Deviation from idealized pattern	78
7.3.2.2	The first derivative	81
7.3.2.3	Modelling of the Embedded Element Patterns.....	81
7.4	Budget of mechanical tolerances on the EM performance.....	87
7.4.1	Rotational alignment between polarisations	87
7.4.2	Vertical alignment	88
7.4.3	Feed gap deviation	89
7.4.4	Distance to ground.....	91
7.4.5	Wire diameter deviation	92
7.4.6	Conclusions	93
7.5	Array tolerances	93
7.5.1	Rotational misalignment between antennas	93
7.5.2	Rotational misalignment between antennas	97
7.5.3	Calibration uncertainties in the amplitude and phase of the weights	98
7.6	Ground plane and APIU/station box effects	106
7.7	Impact of antenna and TPM failures	107
7.7.1	Failing antennas and Tile Processing Module	107
7.7.2	Tile/group of 16 antennas belonging to a TPM.....	108
7.7.3	Cumulative TPM fails.....	112
7.7.4	Random failing antennas.....	113
7.7.4.1	Random failing 13 antennas (5% of a station).....	113
7.7.4.2	Random failing 16 antennas.....	114
7.7.4.3	Random failing 26 antennas (10% of a station).....	115
7.7.4.4	Random failing 64 antennas (25% of a station).....	115
7.7.4.5	Summary table and effect on sensitivity.....	115
8	MEASUREMENTS OF THE PROTOTYPE ARRAYS.....	117
8.1	AAVS0/Pre AAVS1	117
8.1.1	UAV measurements	120
8.1.2	Satellite measurements.....	125
8.1.3	Direct coupling measurements	127
8.1.3.1	Other measurements	128
9	LAYOUTS.....	129

LIST OF FIGURES

Figure 1: Example of a SKA1-LOW field station antenna layout.....	20
Figure 2. SKALA4 prototype at Lords Bridge, Cambridge, UK.....	20
Figure 3: A/T for increasing distance between antennas in an array (d) – left – and average sky brightness temperature across frequency [ref] – right-.....	26
Figure 4: Example of regular vs irregular array. Effect of side lobes.	26
Figure 5: Example of an SKA-LOW random station (left) and the corresponding histogram of minimum antenna spacing (right).	28
Figure 6: Element position grid on left, self-correlation between antenna positions on right	28
Figure 7: Final station layout with keep out zones (left) and maximum correlation over runs (right)	29
Figure 8: Example array factor in dB (not including mutual coupling - [RD13]) of the station before and after optimisation.....	29
Figure 9: Mutual coupling effects on the active S_{11} for infinite regular arrays and finite random arrays.....	30
Figure 10: Mutual coupling effects on the active reflection coefficient of a given element in a pseudo random array and comparison to the passive active reflection coefficient.	31
Figure 11: Mutual coupling effects on the embedded element patterns and comparison to the isolated element pattern in a pseudo random array. The error is calculated as the single element pattern minus the mean element patterns at each angle.	31
Figure 12: Mutual coupling effects on the array pattern of a pseudo random array and comparison to the case without mutual coupling (just the array factor). “MBF (Macro Basis Function) + Baselines” here refers to the simulation including mutual coupling.....	32
Figure 13: Different array configurations and the resulting beams for a zenith scan.	34
Figure 14: Scan Array Temperature for different station configurations.	35
Figure 15: Scan sensitivity for different station configurations.	35
Figure 16: A cut of the typical expected SKA1-LOW station beam incorporating the SKALA response at 100 MHz and 200 MHz. The dotted lines show the transition region from dense to sparse. SLL is the side lobe level and CS stands for coherent section.	36
Figure 17: Comparison between 5 different layouts (different instances of the random layout generator) at 4 different frequencies showing clear differences in the side lobe area.	37
Figure 18: Comparison between 512 different layouts (different instances of the random layout generator) at 4 different frequencies showing clear differences in the side lobe area.	37
Figure 19: Plots showing the all-sky coverage of the Stokes-I element beam (left column), the cross-power station beam for a single baseline (middle column), and the average cross-power station beam for the whole instrument (right column) at 50 MHz (top row), 110 MHz (middle row) and 350 MHz (bottom row).	39
Figure 20: FSSN time scaling from 10 seconds to 8 hours using natural visibility weighting for 6 observation frequencies using (a) un-apodised and (b) apodised stations. Error bars show the 1-sigma variation between 6 pointings. Straight lines represent estimated thermal noise.	40
Figure 21: FSSN time scaling from 10 seconds to 8 hours using uniform visibility weighting for 6 observation frequencies using (a) un-apodised and (b) apodised stations. Error bars show the 1-sigma variation between 6 pointings. Straight lines represent estimated thermal noise.	41
Figure 22: FSSN frequency scaling for a 17702 second (~ 5 hour) observation, for both unapodised station beams (circular symbols) and apodised station beams (square symbols), imaged using natural visibility weighting (solid lines/empty symbols) and uniform visibility weighting (dashed lines/filled symbols). The dotted lines show the estimated thermal noise for the observation. Error bars are drawn to show the 1-sigma variation between the 6 simulated pointings.....	42
Figure 23: Example of the effect of weighting in the station beam.	43

Figure 24: Feeding point details of the HARP mesh (1 polarization).....	45
Figure 25: Feeding point details of the HARP mesh (2 polarizations).	45
Figure 26: SKALA4.1 HARP mesh.....	46
Figure 27: Comparison of beams between HARP and FEKO across frequency.	47
Figure 28: Pre-AAVS1 array with SKALA4.	48
Figure 29: Comparison of the beam between FEKO and HARP at 150 MHz for a 16 element array of SKALA4 antennas.....	48
Figure 30: Comparison of embedded element patterns calculated using HARP and the commercial code FEKO at 3 frequencies: 95 MHz (top), 220 MHz and 350 MHz (bottom). These are shown for an element at the edge of the array (left column) and at the center of the array (right column).	49
Figure 31: AAVS1 configuration.....	50
Figure 32: Embedded element pattern of a central element in AAVS1 (see element position in the AAVS1 layout above) at different frequencies as simulated by HARP (left column) and error pattern wrt to the commercial code WIPL-D (right column).....	51
Figure 33: Array pattern cuts at different frequencies as simulated by HARP and the commercial code WIPL-D.	53
Figure 34: Comparison of the simulated AAVS1 array pattern at 110 MHz scanned at zenith and at 30 degrees with HARP and the commercial code WIPL-D.....	53
Figure 35: Zenith directivity for a SKA1-LOW station.	54
Figure 36: Station directivity across the field of view.	56
Figure 37: Calculated effective area at zenith for a SKA1-LOW station (left) and system temperature (right). Boxes indicating the dense (purple), dense-sparse (orange) and sparse (light blue) regions are shown.	56
Figure 38: Zenith sensitivity for a SKA1-LOW station: (a) full bandwidth, (b) dense regime, (c) sparse regime.	57
Figure 39: Station sensitivity contour maps at several frequencies (averaged between the 2 polarizations).....	58
Figure 40: Embedded element pattern beams at multiple frequencies (all patterns in the station). Also shown, the mean of all the EEPs (thick dark red and blue lines) and also the cuts for the isolated element (thin light red and blue lines).	59
Figure 41: EEPs and Standard deviation of the embedded element pattern beams at multiple frequencies (all patterns in the station), 2 nd polarization.	60
Figure 42: Full EEP of an element in a SKA1-LOW station (absolute value) in dB and normalized to the maximum (160 MHz).....	61
Figure 43: Phase of EEP of an element in a SKA1-LOW station with respect to the center of the station (horizontal (left) and vertical (right) components of the field) in degrees (160 MHz)..	61
Figure 44: Phase of EEP of an element in a SKA1-LOW station with respect to the center of the antenna (horizontal (left) and vertical (right) components of the field) in degrees (160 MHz).62	62
Figure 45: Station beams with and without mutual coupling included at 4 different frequencies.....	62
Figure 46: Nulling with SKA1-LOW station accounting for mutual coupling when the main beams is scanned off zenith.	63
Figure 47: 16 element array (mean embedded pattern (left) and standard deviation (right) of all the patterns in the array in dB).	64
Figure 48: 256 element array (mean embedded pattern (left) and standard deviation (right) of all the patterns in the array in dB).	64
Figure 49: Embedded patterns in dB for 2 individual antennas in a 16 element array (left) and 256 element array (right) at 200 MHz.....	65

Figure 50: Convergence of the effects of mutual coupling for different number of elements in the array (of increasing size) and an increasing radius of influence (radius of the area around each individual antenna in where the effects of mutual coupling are accounted for). The error across the whole sky of the station beam is shown here..... 65

Figure 51: Station IXR at 50 MHz. The grey line marks 45 degrees. The solid black line marks the 15 dB IXR requirement. The red dot marks the point of minimum IXR within the +/- 45 deg. cone from zenith..... 66

Figure 52: Station IXR at 80 MHz. The grey line marks 45 degrees. The solid black line marks the 15 dB IXR requirement. The red dot marks the point of minimum IXR within the +/- 45 deg. cone from zenith..... 67

Figure 53: Station IXR at 110 MHz. The grey line marks 45 degrees. The solid black line marks the 15 dB IXR requirement. The red dot marks the point of minimum IXR within the +/- 45 deg. cone from zenith..... 68

Figure 54: Station IXR at 220 MHz. The grey line marks 45 degrees. The solid black line marks the 15 dB IXR requirement. The red dot marks the point of minimum IXR within the +/- 45 deg. cone from zenith..... 69

Figure 55: Station IXR at 350 MHz. The grey line marks 45 degrees. The solid black line marks the 15 dB IXR requirement. The red dot marks the point of minimum IXR within the +/- 45 deg. cone from zenith..... 70

Figure 56: Station IXR across frequency. Minimum and average values within the field of view (+/- 45 deg cone from zenith) are shown. It is worth noting that the minimum vales always occur at the edge of the field of view but not at the same point at every frequency. Also shown is the minimum IXR if a simple polarization diversity algorithm is applied to the antenna’s rotational positions [RD37]. For comparison the IXR values for the isolated element are also shown..... 71

Figure 57: Sub-station configurations analyzed in this section..... 72

Figure 58: Sub-station beams at 50 MHz. The different colors represent the different configurations presented in **Figure 57**..... 73

Figure 59: Sub-station beams at 110 MHz. The different colors represent the different configurations presented in **Figure 57**..... 74

Figure 60: Sub-station beams at 220 MHz. The different colors represent the different configurations presented in **Figure 57**..... 75

Figure 61: Sub-station beams at 350 MHz. The different colors represent the different configurations presented in **Figure 57**..... 76

Figure 62: Station beam (in log-log scale) and model..... 77

Figure 63: Station beam scanned at zenith; exact and modeled with different orders..... 77

Figure 64: Station beam scanned at 30 degrees from zenith; exact and modeled with different orders..... 78

Figure 65: Example of average EEP at 120 MHz..... 79

Figure 66: Pattern smoothness metric for the first element of the AAVS1 SKALA2 Array at 120 MHz. The scale of the two upper axes is E^2 , where E is the E-field pattern. The different colors identify the various azimuth angles..... 80

Figure 67: Histograms of the $q_i\theta, \varphi$ data for the first AAVS1 element (left) and all elements (right).80

Figure 68: Histograms for the gradient of an analytical dipole placed at $\lambda/4$ from an infinite conducting ground (left) and for the Average Embedded Element Pattern of the AAVS1 array at 120 MHz (right)..... 81

Figure 69: Antenna active region moving with frequency..... 83

Figure 70: Complex spherical harmonics functions (Image credit: Mathworks)..... 84

Figure 71: Complex spherical harmonics full sky beam reconstruction error wrt to real beam (for different orders of decomposition)..... 85

Figure 72: Full sky station beam scanned at zenith (110 MHz) in dB. 85

Figure 73: Error of the reconstructed station beam using spherical harmonic models of the embedded patterns or order 5 with respect to the full sky station beam scanned at zenith (110 MHz) in dB. 86

Figure 74: Error of the reconstructed station beam using spherical harmonic models of the embedded patterns or order 10 with respect to the full sky station beam scanned at zenith (110 MHz) in dB. 86

Figure 75: View of the misalignment angle from above..... 87

Figure 76: Effect of a +/- 1 degree rotational misalignment between polarizations of the antenna on the zenith directivity (left) and the minimum IXR within the field of view (right) across frequency. Absolute deviations are shown. 87

Figure 77: Effect of a +/- 1 degree rotational misalignment between polarizations of the antenna on the S11 (left) and the absolute deviation of S11 (right) across frequency..... 88

Figure 78: Side view of the vertical misalignment angle. 88

Figure 79: Effect of a +/- 1 degree vertical misalignment on the zenith directivity (left) and the minimum IXR within the field of view (right) across frequency. Absolute deviations are shown. 89

Figure 80: Effect of a +/- 1 degree vertical misalignment on the S11 (left) and the absolute deviation of S11 (right) across frequency..... 89

Figure 81: View of the feed gap from above. 90

Figure 82: Effect of a 1mm deviation in the feed gap of the antenna (inwards) on the zenith directivity (left) and the minimum IXR within the field of view (right) across frequency. Absolute deviations are shown. 90

Figure 83: Effect of a 1mm deviation in the feed gap of the antenna (inwards) on the S11 (left) and the absolute deviation of S11 (right) across frequency..... 90

Figure 84: Side view of the distance to ground tolerance..... 91

Figure 85: Effect of a +/- 2 cm variation on the distance to ground on the zenith directivity (left) and the minimum IXR within the field of view (right) across frequency. Absolute deviations are shown. 91

Figure 86: Effect of a +/- 2 cm variation on the distance to ground on the S11 (left) and the absolute deviation of S11 (right) across frequency..... 92

Figure 87: Side view of the one the wire arms..... 92

Figure 88: Effect of a 1mm deviation in the wire thickness on the zenith directivity (left) and the minimum IXR within the field of view (right) across frequency. Absolute deviations are shown. 93

Figure 89: Effect of a 1mm deviation in the wire thickness on the S11 (left) and the absolute deviation of S11 (right) across frequency..... 93

Figure 90: Effect of antenna rotations on the station's IXR. 94

Figure 91: Percentage difference in measured Stokes I source flux for a randomly polarised source at the phase centre. 95

Figure 92: Percentage difference in measured Stokes I source flux for a source polarised with 50% Stokes Q at the phase centre. 95

Figure 93: Percentage difference in measured Stokes Q source flux for a randomly polarised source at the phase centre. 96

Figure 94: Percentage difference in measured Stokes Q source flux for a source polarised with 50% Stokes Q at the phase centre. 97

Figure 95: Effect of antenna vertical positions on the station's IXR at 3 different frequencies. All antennas same position (left column) and random variations up to 10 cm (right column)..... 98

Figure 96: Effects of unaccounted phase and amplitude errors in the array beam (normalized directivity). Errors: 5%, 10% and 15% at 3 different frequencies: 100 (top), 200 and 350 (bottom) MHz.....	99
Figure 97: Effects of unaccounted phase and amplitude errors in the array beam (normalized directivity). Errors: 10%, 20% and 30% at 3 different frequencies: 100 (top), 200 and 350 (bottom) MHz.....	101
Figure 98: Example of 50 simulated E-field station beams for unaccounted phase errors equivalent to 0.1 STDEV. Frequency = 50 MHz.....	102
Figure 99: Example of 50 simulated E-field station beams (normalized) for unaccounted phase errors equivalent to 0.1 STDEV. Frequency = 50 MHz.	103
Figure 100: Statistical impact of unaccounted phase errors (as a function of the standard deviation of the error) in the main beam and maximum SLL. Field beams at frequency = 50 MHz.	104
Figure 101: Statistical impact of unaccounted phase errors (as a function of the standard deviation of the error) in the main beam and maximum SLL. Field beams at frequency = 350 MHz.	105
Figure 102: 64-element array directivity at 4 different frequencies (50, 110, 220 and 350 MHz) for different ground plane configurations. The added extensions to the circular ground planes are radial (eg. 1 m extension means 1 m radially).....	106
Figure 103: 256-element array directivity at 3 different frequencies (95, 220 and 350 MHz) for different ground plane configurations and also including the station boxes.....	107
Figure 104: Station antenna coordinates (in m). Antennas belonging to TPM 15 are shown in red.	108
Figure 105: Station antenna coordinates (in m). Antennas belonging to TPMs 0-14 (top left to bottom right) are shown in red.	109
Figure 106: Station E-field beam (in dBV/m) at 50 MHz (top row), 110 MHz, 220 MHz and 350 MHz (bottom row) for no failing TPMs (left column), failing TPM 0 (central column) and failing TPM 8 (right column).	110
Figure 107: Station E-field beam cuts (in dBV/m) at 50 MHz (top row), 110 MHz, 220 MHz and 350 MHz (bottom row) for a $\phi = 0$ deg. cut and a $\phi = 90$ deg. Cut and the different TPMs failing individually. Zoom of the side lobe region.	112
Figure 108: Station E-field beam cuts (in dBV/m) at 50 MHz (top row), 110 MHz, 220 MHz and 350 MHz (bottom row) for a $\phi = 0$ deg. cut and a $\phi = 90$ deg. Cut and a cumulative number of TPMs failing (0, 1, 5, 9, 13).	113
Figure 109: Loss of effective area for 13 random antennas failing. Simulations performed for an AAVS1 station (35m in diameter).	114
Figure 110: Loss of effective area for 16 random antennas failing. Simulations performed for an AAVS1 station (35m in diameter).	114
Figure 111: Loss of effective area for 26 random antennas failing. Simulations performed for an AAVS1 station (35m in diameter).	115
Figure 112: Loss of effective area for 64 random antennas failing. Simulations performed for an AAVS1 station (35 m in diameter).	115
Figure 113: Loss of sensitivity for a single station for an increasing number of failing antennas. Zenith.	116
Figure 114: Loss of sensitivity for a single station for an increasing number of failing antennas. 45 deg. scan.....	117
Figure 115: AAVS0/PreAAVS1 array at Lords Bridge (MRAO, Cambridge, UK).....	118
Figure 116: RFI waterfall plot at Lords Bridge (MRAO, Cambridge, UK).....	119
Figure 117: AAVS0 receiver system (top) and PRRADU rack (bottom).....	120
Figure 118: (left) UAV flying over the preAAVS1 array (SKALA-2 antennas), deployed at the Mullard Radio Astronomy Observatory, Lords Bridge, Cambridge. (right) Array geometry of both AAVS0 and preAAVS1.....	121

Figure 119: PreAAVS1 array (beam) patterns at 50 MHz (left) and 350 MHz (right).....	122
Figure 120: Embedded-element patterns of the central element (#5) of the pre AAVS1 array. Two different scans are shown for each measurement plane: E-plane (left, TW1 and TW2) and H-plane (right, TW3 and TW4).	122
Figure 121: Reconstructed (blue curve) and simulated phase (red curve) of y-component of the AUT near-field along the UAV trajectory.	123
Figure 122: Radiation pattern measurements of an isolated SKALA-2. A (black) and B (magenta) refer to the two antenna ports. Measurements are shown with circular markers, simulations are shown with dashed line. (left) 50 MHz (right) 350 MHz.....	124
Figure 123: Measurement and simulation of a AAVS0 beam cut (with and without phase calibration).	124
Figure 124: Measurement and simulation of the 2D AAVS0 array beam when scanned at zenith...	125
Figure 125: Spectra for a NOAA satellite pass. The signal itself is a 256-level amplitude modulated 2400Hz subcarrier, which is then frequency modulated onto the 137 MHz-band RF carrier. Maximum subcarrier modulation is 87% ($\pm 5\%$), and overall RF bandwidth is 34 kHz. On NOAA POES vehicles, the signal is broadcast at approximately 37dBm (5 watts) effective radiated power.	126
Figure 126: Array beam and satellite data (CASSIOPE satellite). Left column: power spectrum before (top) and after (bottom) Doppler correction, Central column: Satellite pass over the simulated array beam (top) and beam cut measured (blue line) and simulated with 2 different solvers (red and green lines) (bottom), Right column: satellite position (top) an distance to the array (bottom).	126
Figure 127: 2D Array beam measured with multiple CASSIOPE satellite passes.....	127
Figure 128: AAVS0 array configuration for coupling measurements.	127
Figure 129: Measured vs simulated coupling using commercial (CST) and in-house (HARP) codes.	128

LIST OF TABLES

Table 1: SKA1-LOW Field Station main parameters.....	19
Table 2: Antenna spacing requirement.	21
Table 3: Antennas per field node requirement.	21
Table 4: Distribution of collecting area within field nodes.	22
Table 5: Field Station Effective Diameter.	22
Table 6: Field Node sensitivity.	23
Table 7: Field Node sensitivity.	24
Table 8: Cross polarization purity.	24
Table 9: Aperture Array DDE.	24
Table 10: RMS error – spatial smoothness for a set of frequencies and 2 different scan angles (zenith and 45 degrees).	77
Table 11: RMS of histograms for all the elements of AAVS1 array.....	81
Table 12: Maximum gradient of the average Embedded Element Pattern of the AAVS1 array. The reference value from the analytical solution is equal to 1 at all frequencies.	81
Table 13: Number of Spherical Harmonic coefficients 3:10, 12 and 15, at 5 different frequencies. The average error across the sky is in dB.	84
Table 14: Percentage difference in measured Stokes I source flux for a randomly polarised source at the phase centre.	95
Table 15: Percentage difference in measured Stokes I source flux for a source polarised with 50% Stokes Q at the phase centre.	95
Table 16: Percentage difference in measured Stokes Q source flux for a randomly polarised source at the phase centre.	96
Table 17: Percentage difference in measured Stokes Q source flux for a source polarised with 50% Stokes Q at the phase centre.	96
Table 18: Approximate effect of unknown random position/phase errors on the array sensitivity.	105

LIST OF ABBREVIATIONS

AADC	Aperture Array Design and construction Consortium
AAVS	Aperture Array Verification System
ASTRON	Netherlands Institute for Radio Astronomy
AL	Antenna and LNA
CCL	Cambridge Consultants
CDR	Critical Design Review
EM	Electromagnetic
FN	Field Node
ICRAR	International Centre for Radio Astronomy Research
IEIIT	Institute of Electronics, Computer and Telecommunications Engineering
INAF	Italian National Institute for Astrophysics
LFAA	Low Frequency Aperture Array
LINFRA	Local Infrastructure
LNA	Low Noise Amplifier
LST	Local Sidereal Time
MBF	Macro Basis Function
RD-N	nth document in the list of Reference Documents
RFoF	Radio Frequency over Fibre
RX	Receiver
SKA	Square Kilometre Array
SKA-LOW	SKA low frequency part of the full telescope
SKALAN	nth version of the SKA Log-periodic Antenna
SKAO	SKA Office
TBC	To Be Confirmed
TBD	To Be Determined
UCAM	University of Cambridge
WP	Work Package

1 Introduction

1.1 Purpose of the document

This document describes the electromagnetic design of the SKA1-LOW field station and its compliance to requirements.

1.2 Scope of the document

The SKA1-LOW field station is inscribed in a circular area having an effective station diameter (centre-to-centre [AD3]) of 38 meters and has 256 SKALA4 elements [RD2]. This document describes the electromagnetic design of the field station. In particular it describes the layout design and the electromagnetic modelling and characteristics of the station. This document describes the effects associated with the layout and array such as mutual coupling effects, side lobe pattern and beam shape (eg. smoothness, calibration models) and presents the state of the art of our ability to measure the array performance and validate the simulation work.

The current LFAA field node requirements [AD4], derived from the SKA L1 requirements [AD2], have evolved over the last years since the LFAA PDR [RD5] and the System Baseline Design [RD6]. The SKA1-LOW field station has been designed to meet those requirements and has therefore tracked their evolution (eg. sensitivity requirements, array diameter, etc.).

The aforementioned requirements represent a very tight space with a desire for very high sensitivity over a large frequency range (7:1) and wide field of view (+/- 45 degrees cone from zenith) while keeping the station diameter to a minimum, so as the filling factor but at the same time allowing for sufficient space between antennas to allow for easy maintenances, amongst many others. This results in a complex design.

The description of the individual components of the field station (eg. antennas, LNAs, etc.) and the non-functional and architectural aspects of the field station are described in the Field Node Detailed Design Document [RD3]. This document deals exclusively with the electromagnetic design of the station.

1.3 Structure of the document

After this introduction, and the references and definitions sections, Section 4 describes the compliance of the design with the latest L2 requirements, and where relevant, non-compliances are explained and discussed. The relevant sections of the document where the data is presented and discussed are linked from this first section.

Section 5 then describes the design of the station focusing on the type of layout (pseudo-random as indicated by the SKA requirements) and the rationale about mutual coupling effects in this type of phased arrays.

Section 6 is one of the core sections of this document and deals with the description of the methods and results for the prediction of the station's performance. This section is especially relevant since it informs other work [RD4] related to the station calibration amongst others.

Section 7 is dedicated to describing the main performance metrics of the station including its sensitivity to tolerances and other errors such as calibration errors. This section includes a description of low order beam models for both stations and embedded patterns. This again is quite important since being able to represent these beams accurately and with a low number of coefficients is key for the calibration of the instrument.

Finally section 8 presents a summary of the main tests carried out with the array demonstrator at Lords Bridge, Cambridge UK, in order to validate the simulation work and show our ability to predict the array's performances. This again is one of the key sections since it supports and validates the simulation and modelling work presented in here.

Section 9 presents the location of the main data presented in the document.

1.4 Status of the document

The array station and antenna design have been tightly coupled. The antenna design is described in [RD3]. Through the lifetime of the project, the log-periodic antenna developed for SKA1-LOW has also evolved, with the latest version (SKALA4) been developed since the summer of 2017 after the antenna selection process [RD7][RD8][RD9]. The development plan for SKALA4 is presented in [RD10]. While the majority of the station simulations and performance predictions have been done with the latest SKALA4 design, some results presented in here are for the AAVS1 station (using SKALA2 antennas) due to time constraints. Also, while SKALA4 has improved over SKALA2 in many aspects (passband smoothness, sensitivity, polarization, less response towards the horizon, etc), the 2 versions of SKALA are very similar in terms of their performance in the array environment. Those instances where the simulations have been carried out for the AAVS1 station are clearly indicated in the text and justified.

1.5 Authorship of the document

1.5.1 Main authors

Lead author: Eloy de Lera Acedo (Cambridge University).

Co-authors: Hardie Pienaar (Cambridge University), Nima Razavi Ghods (Cambridge University).

1.5.2 Main contributors to the document and work

Jens Abraham (ex Cambridge University), Edgar Colin-Beltran (ex Cambridge University), Ben Mort (Oxford University), Fred Dulwich (Oxford University), Giuseppe Virone (IEIT), Benedetta Fiorelli (ex ASTRON), Michiel Arts (ASTRON), Christophe Craeye (UcL Belgium), Bui van Ha (UcL Belgium), Keith Grainge (University of Manchester).

1.5.3 Other contributors to the document

Peter Dewdney (SKAO), Jeff Wagg (SKAO), Maria Grazia Labate (SKAO), Andrew Faulkner (Cambridge University), Jan Geralt bij de Vaate (ASTRON), Marchel Gerbers (ASTRON).

2 References

2.1 Applicable documents

The following documents are applicable to the extent stated herein. In the event of conflict between the contents of the applicable documents and this document, **the applicable documents** shall take precedence.

ID	Title	Code	Issue
[AD1]	SKA1 Level 0 Science Requirements	SKA-TEL-SKO-0000007	2
[AD2]	SKA PHASE 1 SYSTEM REQUIREMENTS SPECIFICATION	SKA-TEL-SKO-0000008	11
[AD3]	SKA1-LOW CONFIGURATION COORDINATES – COMPLETE SET	SKA-TEL-SKO-0000422	3
[AD4]	Field Node Requirements Specification	SKA-TEL-LFAA-0200036	

2.2 Reference documents

The following documents are referenced in this document. In the event of conflict between the contents of the referenced documents and this document, **this document** shall take precedence.

ID	Title	Code	Issue
[RD1]	SKA1-LOW Antenna Evaluation Criteria	SKA-TEL-SKO-0000800	D
[RD2]	LFAA Architectural Design and Analysis Report	SKA-TEL-LFAA-0200028	
[RD3]	Field Node Detailed Design Document	SKA-TEL-LFAA-0200038	
[RD4]	LFAA Demonstrator Test Report	SKA-TEL-LFAA-0800001	
[RD5]	LFAA PDR document set		
[RD6]	SKA1 System Baseline Design	SKA-TEL-SKO-0000002	
[RD7]	SKA1-LOW antenna selection document		
[RD8]	SKA1-LOW antenna selection – panel report		
[RD9]	SKA1-LOW antenna candidates		
[RD10]	Antenna development plan	SKA-TEL-LFAA-0300033	
[RD11]	B. Florelli, et al. “Polarization analysis and evaluation for radio astronomy aperture array antennas”, EuCAP 2013		
[RD12]	SKA1-LOW antenna design document	SKA-TEL-LFAA-0300031	
[RD13]	Phased Array Antennas, R. C. Hansen, Wiley.		
[RD14]	SKA Science book, www.skatelescope.org		
[RD15]	N. Razavi et al., “Analysis of sky contributions to system temperature for low frequency SKA aperture array geometries”, Experimental Astronomy 2012.		
[RD16]	C. Thibault et al., “A Global-Local Synthesis Approach for Large Non-Regular Arrays”, IEEE TAP 2014.		
[RD17]	G. Mellema et al., “Reionization and the Cosmic Dawn with the Square Kilometre Array”, Experimental Astronomy 2013.		
[RD18]	E. de Lera Acedo et al. “SKA aperture array verification system: electromagnetic modelling and beam pattern measurements”, Experimental Astronomy 2018.		
[RD19]	D. Gonzalez-Ovejero et al., “Non-periodic arrays for radio-astronomy applications”, IEEE APS 2011.		
[RD20]	B. Mort et al. “Analysing the impact of far-out side-lobes on the imaging performance of the SKA-LOW telescope”, MNRAS 2016.		
[RD21]	E. de Lera Acedo et al., “Ultra-Wideband Aperture Array Element Design for Low Frequency Radio Astronomy”, IEEE TAP 2011.		

[RD22] E. de Lera Acedo et al., "SKALA, a log-periodic array antenna for the SKA-low instrument: design, simulations, tests and system considerations", Experimental Astronomy 2015.		
[RD23] A. El-Makadema et al., "Geometry Design Optimization of Large-Scale Broadband Antenna Array Systems", IEEE TAP 2014.		
[RD24] X-array tool (http://www.mrao.cam.ac.uk/~nima/xarray_dist16/XarrayTool.pdf)		
[RD25] OSKAR (https://github.com/OxfordSKA/OSKAR)		
[RD26] D. Buisson and N. Razavi, "Amplitude weighting of irregular planar arrays: Minimising near-in and intermediate sidelobes", ICEAA 2015.		
[RD27] CST, www.cst.com		
[RD28] FEKO, www.altair.com		
[RD29] WIPL-D, www.wipl-d.com		
[RD30] D. Gonzalez-Ovejero and C. Craeye, "Interpolatory Macro Basis Functions Analysis of Non-Periodic Arrays", IEEE TAP 2011.		
[RD31] Ha Bui-Van et al., "Fast and Accurate Simulation Technique for Large Irregular Arrays", IEEE TAP 2017.		
[RD32] M. Ivashina et al., "Equivalent System Representation to Model the Beam Sensitivity of Receiving Antenna Arrays", IEEE TAP 2008.		
[RD33] E. de Lera Acedo et al., "Spectral performance of SKA Log-periodic Antennas I: Mitigating spectral artefacts in SKA1-LOW 21-cm cosmology experiments", MNRAS 2017.		
[RD34] S. Ellingson, LWA memo 147 " https://www.faculty.ece.vt.edu/swe/lwa/memo/lwa0147.pdf "		
[RD35] Ha Bui-Van et al., "Direct Deterministic Nulling Techniques for Large Random Arrays Including Mutual Coupling", IEEE TAP 2018.		
[RD36] T. Carozzi and G. Woan, "A Fundamental Figure of Merit for Radio Polarimeters", IEEE TAP 2011.		
[RD37] H. Pienaar et al., "Practical Polarisation Diversity for a Sparse Aperture Array Station", ICEAA 2018.		

[RD38] S. J. Wijnholds, "Substantiation of LFAA L1 calibration requirements", internal LFAA document, 2015.		
[RD39] E. de Lera Acedo et al., "Compact Representation of the Effects of Mutual Coupling in Non-regular Arrays Devoted to the SKA Telescope", ICEAA 2011.		
[RD40] Ha Bui-Van et al., "Main Beam Modeling for Large Irregular Arrays The SKA1-LOW telescope case", Experimental Astronomy 2017.		
[RD41] R. Lehmsiek and D. I. L de Villiers, "Constant Radiation Characteristics for Log-Periodic Dipole Array Antennas", IEEE TAP 2014.		
[RD42] B. Fiorelli and E. de Lera Acedo, "Polarization Performance of the SKA Low Frequency Aperture Array Station", ICEAA 2014.		
[RD43] A. Sutinjo and P. Hall, "Intrinsic Cross-Polarization Ratio of Dual-Linearly Polarized Antennas for Low-Frequency Radio Astronomy", IEEE TAP 2013.		
[RD44] A. Sutinjo et al., "Characterization of a Low-Frequency Radio Astronomy Prototype Array in Western Australia", IEEE TAP 2015.		
[RD45] G. Pupillo et al., "Medicina array demonstrator: calibration and radiation pattern characterization using a UAV-mounted radio-frequency source", Experimental Astronomy 2015.		
[RD46] F. Paonessa <i>et al.</i> , "The UAV-based test source as an end-to-end verification tool for aperture arrays," <i>2016 International Conference on Electromagnetics in Advanced Applications (ICEAA)</i> , Cairns, QLD, 2016.		
[RD47] G. Virone, et al., "Antenna pattern measurements with a flying far-field source (hexacopter)," IEEE International Conference on Antenna Measurements and Applications, Nov. 16-19 2014, Antibes Juan-les-Pins, France.		
[RD48] P. Bolli, et al. "Antenna pattern characterization of the low-frequency receptor of LOFAR by means of an UAV-mounted artificial test source," <i>SPIE Ground-based and Airborne Telescopes VI</i> , Edinburgh, United Kingdom, June 2016.		
[RD49] L. Ciorba et al., "Near-Field Phase Reconstruction for UAV-based Antenna Measurements" submitted to EuCAP 2019.		

[RD50] Rui Cao et al., "All-Digital Beam Forming for SKAI-LOW: CTPM Design and Verification", IEEE MTT-S 2018.		
[RD51] C. Raucy et al., "Characterization of SKA-AA low antenna elements in the array environment", ICEAA 2012.		
[RD52] B. Fiorelli and E. de Lera Acedo, "On the simulation and validation of the Intrinsic Cross-Polarization Ratio for antenna arrays devoted to low frequency radio astronomy", EuCAP 2014.		

3 Definitions

3.1 The SKA1-LOW field station

A SKA1-LOW field station represents the collection of 256 antennas forming a phased aperture array. A field station has the following main parameters (table 1).

Parameter	Value
Antenna element	SKALA4 (see Figure 2)
Field Station shape	Circular
Effective station diameter (D1)*	38 m (max. from centre to centre)
Clearance station diameter (D2)*	40 m
Ground-plane station diameter (D3)*	42 m
Number of antennas	256
Field Station layout	Pseudo-random (see Figure 1)
Average distance between antennas within a station (centre to centre)	2.1 m (assuming a square footprint per antenna)
Minimum distance between antennas within a station (centre to centre)	1.7 m
Minimum width of the path that should allow access to each antenna (at least one free path for each antenna)	≥ 0.7 m

* Definitions available in [AD4].

Table 1: SKA1-LOW Field Station main parameters.

In Figure 1 a sample of a field station layout is presented. The outer black thick line represents the ground plane perimeter (corresponding to a diameter D3) and the black thin line represents the effective station perimeter (corresponding to a diameter D1). The 5 red dots represent the location of the 4 APIUs and the Field Node Distribution Hub (FNH, the red dot in the centre). The FNH has now been moved to the outside edge of the field station. This change has been done after the EM simulations for the station were started, however we don't expect any significant impact on the electromagnetic performance of the field station due to this change of position. The grey circles represent the positions of the antennas (they do not represent the footprint of the antenna).

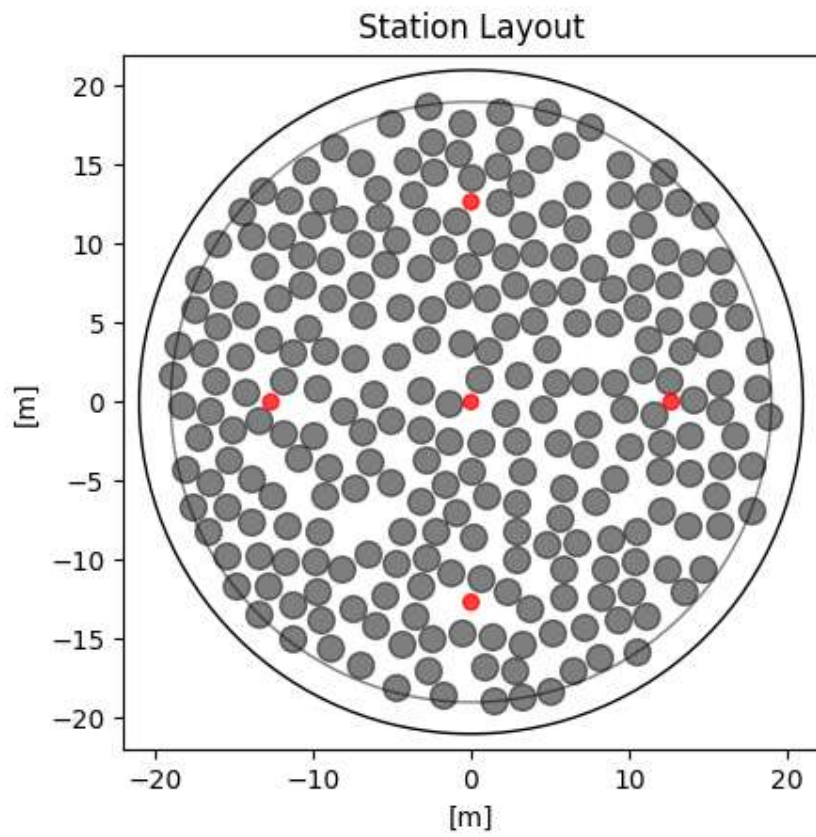


Figure 1: Example of a SKA1-LOW field station antenna layout.



Figure 2. SKALA4 prototype at Lords Bridge, Cambridge, UK.

4 Compliance with requirements

In this section the L3 requirements for the FN that have been identified as directly related to the electromagnetic station design are presented. Compliances are explained.

4.1 SKA1-LFAA_FN_REQ-195 Antenna spacing

Requirement definition	"The average spacing between antenna elements within a Field Station shall be the same for each of the LFAA Field Stations."
Date of requirement	07/24/2018
Verification	Analysis
Compliance	Compliant
Relevant sections in the document	3.1, 5.2, 5.5
Comments	The average spacing between antennas is determined by the layout generation and limited by the station diameter (equal for all stations) and the number of antennas per station (equal for all stations).

Table 2: Antenna spacing requirement.

4.2 SKA1-LFAA_FN_REQ-123 Antennas per field node

Requirement definition	"The number of antennas in each Field Node shall be 256."
Date of requirement	07/25/2018
Verification	Inspection
Compliance	Compliant
Relevant sections in the document	3.1, 5.2
Comments	The number of antennas is by definition 256 and it is provided by the layout generator.

Table 3: Antennas per field node requirement.

4.3 SKA1-LFAA_FN_REQ-196 Distribution of collecting area within field nodes

Requirement definition	"Placement of antennas within each Field Station shall be independently randomised in two dimensions (within the constraints of antenna and station size) so as not to form a regular grid."
Date of requirement	07/25/2018
Verification	Analysis, Inspection
Compliance	Compliant

Relevant sections in the document	3.1, 5.2, 5.5, 9
Comments	The coordinates of the antennas are provided by the layout generator. This implements a random placement in two dimensions.

Table 4: Distribution of collecting area within field nodes.

4.4 SKA1-LFAA_FN_REQ-197 Field Station Effective Diameter

Requirement definition	"The Field Station shall have an "Effective Station Diameter" (defined in [AD8]) of 38 metres + TBD Margin."
Date of requirement	07/25/2018
Verification	Inspection
Compliance	Compliant
Relevant sections in the document	3.1, 5.2, 5.5, 9
Comments	The station diameter is enforced by the layout generator.

Table 5: Field Station Effective Diameter.

4.5 SKA1-LFAA_FN_REQ-132 Field Node sensitivity

Requirement definition	<p>"Assuming a sky noise temperature defined in the definitions section of the system requirements specification document [AD1], the whole LFAA shall have sensitivity per polarisation at zenith corresponding to the following values interpolated by a 'not-a-knot' cubic spline function and not deviating by more than $\pm 5\%$ from the spline interpolation spanning the following points:</p> <p>(0.14+TBD) m2/K at 50 MHz (0.14+TBD) m2/K at 55 MHz (0.46+TBD) m2/K at 80 MHz (1.04+TBD) m2/K at 110 MHz (1.15+TBD) m2/K at 140 MHz (1.20+TBD) m2/K at 160 MHz (1.20+TBD) m2/K at 220 MHz (1.13+TBD) m2/K at 280 MHz (1.02+TBD) m2/K at 340 MHz (1.01+TBD) m2/K at 345 MHz (1.01+TBD) m2/K at 350 MHz"</p>
Date of requirement	07/27/2018
Verification	Analysis
Compliance	Non Compliant
Relevant sections in the document	7.1
Comments	While the station sensitivity is met at the specified frequency points and substantially

	<p>improved in the most part of the frequency band, the deviation from a 'not-a-knot' cubic spline by more than $\pm 5\%$ is not. This is due to 2 main causes, firstly the nature of the LPD antenna produces spectrally slow variations when different parts of the antenna are activated (currents flowing in the dipoles with the right size for a given wavelength). Furthermore, the effects of mutual coupling, especially towards the middle of the band where the antenna is not electrically small and the distance between antennas is not too large, can slightly accentuate this effect. The deviations can go up to 25% in some parts of the band as shown in Section 7.1. Furthermore, the specific deviations strongly depend on the selection of frequency points and the number of them. In this requirement 11 unevenly spaced arbitrary points have been specified. It is however worth noting, as described later in the text, that these variations are easily modelled since they are spectrally slow variations.</p>
--	---

Table 6: Field Node sensitivity.

4.6 SKA1-LFAA_FN_REQ-133 Sensitivity for off zenith angles

Requirement definition	“The sensitivity of the Field Node shall not degrade by more than 30% at local elevation angle of 60 degrees and not by more than 50% at local elevation angle of 45 degrees for all local azimuthal angles between 0 and 360 degrees, compared to the peak sensitivity at zenith.”
Date of requirement	07/29/2018
Verification	Analysis
Compliance	Non Compliant
Relevant sections in the document	7.1
Comments	The sensitivity off zenith angles per polarization in random phased arrays is dominated by the directivity of the embedded element patterns, and in particular for the directivity of the average embedded element pattern. In order to meet the required zenith sensitivity and at the same time the required drop off sensitivity at 45 degrees, the system baseline design [RD6] assumed an antenna directivity of 8 dBi at zenith and an idealized cosine like beam, resulting in 5 dBi in all phi cuts at 45 degrees. No real antenna can achieve that over a 7:1 band and the embedded beams tend to be elliptical (as expected for dipole like antennas) resulting in an

	increased sensitivity in one direction and a reduced sensitivity in the other direction. Thus, the sensitivity at 45 and 60 degrees elevation is not 50% and 30% from zenith. However, given the already higher zenith sensitivity provided by a SKALA4 station, the 45 and 60 degrees sensitivity is also higher than the required sensitivity at those angles. Furthermore, the averaged sensitivity between the 2 polarizations has a circular symmetry and is also very close to this required drop off.
--	--

Table 7: Field Node sensitivity.

4.7 SKA1-LFAA_FN_REQ-120 Cross polarisation purity

Requirement definition	“The Field Station intrinsic cross polarisation ratio shall be at least 15 dB over the whole observing band within the half power beam width up to observing angles of 45 degrees from the zenith.”
Date of requirement	07/24/2018
Verification	Test
Compliance	Non Compliant
Relevant sections in the document	7.2.1
Comments	The IXR of the station beam is less than 15 dB at some angles within the field of view. This always occurs at the edge of the field of view due to projection effects. This is a known effect [RD11] for fixed dipole like antennas on top of a ground plane across a wide frequency band.

Table 8: Cross polarization purity.

4.8 SKA1-LFAA_MCCS_REQ-89 Aperture Array DDE

Requirement definition	“The MCCS shall have direction dependent models for the beams for each station (or sub-station) with an accuracy of 1% in amplitude and 0.1 radians in phase at the half-power points to be used in calibration and imaging.”
Date of requirement	-
Verification	-
Compliance	Compliant
Relevant sections in the document	7.3.1
Comments	Low-order models of the station beam can produce the desired accuracy wrt to the full wave simulated beam.

Table 9: Aperture Array DDE.

5 Design of the array station

5.1 Antenna element design

The electromagnetic and mechanical design of the antenna element (SKALA4) is described in [RD12] and [RD3] respectively. In this document, the design of the field station made of 256 SKALA4 elements is described. The antenna is a wideband log-periodic antenna with 16 dipoles fed with a pseudo differential LNA.

The electromagnetic design of SKALA4 took into account the fact that the antenna had to be placed in a phased array with a pseudo-random layout (see section 5.2 for more information on the layout). The main constraints to consider when designing antenna elements for a phased array in a large frequency band are:

- The antenna bandwidth vs mutual coupling effects. It is expected that mutual coupling effects will be present and to some extent noticeable in an array with the density described by Table 1 and operating over a 7:1 band. The design of the SKA1-LOW field station arrays has followed traditional engineering practices of array design. First the antenna element is designed in isolation, then it is inserted in the array, finally the design loops back to refine the design. It is also known [RD13] that the bandwidth of an antenna in an array environment is strongly related to its susceptibility to mutual coupling effects. Wide band antennas tend to support multiple current modes to allow for the wide range of operation frequencies. For the same reason they are capable of supporting currents related to mutual coupling, even in the case of a disconnected array of antennas such as the SKA1-LOW field station. The design of SKALA4 and the SKA1-LOW field station has taken into account this trade off in order to provide the desired frequency bandwidth to cover all the key science cases [RD14] and at the same time kept the effect of mutual coupling under control.
- The size of the element. The antenna's footprint has been kept to a minimum to enable access to the array for maintainability, as well as to maximize the filling factor.

5.2 Sparse random array

The SKA1-LOW field station is designed to have a pseudo-random antenna layout [AD2]. In order to overcome the increasing sky brightness temperature at lower frequencies a sparse array (distance between element typically larger than a full wavelength) can provide increasing effective aperture at low frequencies compared to a denser array (see Figure 3). Furthermore, some so-called sparse arrays proposed for the SKA result in grating lobes, which could have major consequences for such a radio astronomy instrument. Figure 4 shows the far field response of an under-sampled (0.8λ spacing) triangular lattice array, where the grating lobe (<10 dB) is pointing towards the galactic plane when the main beam is pointing off zenith to a cold patch of the sky. There is an evident contribution from the grating lobes that presents a number of calibration and signal processing challenges [RD15]. However, in the same plot we can see the same response from a pseudo random array where the grating lobe response is distributed over the visible region. This indicates an increase of the overall side lobe level as oppose to localized effects of grating lobes. The impact of this from an interferometry point of view will be discussed in section 5.5.

It is worth noting that this type of array is very similar to that use in other radio telescopes such as LOFAR LBA or LWA.

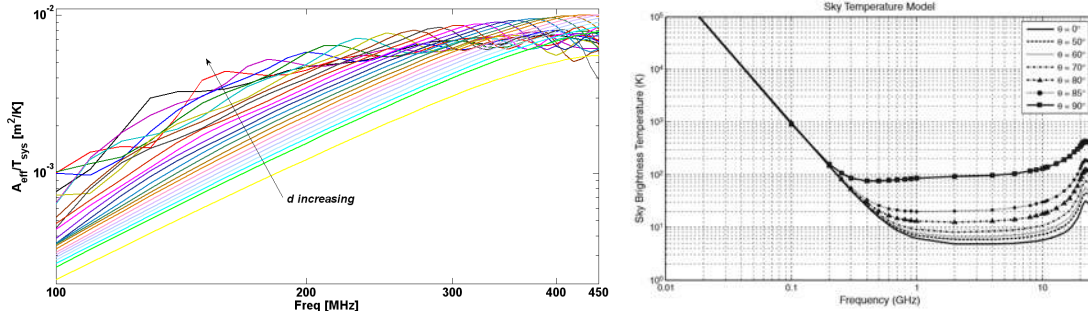


Figure 3: A/T for increasing distance between antennas in an array (d) – left – and average sky brightness temperature across frequency [ref] – right-.

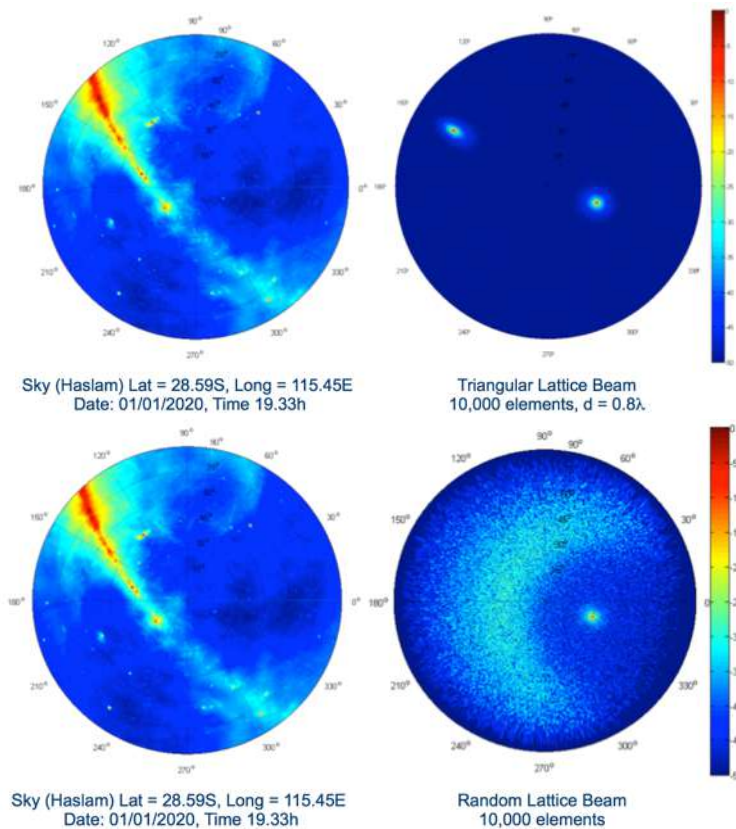


Figure 4: Example of regular vs irregular array. Effect of side lobes.

5.2.1 Sparse random array layout algorithm

As will be discussed later, one of the advantages of random arrays is that the grating lobe response in an under-sampled system such as SKA1-LOW can be disturbed in a randomised fashion. This has a direct link with the distribution of the array antenna inter-element spacings as described in [RD16]. Sparse random array configurations can be generated in a number of different ways and due to the aforementioned reason, the impact on the array performance can be startling not to mention the impact on the mutual coupling.

The first approach is to start with a regular lattice, where the location of each element is perturbed in a random fashion within a given circle around each element. Once each element is perturbed, a check can be made to ensure the new element is not closer than a specified minimum distance (d_{min})

to surrounding elements. Alternatively, if the size of the circle placed over each element for randomising its position is small, such a check is not necessary. This type of approach is generally quite simple to implement, however, the array performs poorly for a random array. The reason being that the distribution of the elements tend to have an underlying regular structure meaning that the grating lobes are not distributed into a so called “sea of sidelobes” but instead due to the regularity in the array, traditional grating lobes will form, albeit they will be averaged down due to the randomisation. It is therefore expected that if the end result is a randomised array for the sake of sidelobe distribution and averaging of mutual coupling effects, starting with a regular lattice is not an optimal choice.

The more useful approach for generating a random array is one where an element is generated within a given perimeter circle. Then another element is randomly generated and so forth. After each element is generated a minimum distance check is carried out to ensure that it does not violate that boundary. If it does, it will be discarded and another element is generated, again after which this check is performed. This approach is easy enough to implement and generally yields good results. Towards the end of the array generation run, the clashes of elements increases and so either the loop count needs to be in the thousands to ensure an array is formed or it can be done as a fixed condition. The latter can result in the algorithm not completing unless a reasonable limit is set to the number of elements generated. From experience, this tends to be 70% of the number of elements which can be packed into a regular lattice with a spacing equal to d_{min} .

Whilst generation of randomly positioned elements in a circle can yield good results, the more flexibility afforded to where the elements are positioned, the better the randomisation. The minimum distance parameter relates to the desired filling factor for a given array size [RD17]. The smaller this number is, given the physical dimensions of the antenna, the more randomised the antenna positions become. This is not only beneficial from the mutual coupling perspective but also because the positions of side-lobes would become more randomised. It is important to note, however, that since d_{min} is very much subject to the physical size of the antenna, the full benefits of randomisation cannot be explored without throwing away filling factor, and therefore brightness sensitivity as noted in [RD17]. For SKA1-LOW, the average spacing between antennas is ~2m (38m diameter with 256 antennas). To illustrate this, Figure 5 shows a typical SKA-LOW station’s random configuration (given a d_{min} of 1.6m) and the corresponding histogram of the minimum distance.

One approach to improve the randomisation of the array is for d_{min} itself to also be a random number picked within a given range of spacings. This tends to give a better spread of the minimum spacings than that shown in Figure 5. However, this will result in a reduced filling factor of the station’s aperture.

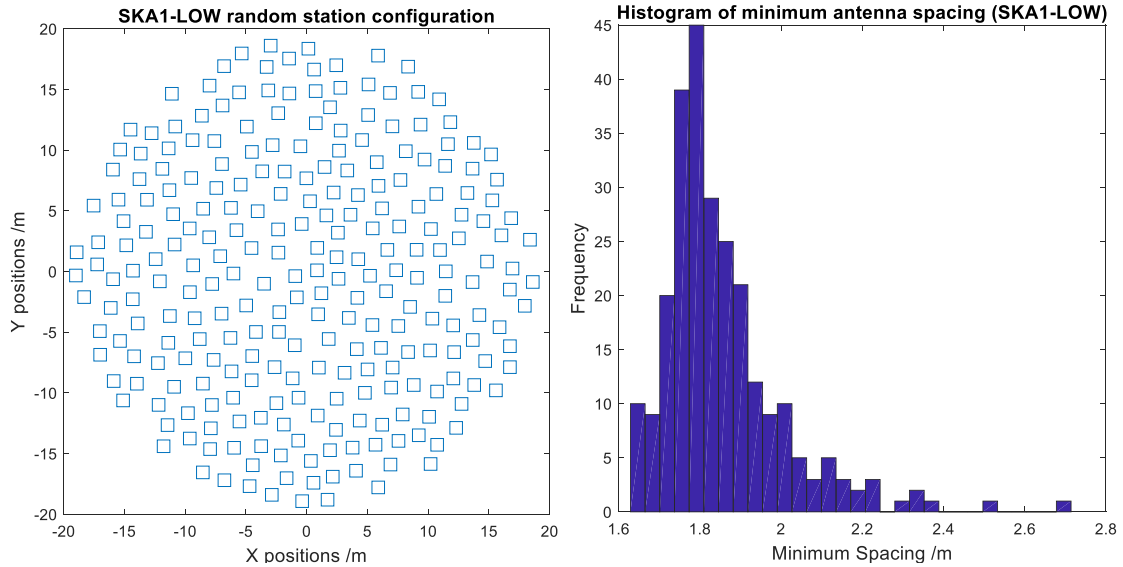


Figure 5: Example of an SKA1-LOW random station (left) and the corresponding histogram of minimum antenna spacing (right).

5.2.1.1 Final optimization

The final station layout was designed to minimise regularity in the array positions. The optimisation starts with pseudo-randomly placed elements, note that this step is not strictly necessary but certainly decreases the time that the optimisation will reach a desirable level of minimised regularity. Placing the elements randomly might form some repeating patterns between elements that the rest of the optimisation attempts to minimise. To calculate our loss function, the element positions are placed into a regular grid using a cone function. The cone function reduces the number of elements we need in the grid seen in Figure 6 (left). To measure similarity, the position grid is correlated with itself (Figure 6 right). The maximum point in the correlated grid is used as our loss function.

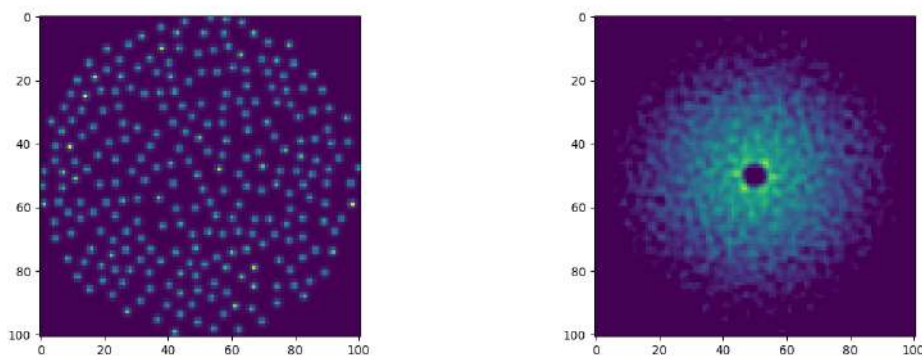


Figure 6: Element position grid on left, self-correlation between antenna positions on right

The optimiser shifts all of the element locations by a small amount while preventing antenna overlaps, keeping elements inside of the 38 m disc and keeping elements outside of the APIUs keep-out zones. The current implementation is slow and can be improved using more developed strategies such as simulated annealing and using the Jacobian to adjust element positions for the next run.

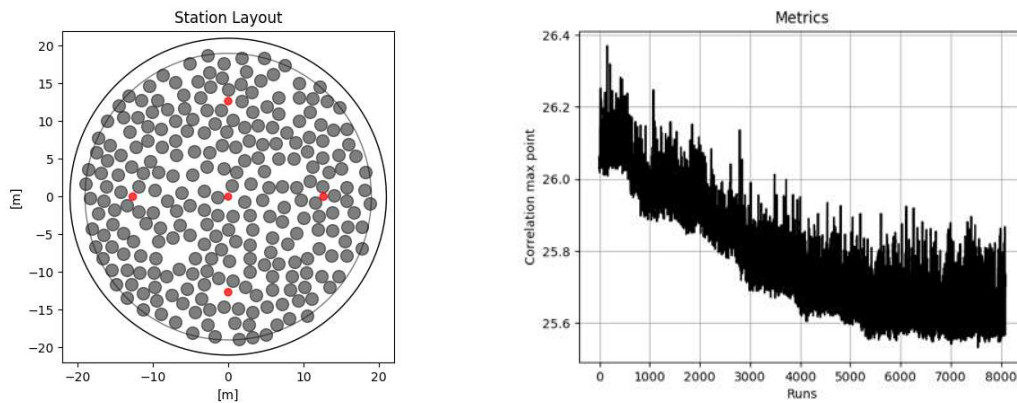


Figure 7: Final station layout with keep out zones (left) and maximum correlation over runs (right)

Figure 7 (right) shows an example of 10000 runs illustrating the convergence to a less correlated layout. This step significantly reduces the maximum 3rd and 4th side lobes (Figure 8) from the initial randomly placed layout. The final layout has a minimum inter-element distance of 1.7 m.

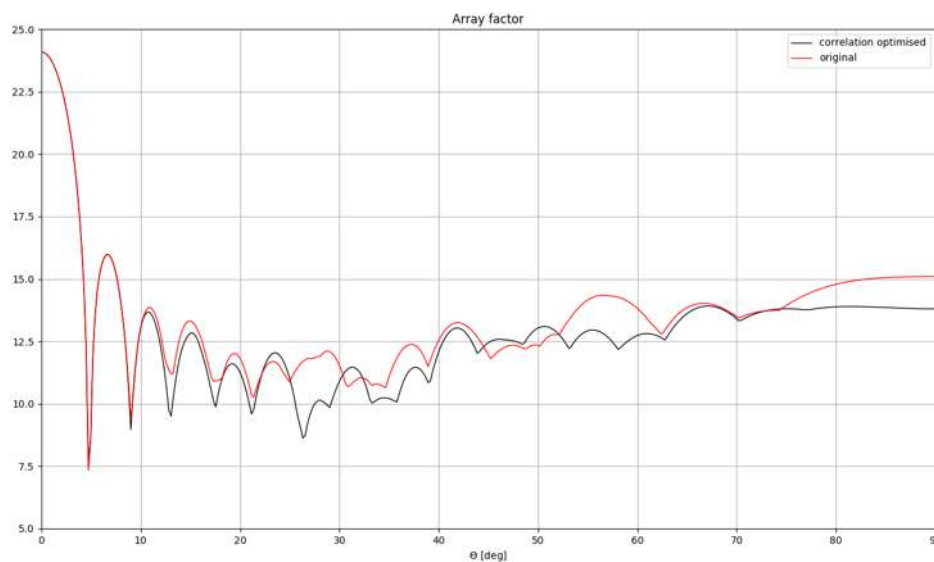


Figure 8: Example array factor in dB (not including mutual coupling - [RD13]) of the station before and after optimisation.

5.3 Mutual coupling

Mutual coupling is one of the dominant factors in phased arrays, especially in wide band phased arrays. In this section we describe the effects of mutual coupling for regular and random array layouts.

Figure 9 shows a plot of the S11 matching parameter (scattering reflection coefficient of port 1) for the antenna element embedded in an infinite regular array when all elements are active and pointing at zenith, showing clearly the type of anomalies to be expected for a sparse regular configuration. The S11 for one of the antennas in the AAVSO random array (16 elements, 8 m in

diameter) [RD18] (measured) is also displayed showing no anomalies in band. Also, only if the array configuration is randomized to mitigate the effects of mutual coupling, which are then also randomized, can the desired sensitivity be achieved. Furthermore, as mentioned above, the effects of the side lobes in irregular/randomized configurations tend to be less detrimental [RD15]. This is the type of configuration called for in the SKA1 system requirements specification [AD2] and it is the configuration being implemented in the LFAA designs.

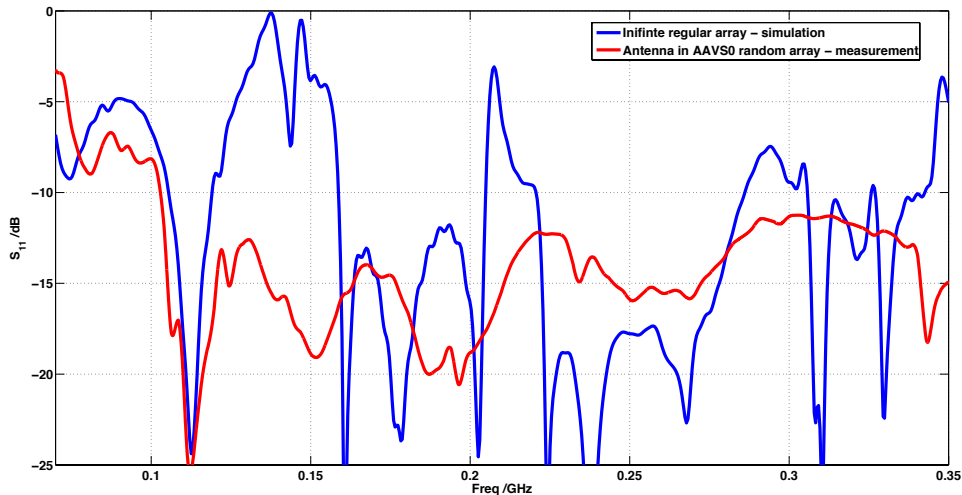


Figure 9: Mutual coupling effects on the active S_{11} for infinite regular arrays and finite random arrays.

Figure 1 showed an example of a random configuration with 38 m effective station diameter and 256 antenna elements as specified for the SKA. While sparseness is useful to obtain more sensitivity at low frequencies, in order to deliver maximum brightness sensitivity; the filling factor of the SKA core area must be as well high. In the central area all the antennas contribute to capture the relevant Fourier modes in a given angular scale. This can be pictured as all the antennas being cross-correlated to each other in an interferometric sense, so the distance between the antennas inside a station is also a baseline contributing to the total sensitivity. Therefore, a higher filling factor will maximize the information collected from the sky. This however also means that mutual coupling levels will be higher than for a sparser array.

Mutual coupling is a crucial design consideration for any antenna working in an array environment as it modifies the antenna pattern and scan impedance. In this particular case, backed up by studies of mutual coupling of irregular sparse arrays suitable for LFAA [RD19], the first design process of the array antenna was implemented used a single element. The idea behind this is that in a randomized array the mutual coupling effects tend to randomize out (see Figure 10 and Figure 11) and the array pattern can be approximated to a first order by the multiplication of the array factor and the isolated element pattern (see Figure 12). It is worth noticing however that in the calibration step, mutual coupling effects will need to be included. Mutual coupling effects are expected in the dense to sparse transition part of the band. In this central part of the band the antennas are electrically larger and can potentially support more current modes due to mutual coupling. At the same time the electrical distance between the antennas is still relatively low. Finally, it is important to note that the patterns of all the antennas in a random array (embedded element patterns) while different from each other are also static and predictable using physics-rooted models.

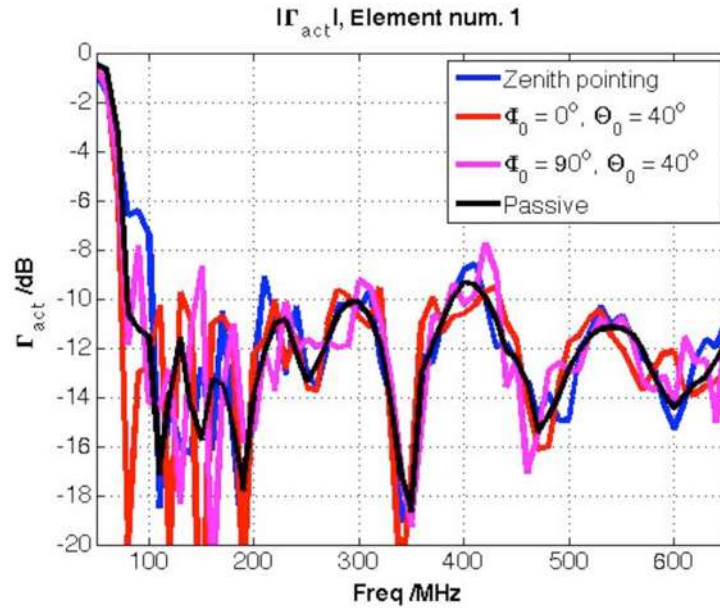


Figure 10: Mutual coupling effects on the active reflection coefficient of a given element in a pseudo random array and comparison to the passive active reflection coefficient.

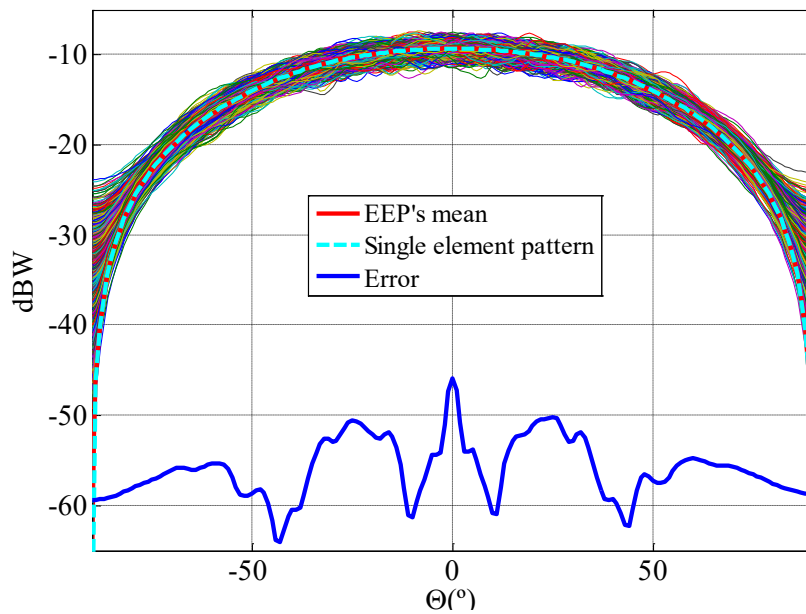


Figure 11: Mutual coupling effects on the embedded element patterns and comparison to the isolated element pattern in a pseudo random array. The error is calculated as the single element pattern minus the mean element patterns at each angle.

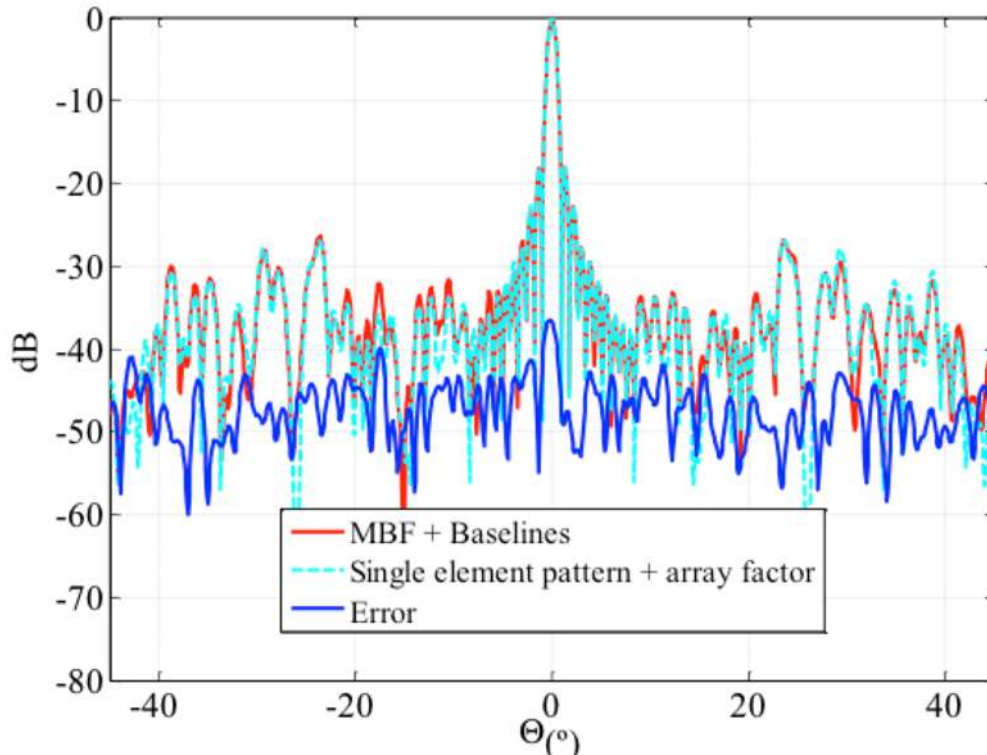


Figure 12: Mutual coupling effects on the array pattern of a pseudo random array and comparison to the case without mutual coupling (just the array factor). “MBF (Macro Basis Function) + Baselines” here refers to the simulation including mutual coupling.

5.4 Sidelobes and Gratinglobes

The configuration of the antennas in an aperture array has been an active topic of research for the past few years, with various studies conducted to determine performance parameters [RD15][RD16][RD20]. Phased array antenna systems may be implemented with regular as well as irregular geometries. The former is well understood in the literature, e.g. [RD13], especially in regards to the dense (separation $\leq \lambda/2$) and sparse (separation $> \lambda/2$) regimes where grating lobes are present.

Regular type arrays consist of not only typical regular or hexagonal lattices, but also aperiodic array types, which can range from the Danzer or Penrose tiles to the more exotic snowflake configurations. What is apparent for all such arrays is the formation of grating lobes or pseudo grating lobes when operating in the under-sampled regime. In this regime, the array behaves very much like a continuous aperture, whilst above this frequency a regular array would result in grating lobes. At a higher operating frequency where the array is sparser, the number of grating lobes increases and they also move closer to the main beam.

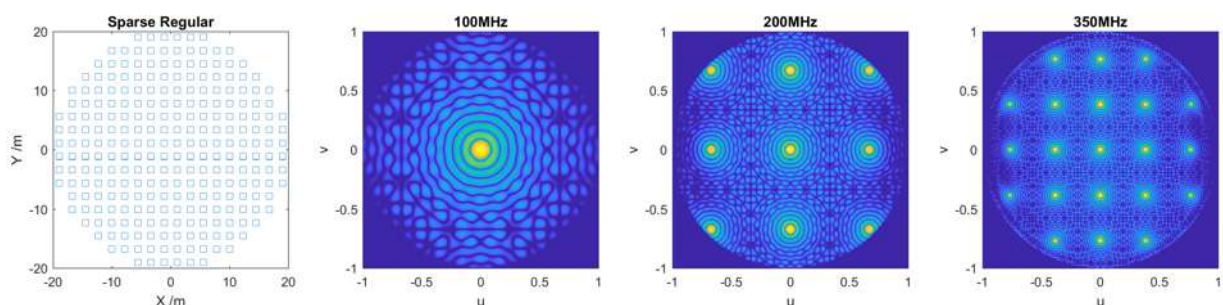
Modern wideband array antennas, such as those proposed for the SKA, may be implemented with irregular random configurations to avoid grating lobes when working in the sparse regime [RD15]. However, the power, which would form a grating lobe in a regular array, is redistributed into a broad region of weaker irregular side-lobes, which are visible at all angles known as the sea of sidelobes.

Furthermore for SKA1-LOW, in order to meet the sensitivity requirements [AD2] a sparse configuration is needed. Due to the galactic synchrotron emission dominating at the low frequencies, in order to maximise the array sensitivity without increasing the number of elements, enough space needs to be allocated to each antenna in the array so that mutual coupling does not limit their effective aperture [RD21][RD22]. Furthermore, in order to deliver maximum brightness sensitivity, the filling factor of the SKA-LOW core must be as high as possible [RD17]. As mentioned above, in the SKA1-LOW, all the individual antenna elements contribute to capture the relevant Fourier modes in a given angular scale, therefore a higher filling factor will maximize the information collected from the sky. This imposes a filling factor requirement, which sets some limits on the distance between elements and the required footprint per antenna.

5.4.1 Alternative configurations

In order to show the effects different configurations can have on the station response and thus sensitivity, six configurations are shown in Figure 13 along with their beams at 100 MHz, 200 MHz and 350 MHz. For all configurations, the grating or pseudo grating lobes are present at the higher frequencies (200 MHz and 350 MHz). Grating lobes are seen in the case of the regular array (tapered and rotated) as well as the aperiodic Penrose tiles, whilst a smoother sea of sidelobes is present in the case of the sparse random array and the golden radio spiral. The latter has been discussed in [RD23] and can offer an alternative to randomized arrays, however, such an array would require detailed modelling and calibration due to its mutual coupling behavior.

To assess the impact on array temperature and sensitivity, a number of drift scan simulations were carried out with Xarray software [RD24] at a spot frequency of 200 MHz. The purpose here was to evaluate the smoothness in both parameters if the array beam is pointing at zenith when some grating lobes were present. It should be noted that these effects would be more dramatic at higher frequencies. The results are shown in Figure 14 and Figure 15. The array temperature shows that the sparse random configuration would yield the smoothest and one of the lowest array temperatures whilst the others have many peaks and troughs. The peak at ~ 18 h LST is the galaxy passing over the array. Similarly, the scan sensitivity shows smoother response for the sparse random array and one of the highest sensitivities. Whilst Penrose tiling shows a higher level of sensitivity across most of the band, there is also a great deal of variation which is not desirable.



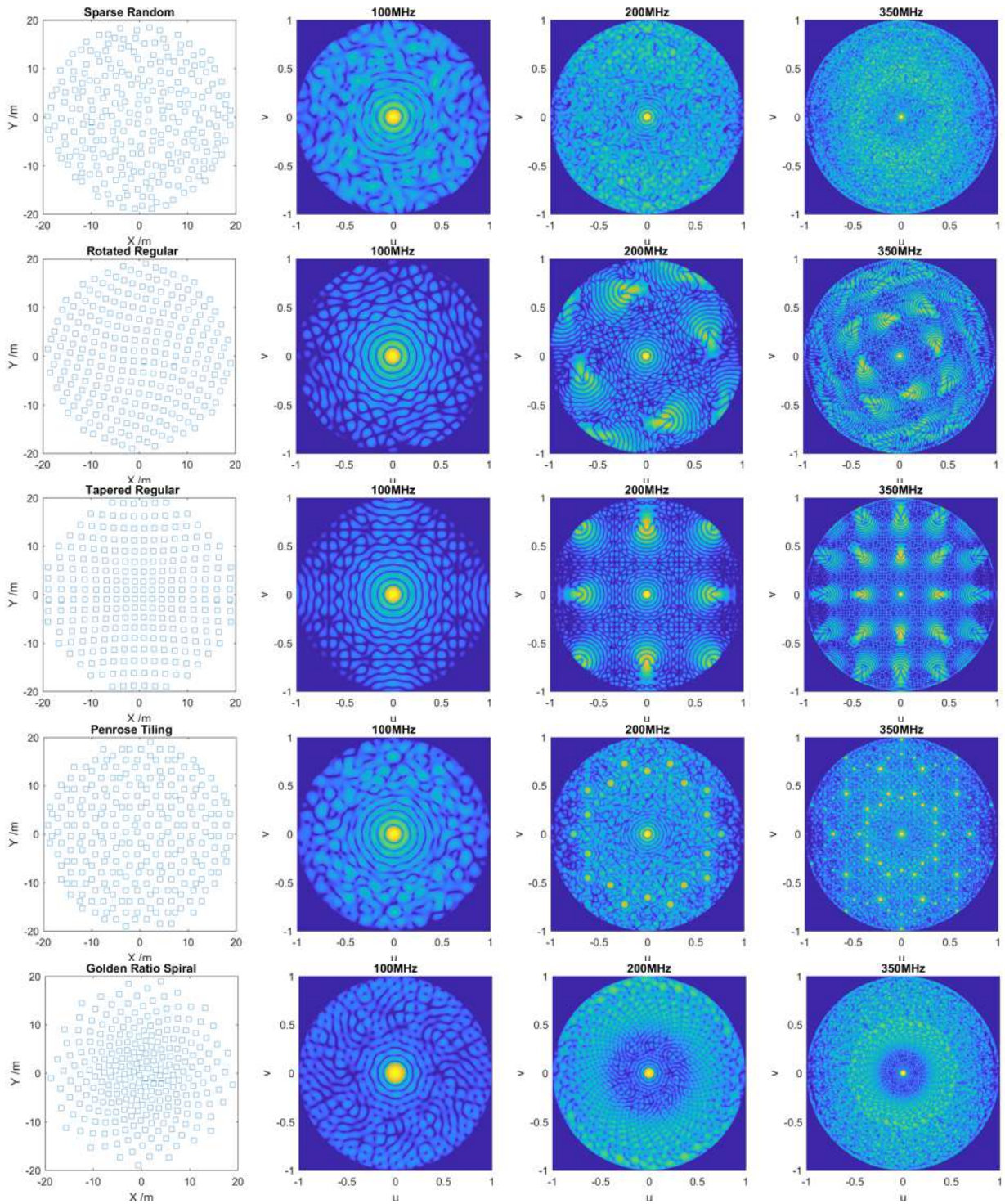


Figure 13: Different array configurations and the resulting beams for a zenith scan.

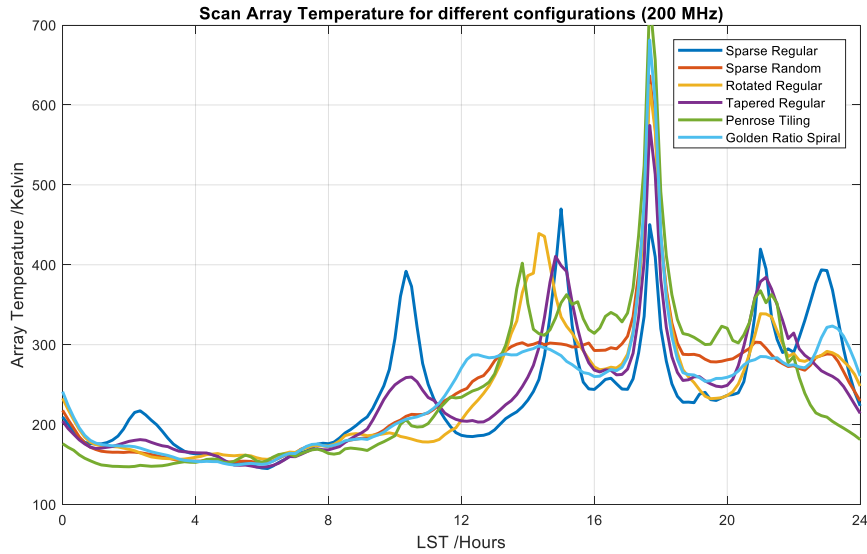


Figure 14: Scan Array Temperature for different station configurations.

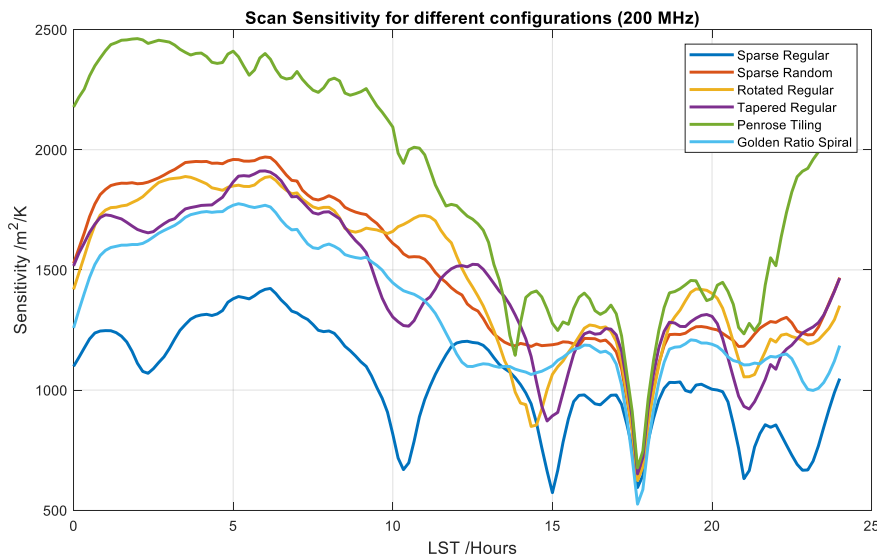


Figure 15: Scan sensitivity for different station configurations.

For these reasons, it is desirable that a sparse random array is implemented. The main difference being that the grating lobes would now exist in the form of irregularly distributed side-lobes which can be analysed by separating the array beam into so-called “coherent” and “non-coherent” regions. This terminology is described in detail in [RD16], where we estimate the boundary of this coherent to non-coherent region to appear after $\sim 0.3\sqrt{N}$ side-lobes from the main beam, and the average level of side-lobes to be given by $\sim 1/N$, where N is the number of antennas. For the SKA1-LOW telescope, where each station contains nominally 256 antennas [AD2], this transition would be ~ 5 side-lobes from the main beam (Figure 16) with the typical widths of side-lobes being $\lambda/2D$, where D is the diameter of the array. A higher operating frequency and thus more sparseness in a random array will result in this transition region appearing nearer the main beam in absolute terms. It is important to note that the side-lobe profile of each station may be different, since each station could use a different pseudo-random configuration.

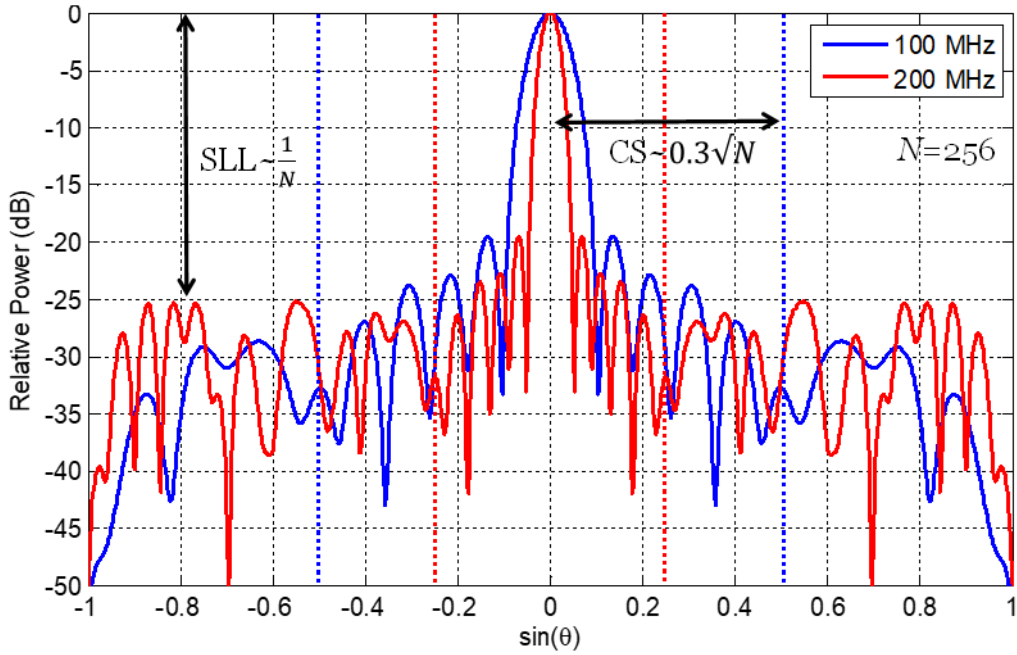
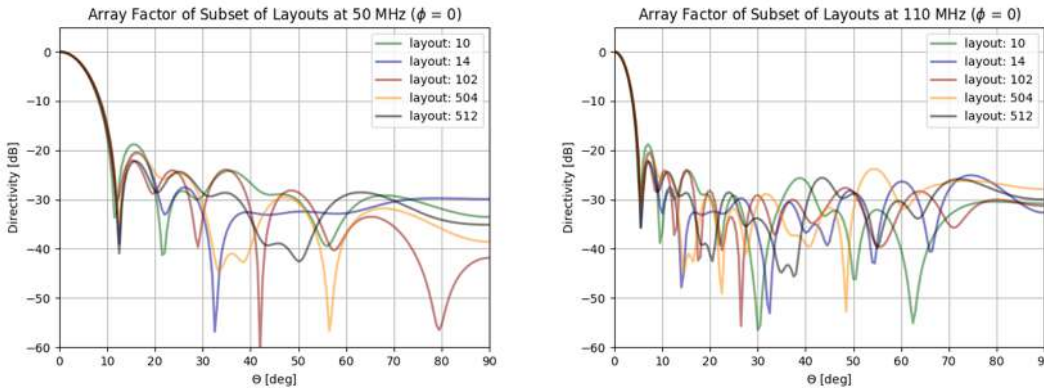


Figure 16: A cut of the typical expected SKA1-LOW station beam incorporating the SKALA response at 100 MHz and 200 MHz. The dotted lines show the transition region from dense to sparse. SLL is the side lobe level and CS stands for coherent section.

5.5 The 512 SKA1-LOW stations

In this section we described the differences and potential consequences of them between the beams of the 512 SKA1-LOW stations. In Figure 17 and Figure 18 we display the expected differences in the beam patterns of the different stations. These plots show the expected agreement in the main beam (determined by the station size and density) and clearly different side lobes (determined by the specific layout).



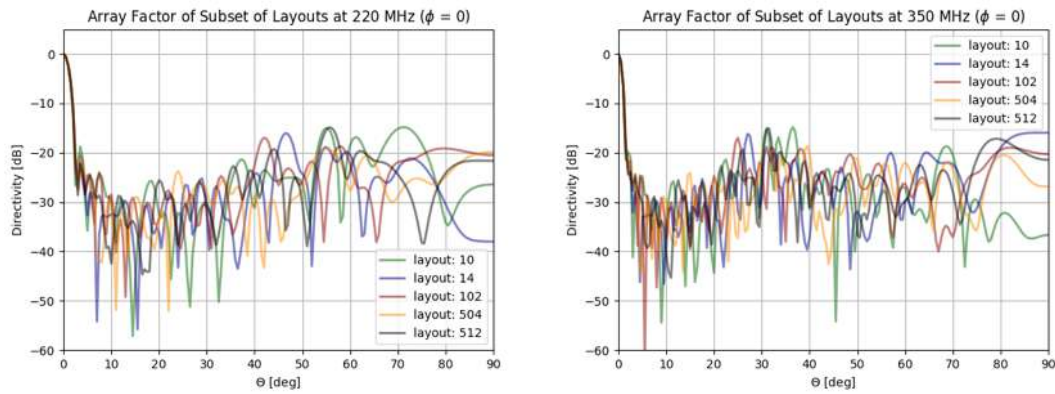


Figure 17: Comparison between 5 different layouts (different instances of the random layout generator) at 4 different frequencies showing clear differences in the side lobe area.

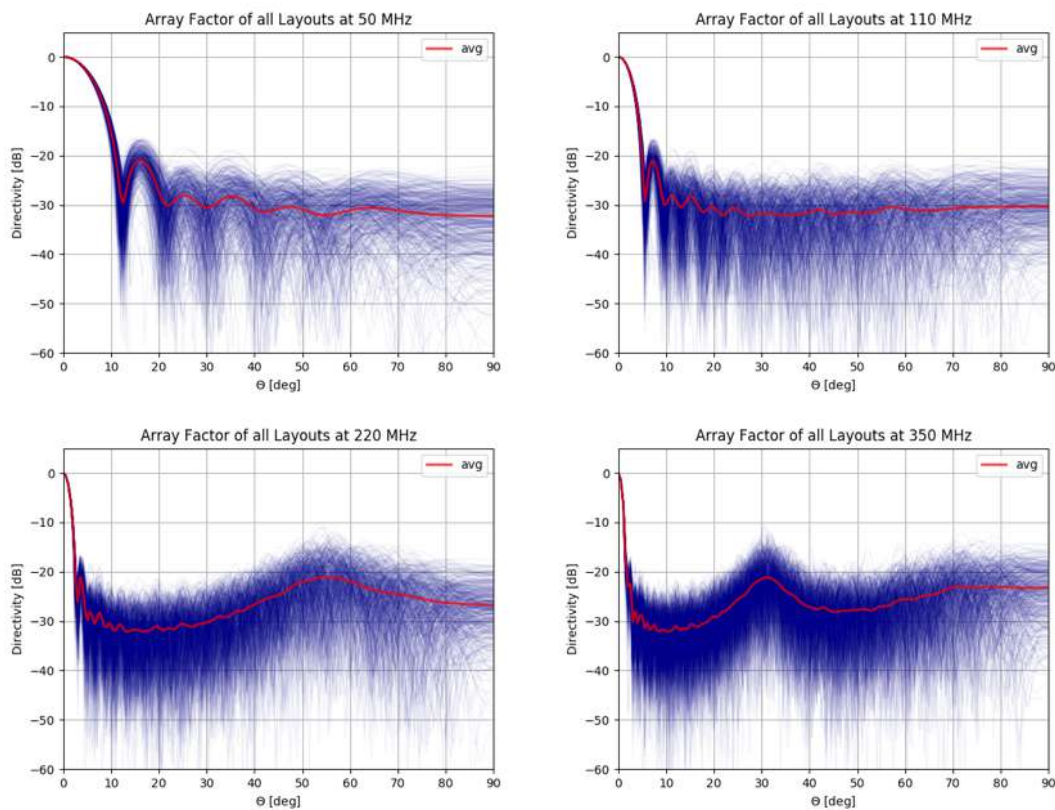


Figure 18: Comparison between 512 different layouts (different instances of the random layout generator) at 4 different frequencies showing clear differences in the side lobe area.

The impact that station configurations have on the interferometric response of the SKA1-LOW telescope is a subject that needs further work and requires the expertise of other consortia as well. LFAA has designed and optimized the station configuration to minimize the effects of mutual coupling and to realize stations with low side lobe levels. However, end-to-end simulations of SKA1-LOW pipelines analyzing the effects of specific configurations (mutual coupling, side-lobes, etc) in specific observations will be needed to finalize the design of the station layout. So far a limited amount of work has been done using the OSKAR SKA simulator [RD25].

The work carried out in [RD20] simulated visibilities using a large number of interfering sources far from the main lobe of the primary (station) beam of an SKA-like telescope consisting entirely of aperture arrays (see Figure 19 for a view of the single element and cross correlated station beams using AAVS1 like stations). These sources had the effect of introducing a noise-like corruption to images, known as the Far Side lobe Source Noise (FSSN). Whilst many components of system noise behave like Gaussian random variables, and therefore tend to decrease as observation length increases, FSSN is due to a multitude of side-lobes from real sources that will not tend to zero simply by integrating for an infinite time. For this reason, FSSN is a very practical metric to use in such simulations to determine the performance of aperture array stations. In Figure 20-**Figure 22**, we present the summary of that analysis.

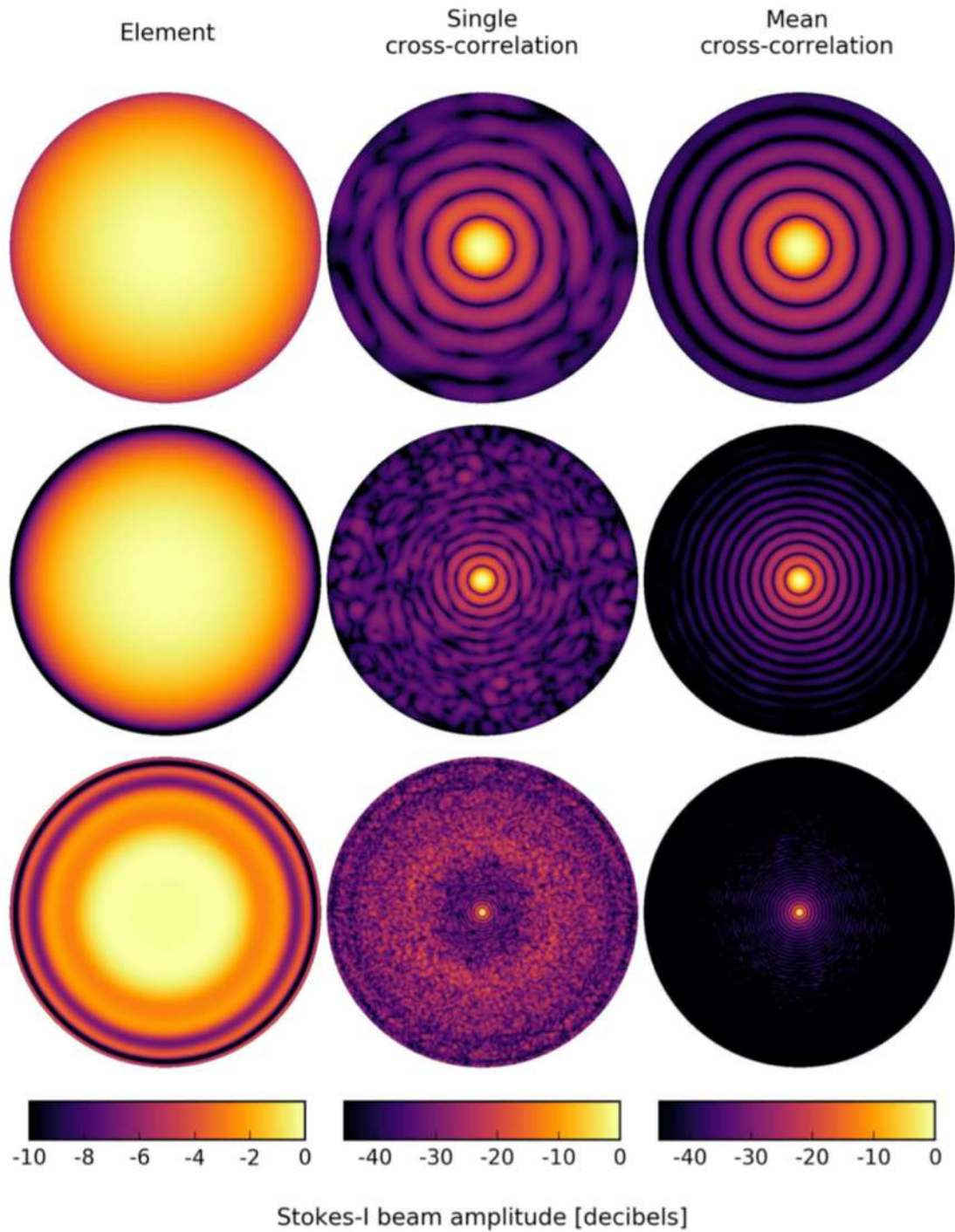


Figure 19: Plots showing the all-sky coverage of the Stokes-I element beam (left column), the cross-power station beam for a single baseline (middle column), and the average cross-power station beam for the whole instrument (right column) at 50 MHz (top row), 110 MHz (middle row) and 350 MHz (bottom row).

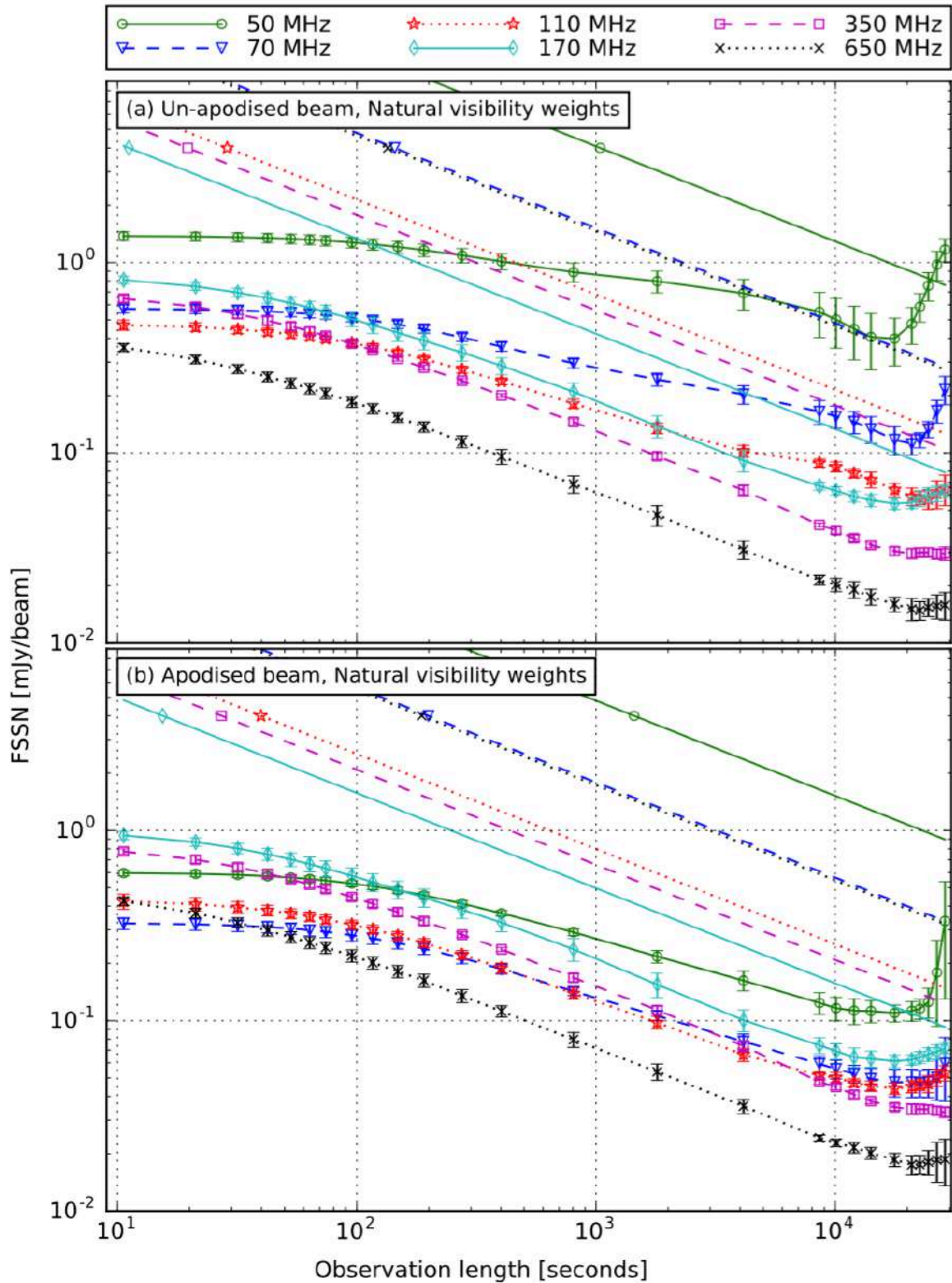


Figure 20: FSSN time scaling from 10 seconds to 8 hours using natural visibility weighting for 6 observation frequencies using (a) un-apodised and (b) apodised stations. Error bars show the 1-sigma variation between 6 pointings. Straight lines represent estimated thermal noise.

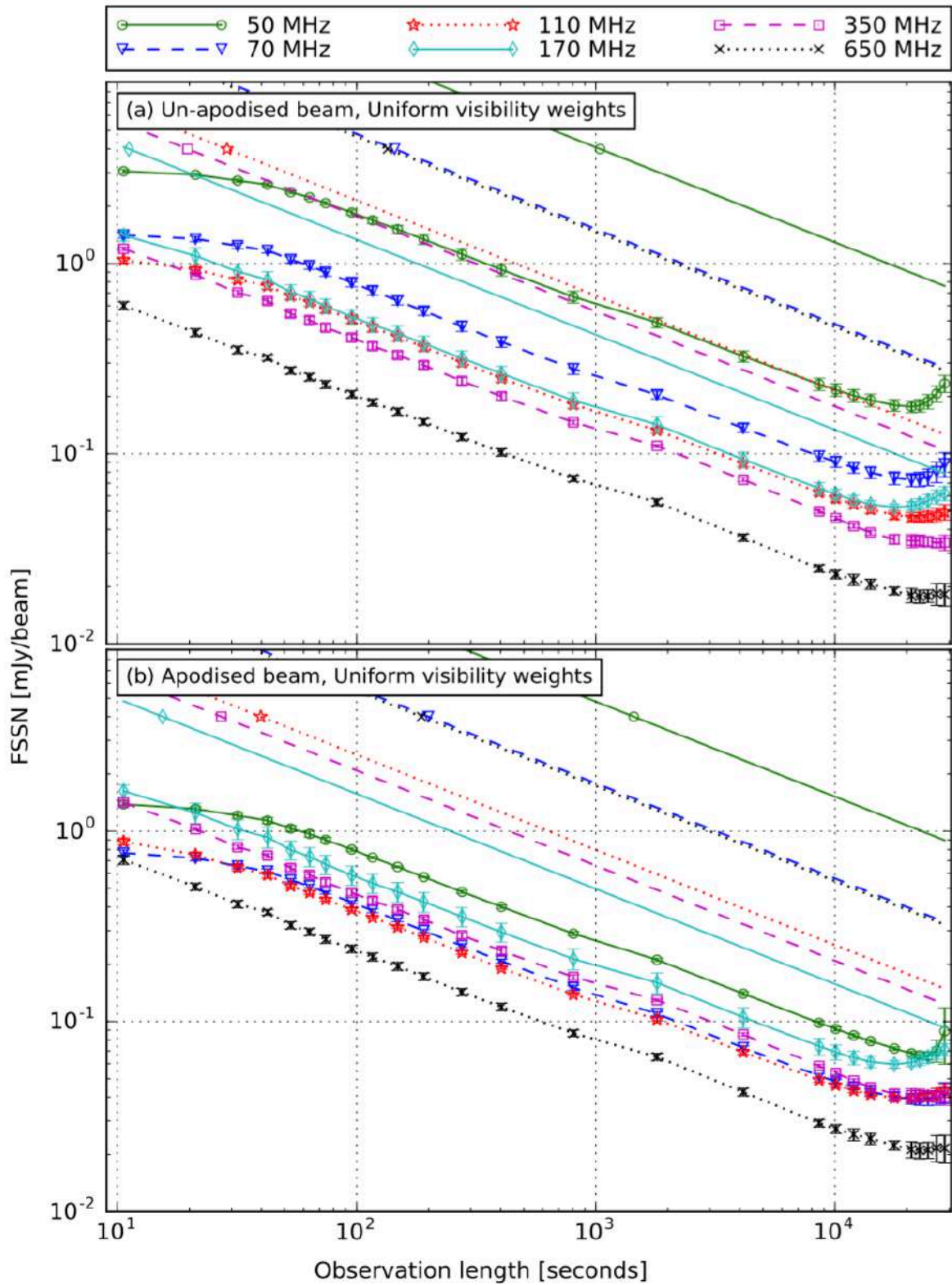


Figure 21: FSSN time scaling from 10 seconds to 8 hours using uniform visibility weighting for 6 observation frequencies using (a) un-apodised and (b) apodised stations. Error bars show the 1-sigma variation between 6 pointings. Straight lines represent estimated thermal noise.

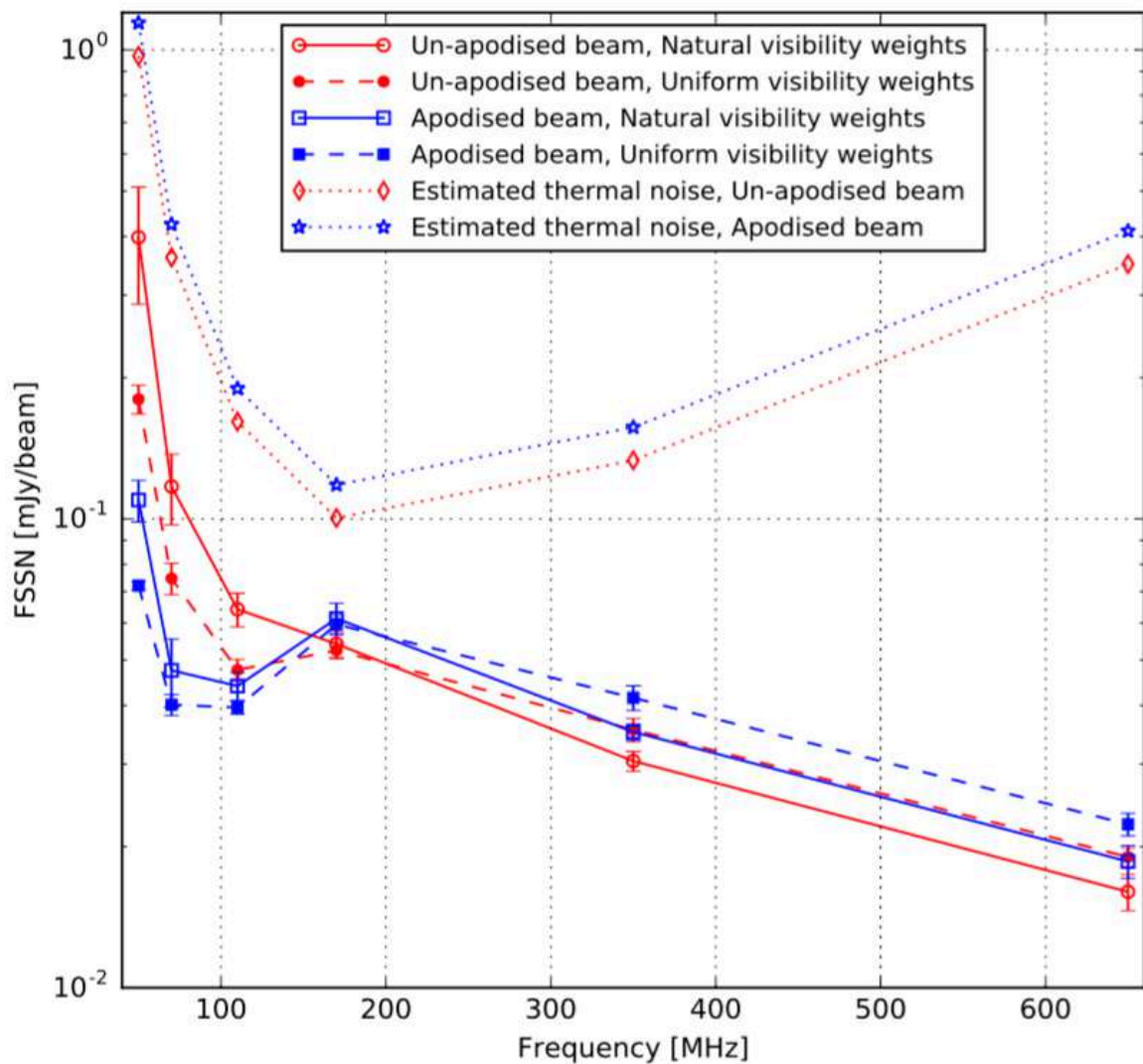


Figure 22: FSN frequency scaling for a 17702 second (~ 5 hour) observation, for both unapodised station beams (circular symbols) and apodised station beams (square symbols), imaged using natural visibility weighting (solid lines/empty symbols) and uniform visibility weighting (dashed lines/filled symbols). The dotted lines show the estimated thermal noise for the observation. Error bars are drawn to show the 1-sigma variation between the 6 simulated pointings.

An important aspect of the work described in [RD20] is that the simulations of FSN were carried out with each station in the array having not only a random configuration as described previously but also with each station having a different random configuration as compared to each other. Since all stations have different randomised layouts, the resulting cross-power beam suppresses the far-out side lobes of the station beam well and at higher frequencies, the main lobe of the station beam gets smaller and therefore acts as a better spatial filter on the sky. A critical aspect to note about this work is that the array beam along with its grating response will form an envelope on the PSF.

There are various other tools in our so-called design arsenal which can be used to improve the performance of aperture arrays for interferometric observations. These include station rotations, which tend to help if the station has a very regular grating response (e.g. in the case of LOFAR HBA),

tapering and in general optimized weighting schemes. Amplitude tapering the array (see **Figure 23** for an example) will reduce sensitivity but will improve significantly the near in side lobes described earlier as the coherent zone. Also interesting schemes such as equal area weighting described in [RD26] can help by adjusting the element weighting of a random array based on occupied area which provides an improvement in near-in sidelobe levels at the cost of a slight increase in the average power of far-out sidelobes. The impact on Signal to Noise ratio however would have to be considered in an optimization using this scheme.

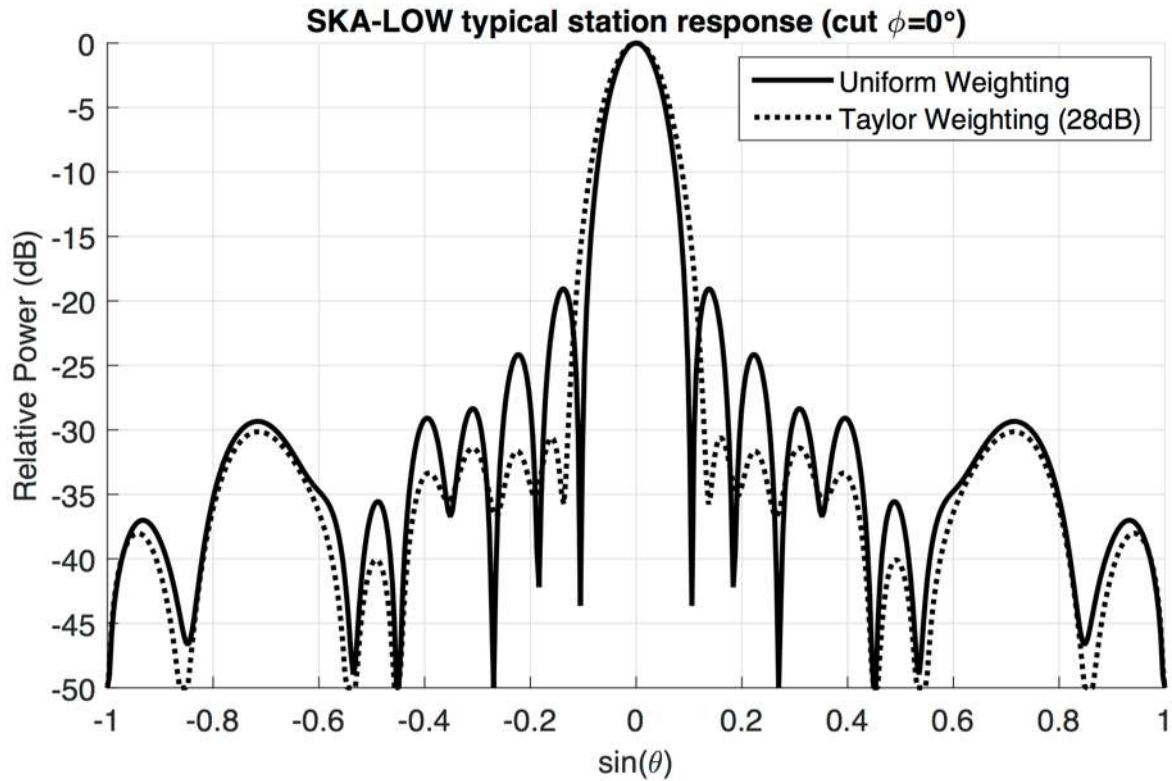


Figure 23: Example of the effect of weighting in the station beam.

6 EM Modeling

Our ability to predict the response of the station to a sky signal is crucial to achieve the science goals of SKA. Beam models are needed in several steps of the instrument's calibration and signal processing (eg. imaging). The closer these beams are to the actual beam the easier the calibration of the telescope. While mutual coupling effects are virtually invariant with time since they respond to physical properties of the array, we need to understand and be able to predict them.

The embedded element patterns of the antennas in the array environment are mostly time invariant (except for physical changes in the array, eg. mechanically effects on the antennas). This is the case for well-matched antennas where the potential slight change in the load impedance due to changes in the LNA input impedance (eg. due to temperature changes) would only have a small effect on the embedded patterns. These embedded element patterns can then be used to form the station beam by multiplying them by the right weight (for the desired scanning angle) and add them together.

This section is dedicated to describe the electromagnetic (EM) simulations of SKA1-LOW stations. We briefly present the methods used for these simulations and present results of its validation using different commercial and in-house codes. Section 8 is then dedicated to present measurements of array prototypes to further validate these simulations.

The subject of electromagnetic modelling of large structures is a very active area of research in the antenna engineering community. For the last few decades commercial codes have been developed around the globe to tackle the problem of solving Maxwell's equations in arbitrary domains. It is fair to say that these solvers are constantly improving and becoming more computationally efficient.

The biggest challenge at long wavelengths resides in the measurement of the electromagnetic response of the arrays given the application, wavelength and size of the instrument. However, in this area, both the engineering and physics communities have realized a lot of work in the last decades and years.

6.1 Commercial codes

Several commercial codes have been used for the modelling of SKA1-LOW stations. These include:

- CST (Integral equation solver) [RD27].
- FEKO (Method of Moments) [RD28].
- WIPLD (Method of Moments) [RD29].

These software packages implement numerical methods for the solution of Maxwell equations in electromagnetic structures of arbitrary shape. These codes are all capable of simulating SKA1-LOW stations although they can be computationally expensive. A full wave simulation of a SKA1-LOW station can take several tens of hours or days per frequency point. In the next section we describe an alternative code, developed specifically for the SKA capable of reducing this simulation time to ~1 min while preserving the accuracy given by commercial codes.

It is worth noting that in all cases the inclusion of all the structures present in the environment of the antenna array (eg. finite ground planes, landscape features, metal boxes, cables, etc) increases the complexity of these simulations dramatically.

6.2 HARP

HARP (HARmonic-Polynomial) [RD31] relies on the Macro Basis Functions (MBF) approach and an interpolatory technique to compute the interactions between MBFs [RD30]. In brief, the MBFs are subdomain descriptions of the currents in the array structure that are used to calculate the currents and radiated fields for a given set of excitation weights.

HARP has been developed since 2009 specifically to simulate large arrays of disconnected antennas in random layouts such as the SKA1-LOW stations. Through a series of mathematical operations, HARP has managed to successfully reduce the computational cost and simulation time for an array of the size and shape of a SKA1-LOW field station by several orders of magnitude (eg. full EM simulation of the array at ~1 min. per frequency vs ~ 50-100 hours with commercial codes). This will allow SKA to quickly re-compute station beams practically on the fly if needed.

The detailed description of the method is described in [RD31].

6.2.1 Meshing SKALA4 in HARP and comparison with commercial codes

The SKALA4 antenna has been simulated in HARP both as an isolated element and as part of the array. For that purpose the antenna has to be decomposed in basis functions. This is a manual process that requires of the understanding of the structure and the currents that will flow through it. Figure 24 show a view of the mesh of SKALA4 in HARP.

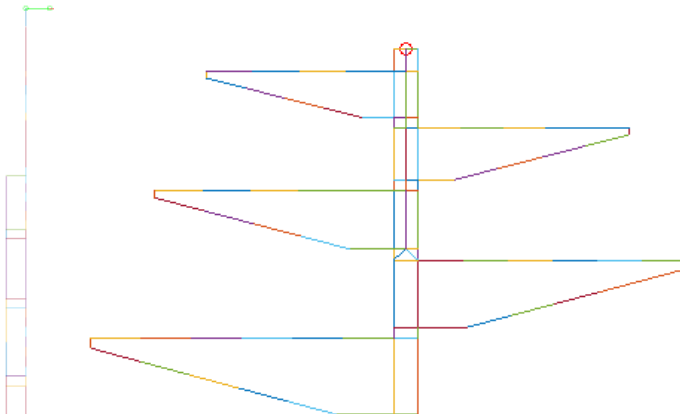


Figure 24: Feeding point details of the HARP mesh (1 polarization).

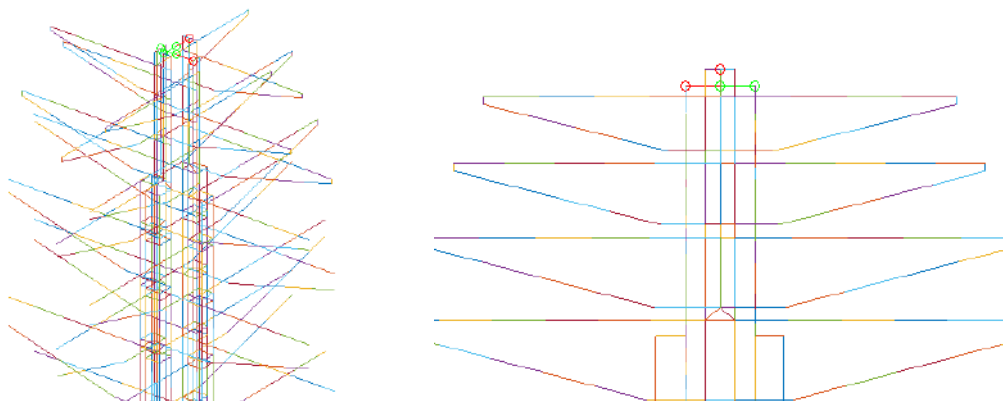


Figure 25: Feeding point details of the HARP mesh (2 polarizations).

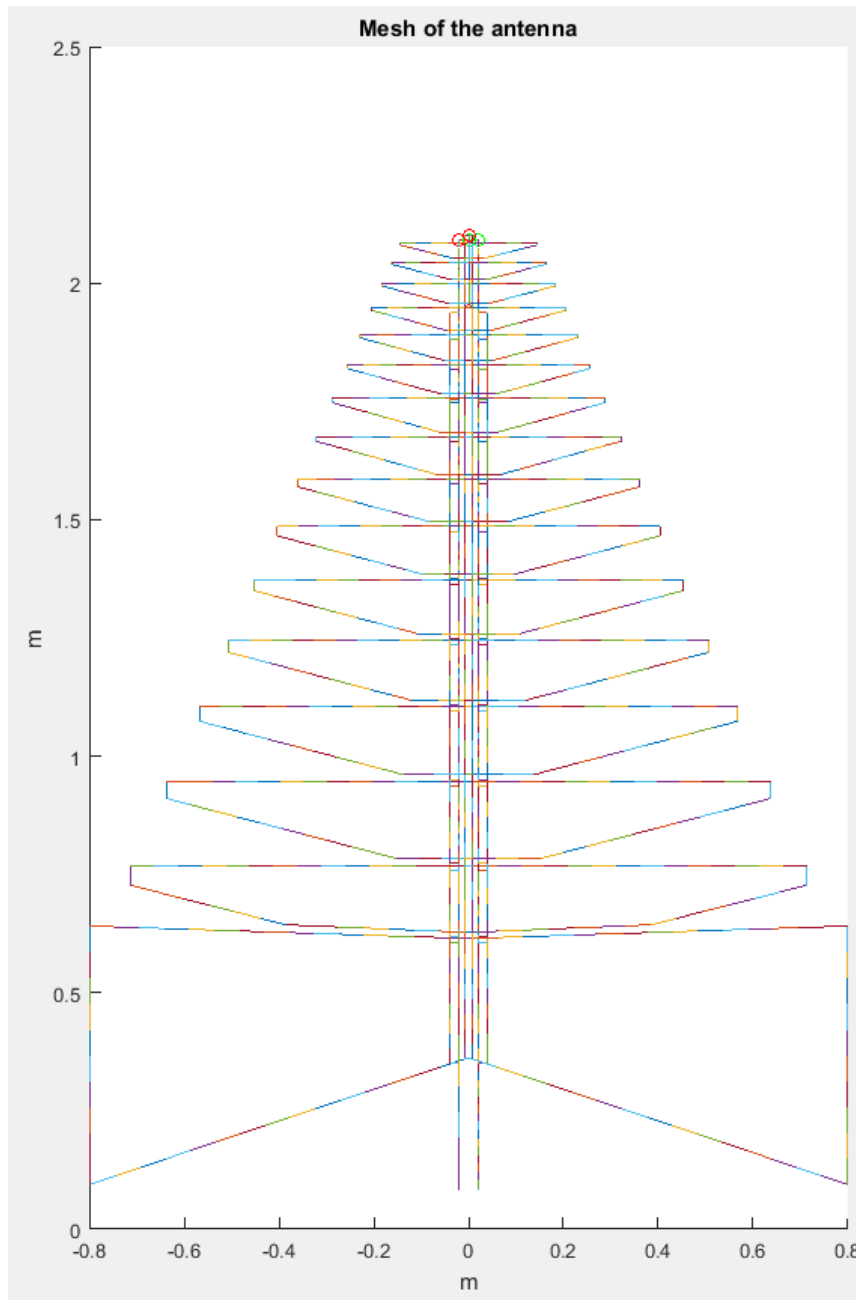


Figure 26: SKALA4.1 HARP mesh.

6.2.1.1 Single element validation

The first step in the validation is to compare the numerical results from different codes with an isolated element (no mutual coupling). In **Figure 27**, the comparison between FEKO and HARP is presented. As it can be appreciated there is very good agreement between both codes.

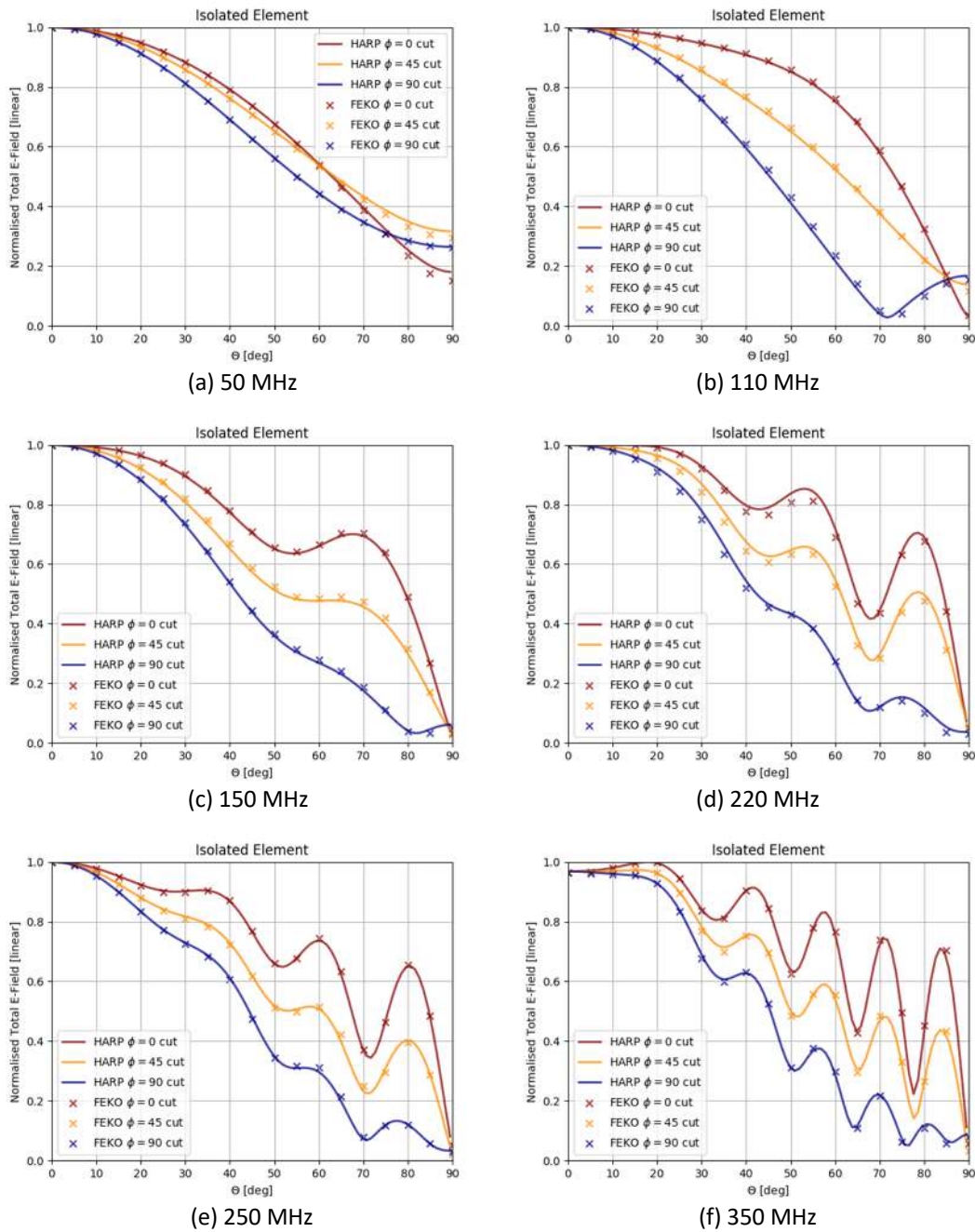


Figure 27: Comparison of beams between HARP and FEKO across frequency.

6.2.1.2 Small array validation

Secondly, the codes are checked against each other for a small array (16 elements in this case). For these small arrays it is still acceptable the use of commercial codes from a computational cost point of view. In the following figures we present the simulated beam of a 16 element pseudo random array (Pre-AAVS1, see Section 8 for more information). Again, the agreement is good.

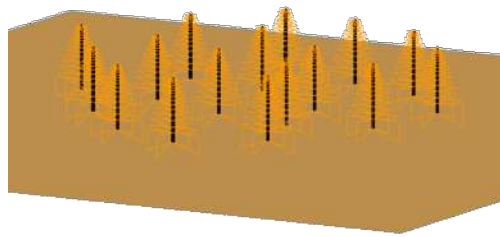


Figure 28: Pre-AAVS1 array with SKALA4.

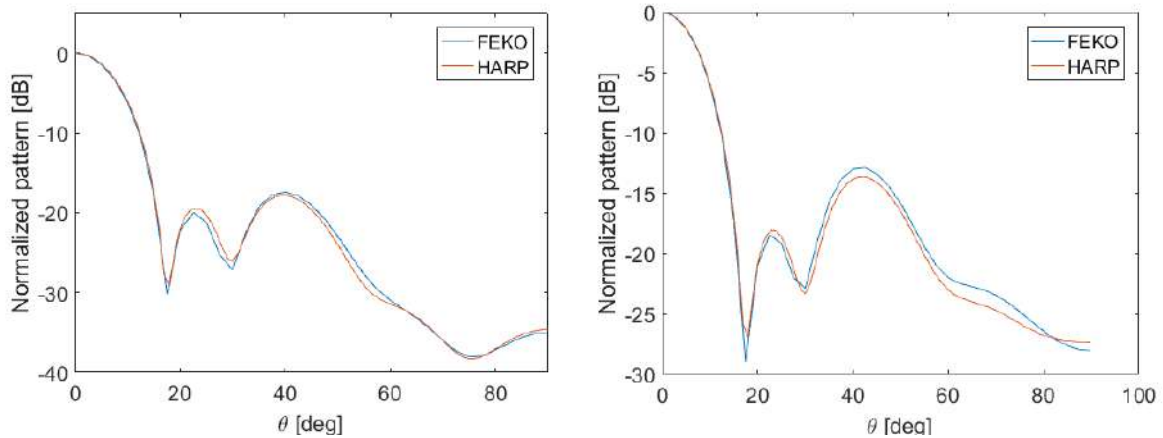
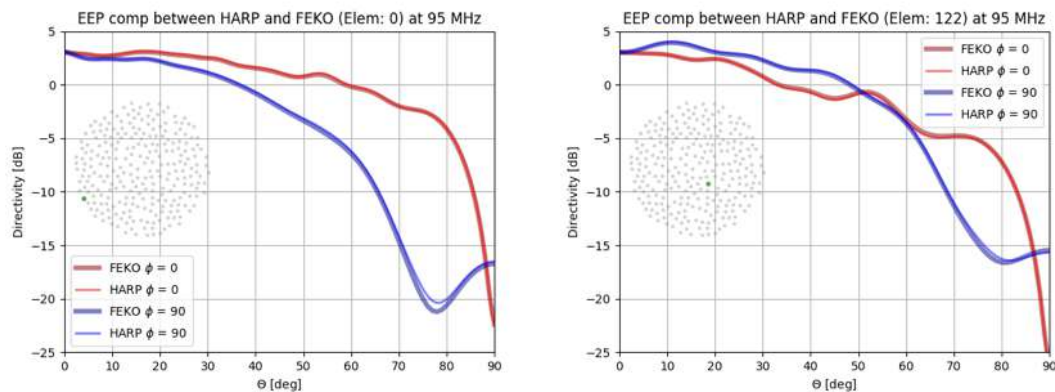


Figure 29: Comparison of the beam between FEKO and HARP at 150 MHz for a 16 element array of SKALA4 antennas.

6.2.1.3 SKA1-LOW station validation

Finally, we produce simulations of a SKA1-LOW station with both codes and compare. We present the comparison of embedded element patterns since they contain all the mutual coupling information. In **Figure 30** we can see this comparison for 2 different elements, one on the edge of the array and one on the centre (see position of the element in the layout inside the figures). The agreement between both is good although some differences can be seen at higher angles.



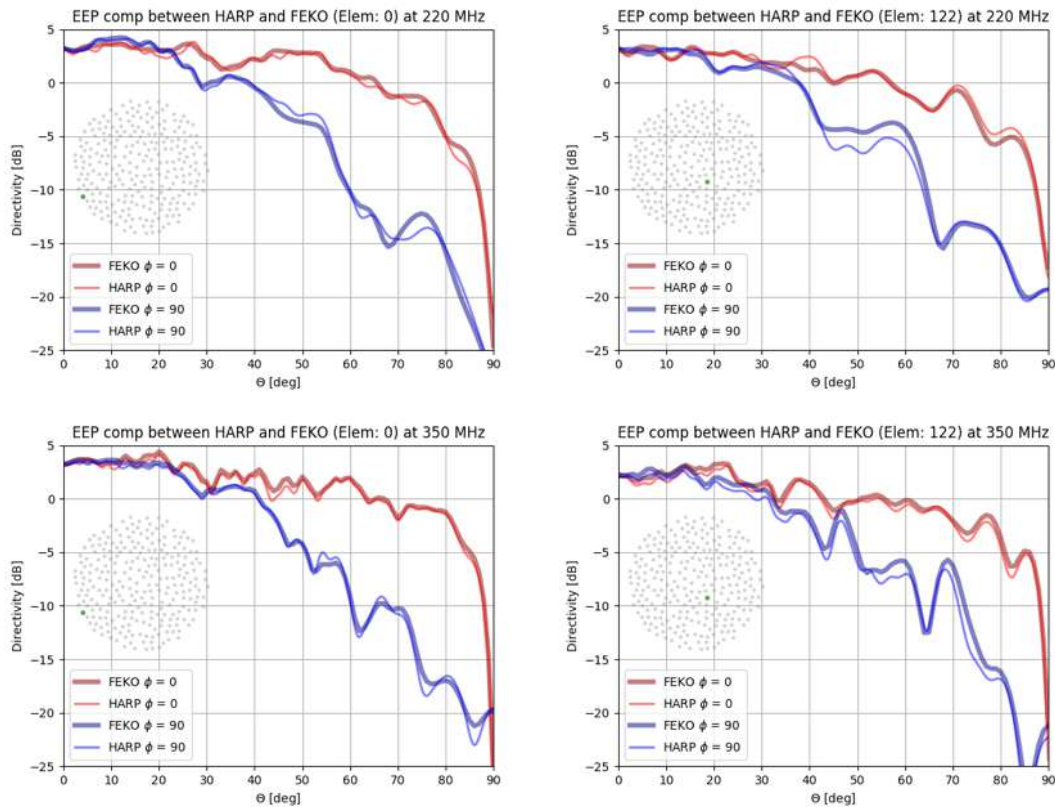


Figure 30: Comparison of embedded element patterns calculated using HARP and the commercial code FEKO at 3 frequencies: 95 MHz (top), 220 MHz and 350 MHz (bottom). These are shown for an element at the edge of the array (left column) and at the center of the array (right column).

6.2.1.4 Further validation

In this section we present further validation from simulations of arrays with SKALA2 (the AAVS1 array [RD4]). In **Figure 31** we show the random layout of the AAVS1 prototype array. In **Figure 32- Figure 34** we show comparison of simulations of both embedded element patterns for a central element and the array pattern (zenith and off zenith scan) with HARP and the commercial code WIPL-D. This comparison shows the quality of the agreement between the 2 different simulation methods. The level of error for the array pattern is maximum at the main beam and always less than -20 dB. Furthermore this error does not significantly increase with at other scanning angles.

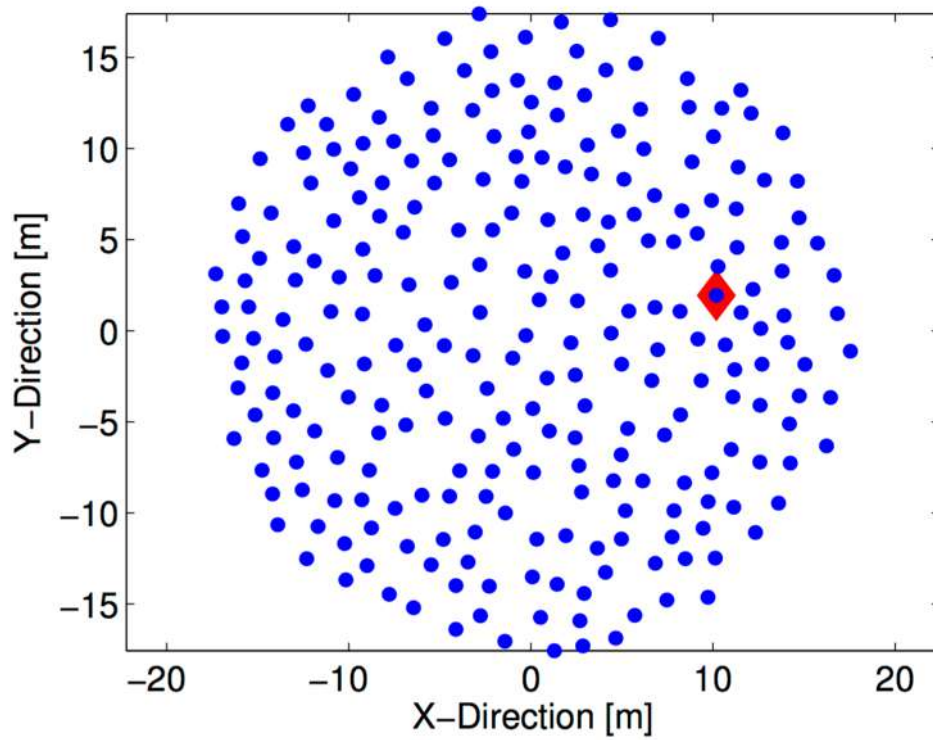
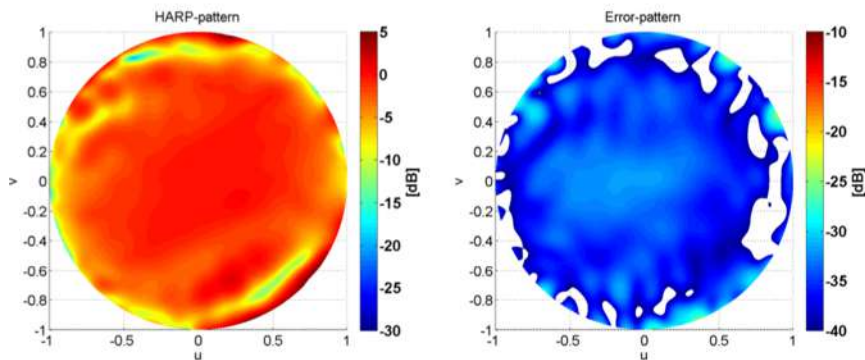
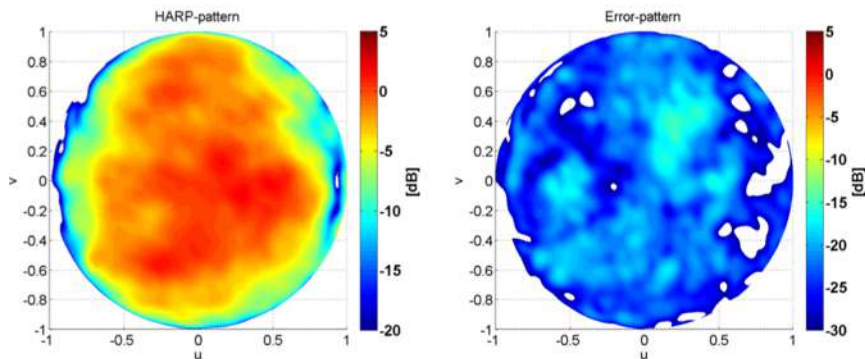


Figure 31: AAVS1 configuration



(a) 50 MHz.

(b) Error Pattern 50 MHz



(c) 110 MHz.

(d) Error Pattern 110 MHz

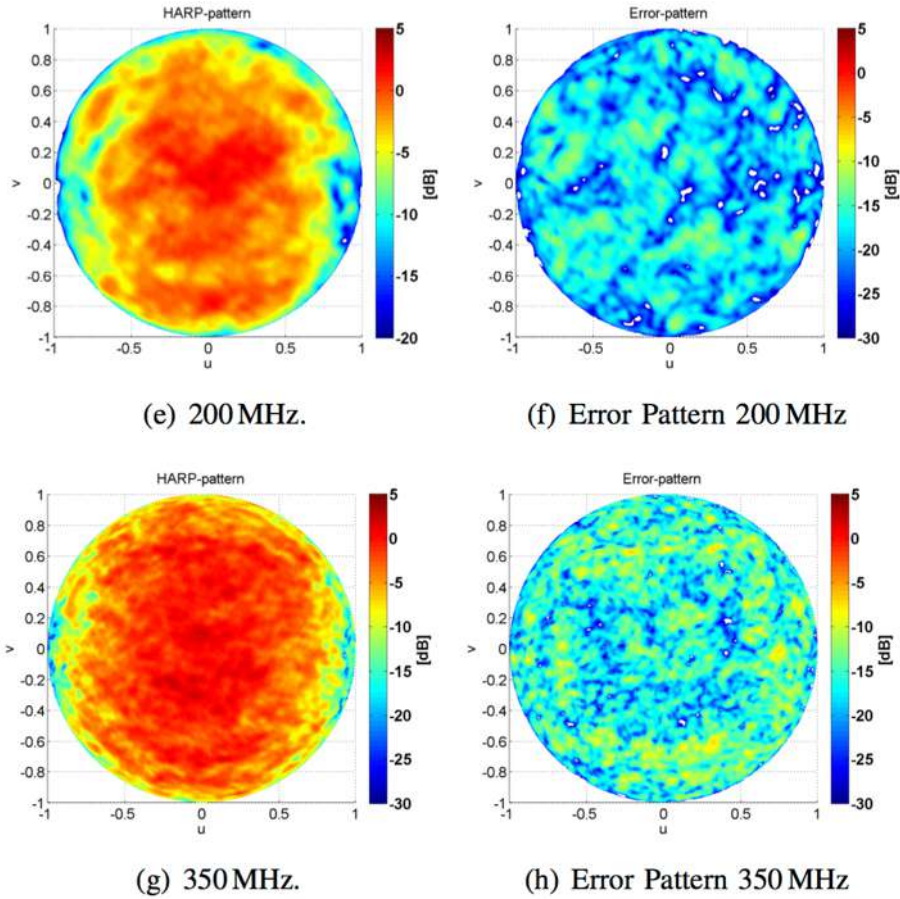
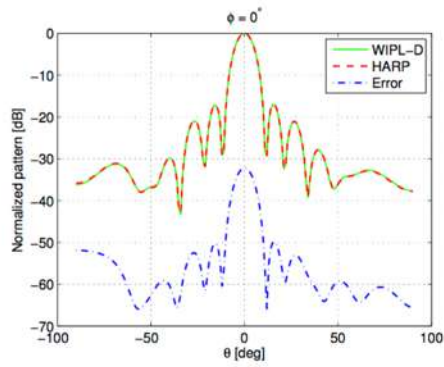
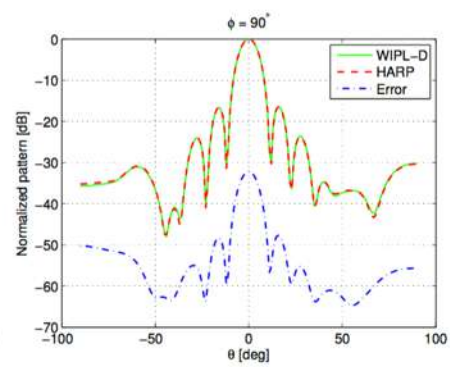


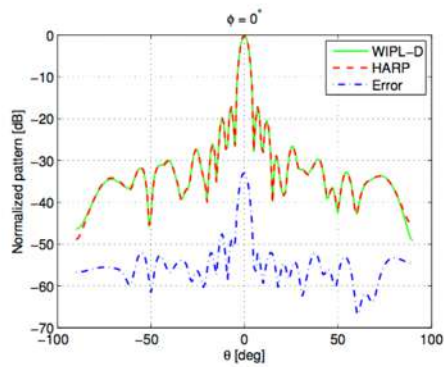
Figure 32: Embedded element pattern of a central element in AAVS1 (see element position in the AAVS1 layout above) at different frequencies as simulated by HARP (left column) and error pattern wrt to the commercial code WIPL-D (right column).



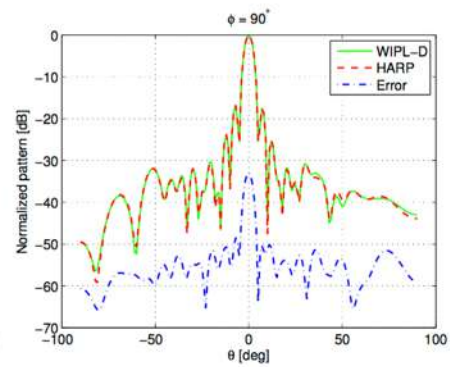
(a) E-plane: $\phi = 0^\circ$, 50 MHz



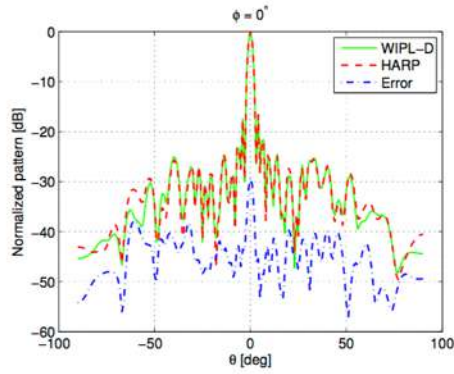
(b) H-plane: $\phi = 90^\circ$, 50 MHz



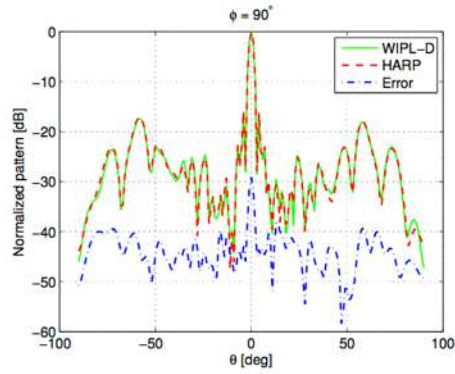
(c) E-plane: $\phi = 0^\circ$, 110 MHz



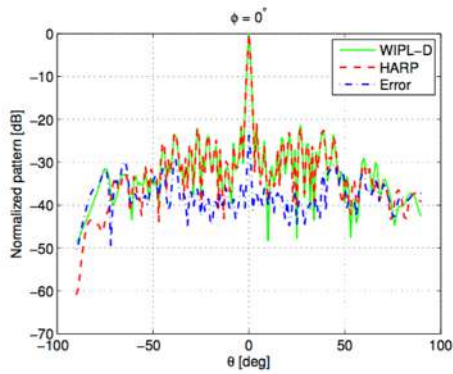
(d) H-plane: $\phi = 90^\circ$, 110 MHz



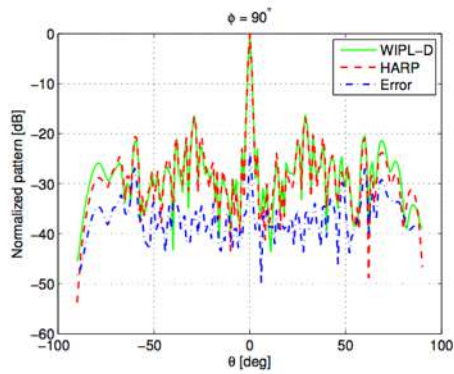
(e) E-plane: $\phi = 0^\circ$, 200 MHz



(f) H-plane: $\phi = 90^\circ$, 200 MHz

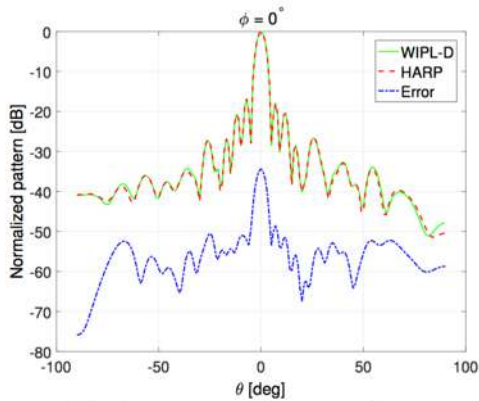


(g) E-plane: $\phi = 0^\circ$, 350 MHz

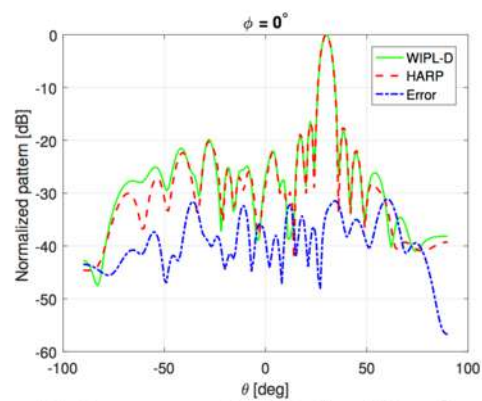


(h) H-plane: $\phi = 90^\circ$, 350 MHz

Figure 33: Array pattern cuts at different frequencies as simulated by HARP and the commercial code WIPL-D.



(a) Array scanned at broadside



(b) Array scanned at $(\phi, \theta) = (0^\circ, 30^\circ)$

Figure 34: Comparison of the simulated AAVS1 array pattern at 110 MHz scanned at zenith and at 30 degrees with HARP and the commercial code WIPL-D.

7 Station performance

This section presents the main results relevant to discuss compliance with the SKA1-LOW requirements.

7.1 Sensitivity

In **Figure 37** the Directivity at zenith versus frequency for a SKA1-LOW station including the effects of mutual coupling is presented. In **Figure 36** the directivity of the station across the whole field of view is presented (ie when the station is scanned to any angle across the field of view). This informs us of the expected drop of sensitivity off zenith angles. From the directivity we can calculate the effective area as shown in **Figure 37**. Together with the system temperature, we can then calculate the sensitivity [RD32] of the SKA1-LOW station (shown in **Figure 38**). There are 3 distinctive regions shown in these plots. A first region is at low frequencies (50 to ~100 MHz) where the effects of mutual coupling limit the effective area of the station (dense region). A second region is from ~100 to ~200 MHz and it is called the dense-sparse transition region. In this region the effects of mutual coupling are largest since the antennas are electrically larger than in the dense region and therefore able to support more current modes due to mutual coupling and at the same time the electrical distance between antennas is still relatively small (as compared to the third region). The final region is between ~200 to 350 MHz. This is the sparse region of the array and here the effects of mutual coupling are less as the electrical distance between the antennas increases.

In **Figure 38** the sensitivity is shown. In that plot we also show the SKA-LFAA L3 requirements for station sensitivity in a solid red line as well as a point-to-point cubic spline specified at 11 points across the frequency band. In green, the percentage difference between the sensitivity at zenith and the cubic spline is shown. The 11 frequency points used to define the cubic spline are marked with orange crosses. These points are not evenly spaced and are positioned at the reference frequencies through the band (as per the L1 requirements [AD2]). The resulting percentage difference has a strong dependency on the position of these points. The spectrally slow variations visible in the sensitivity plot are mainly due to the directivity of the antenna element changing with frequency as different regions in the LPD antenna become active. In some cases these can be accentuated by mutual coupling as well. These variations are spectrally slow, and as shown in [RD33], the passband is dominated by the antenna-LNA matching and its spectral response. This response can be easily modelled using low order polynomials [RD33]. **Figure 39** shows the averaged (for the 2 polarizations) sensitivity contour plots. These are, as one would expect, circularly symmetric.

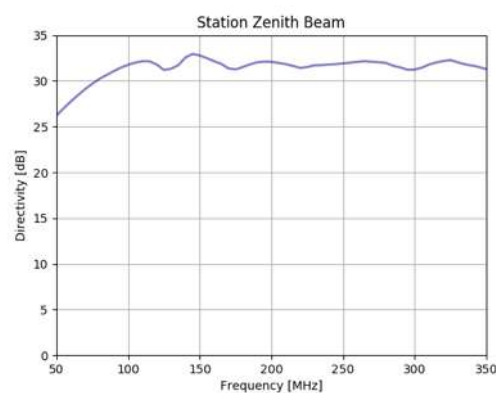
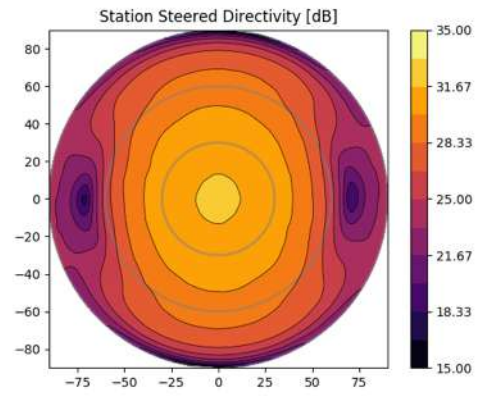
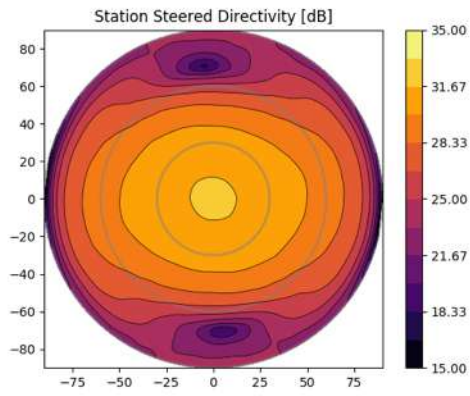
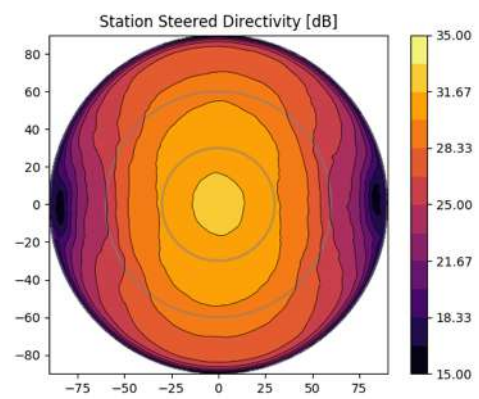
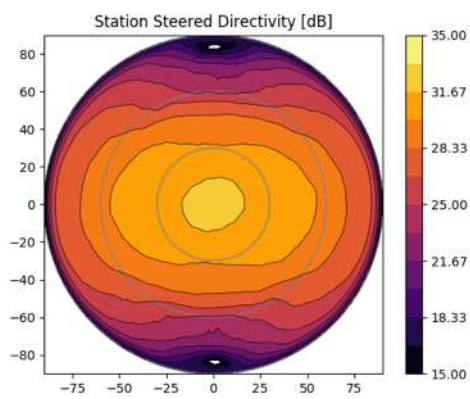


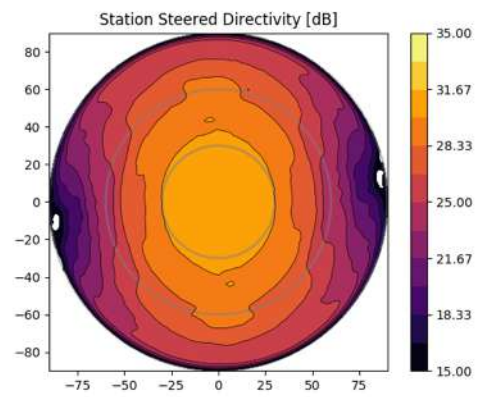
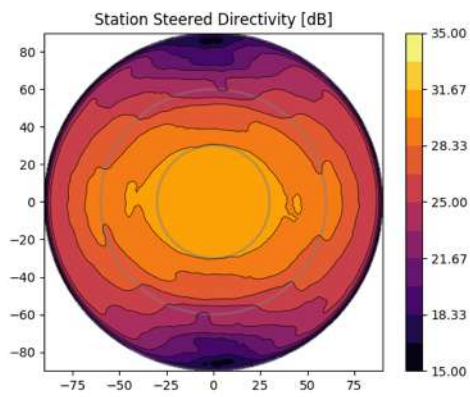
Figure 35: Zenith directivity for a SKA1-LOW station.



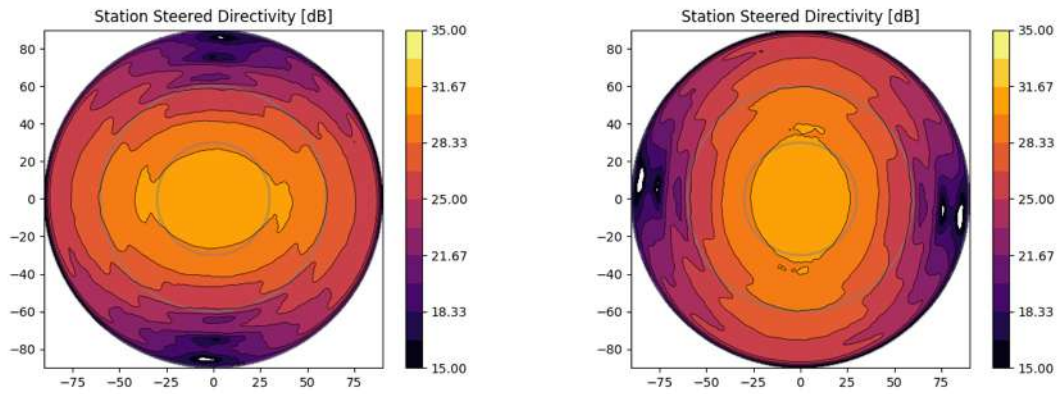
(a) 100 MHz



(a) 200 MHz



(c) 300 MHz



(d) 350 MHz

Figure 36: Station directivity across the field of view.

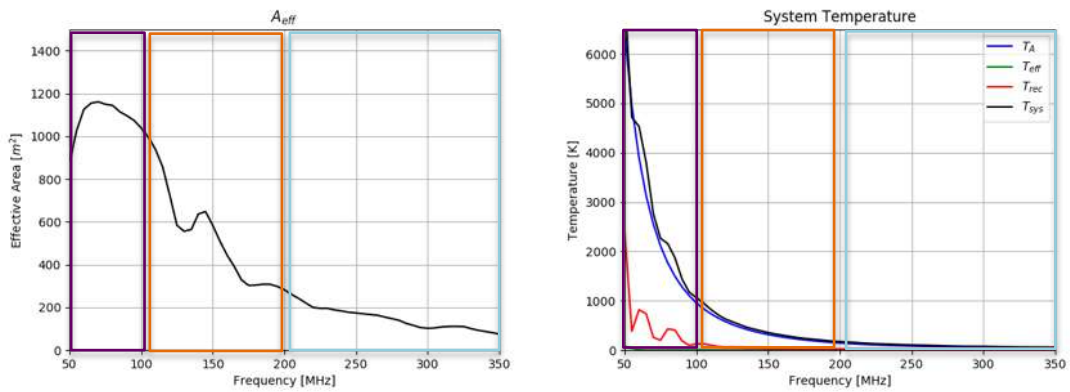
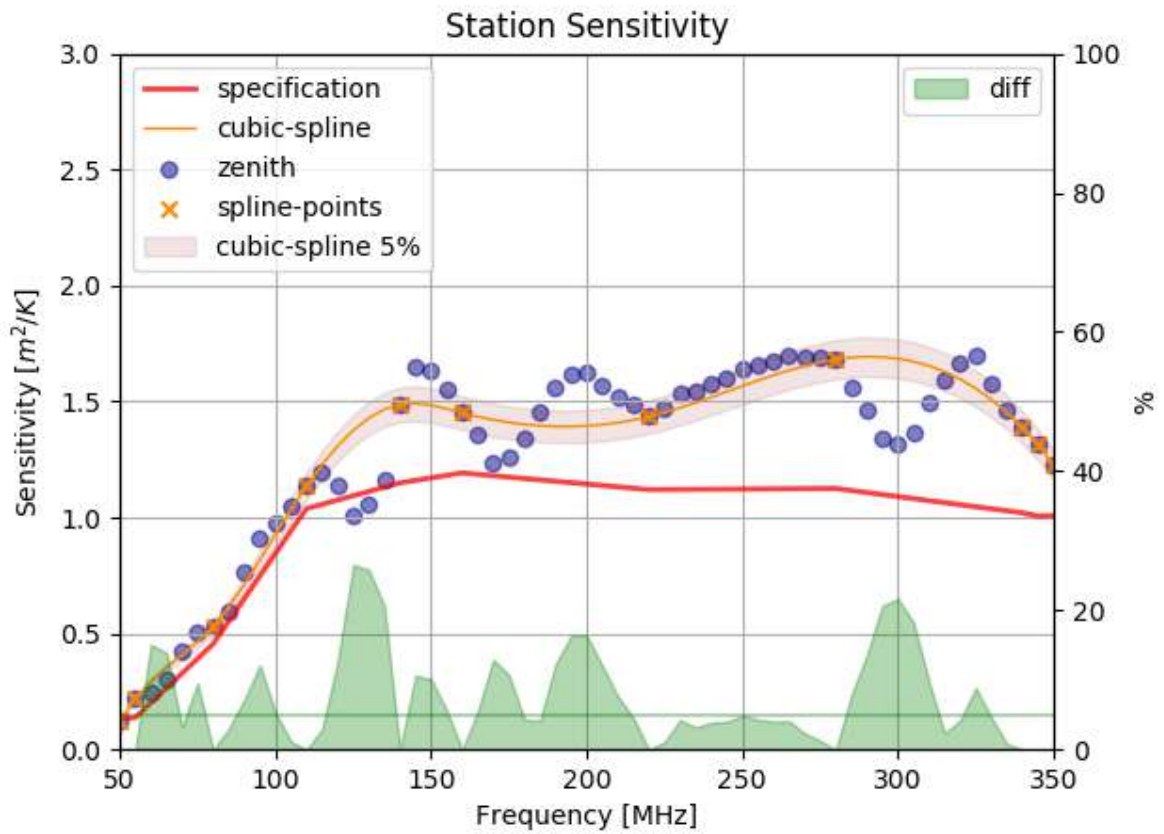
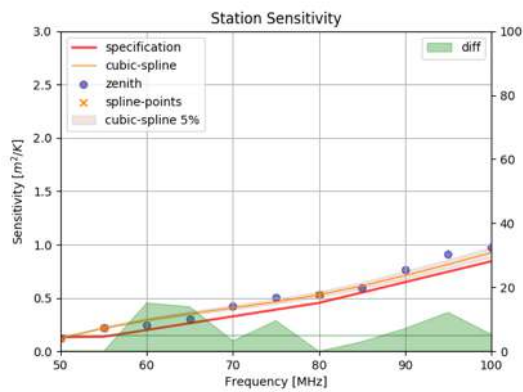


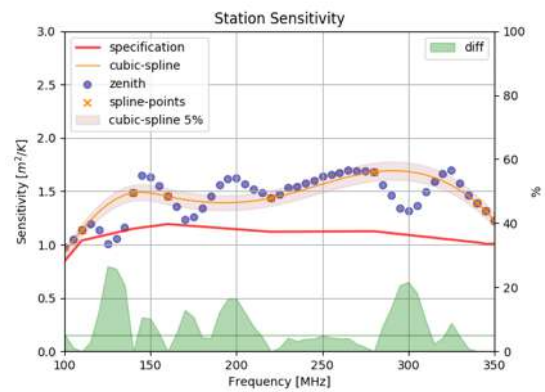
Figure 37: Calculated effective area at zenith for a SKA1-LOW station (left) and system temperature (right). Boxes indicating the dense (purple), dense-sparse (orange) and sparse (light blue) regions are shown.



(a)



(b)



(c)

Figure 38: Zenith sensitivity for a SKA1-LOW station: (a) full bandwidth, (b) dense regime, (c) sparse regime.

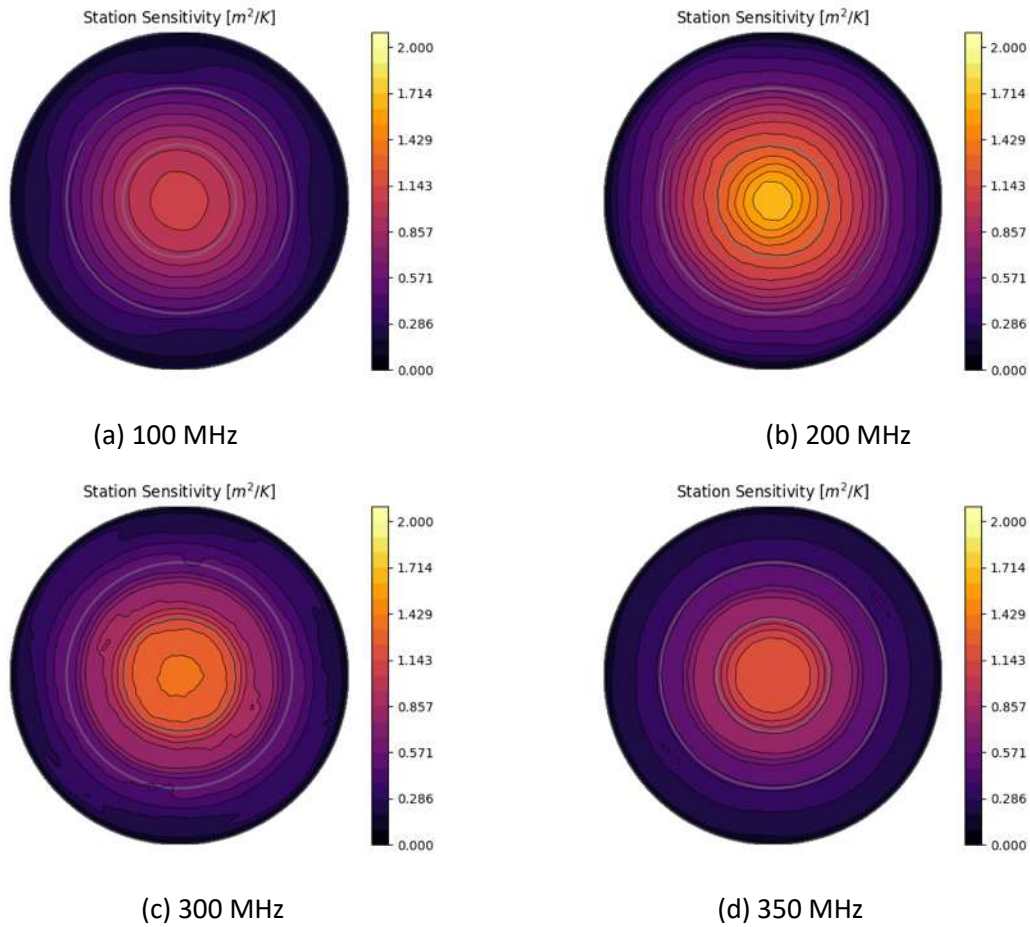


Figure 39: Station sensitivity contour maps at several frequencies (averaged between the 2 polarizations).

7.2 Beams

In the first set of plots in this section the differences between the embedded elements patterns at several frequencies are presented (when loaded with the LNA impedance). Together with this, the mean of all the embedded patterns is shown and also, for comparison, the isolated element pattern. The differences between the patterns increase for larger scan angles (away from zenith). These differences are comparable to those observed for other telescopes [RD34] and are a result of the randomize station layout. As described above, narrower band antennas, and in general antennas that can support less current modes would tend to show similar divergences but of less magnitude. **Figure 41** shows the standard deviation of those patterns for the other polarization. These variations could potentially require specific station calibration algorithms capable of accepting models for all the individual antennas in the array.

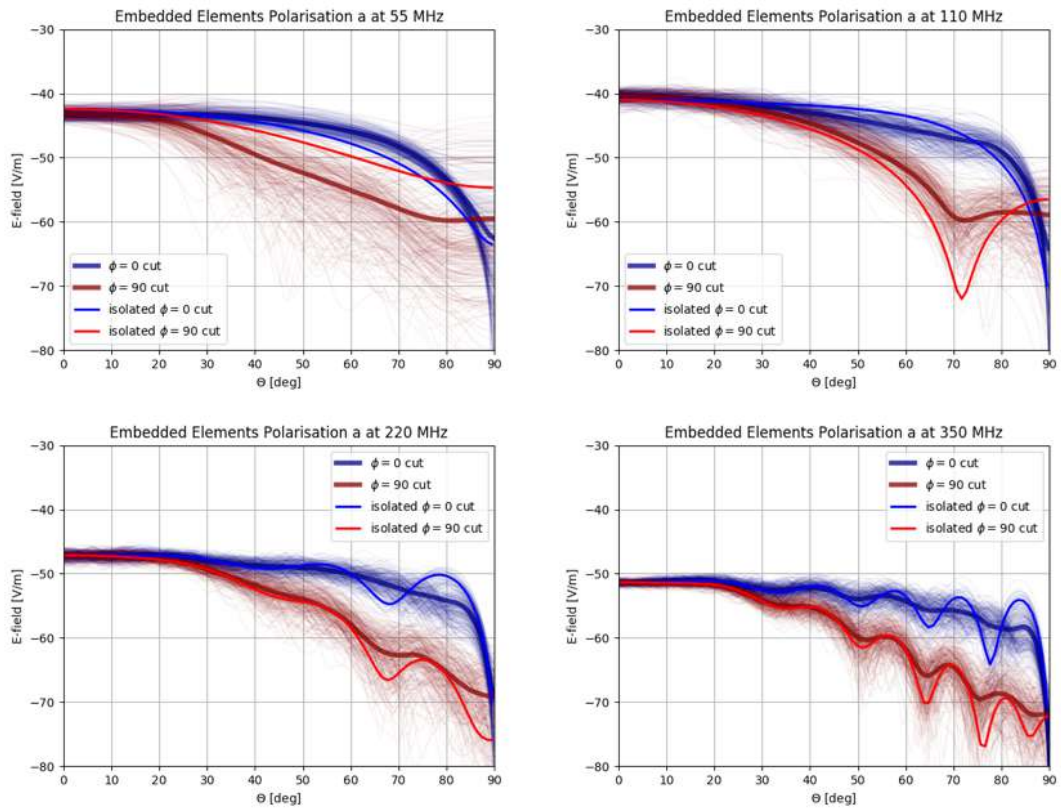
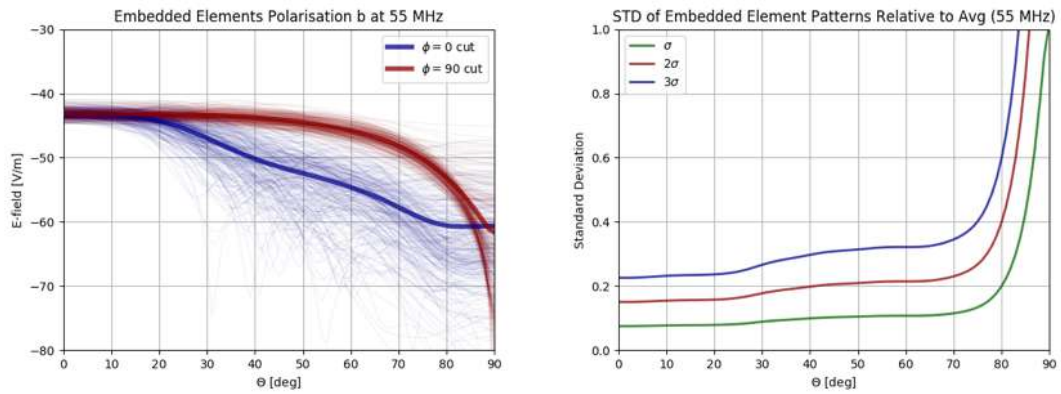


Figure 40: Embedded element pattern beams at multiple frequencies (all patterns in the station). Also shown, the mean of all the EEPs (thick dark red and blue lines) and also the cuts for the isolated element (thin light red and blue lines).



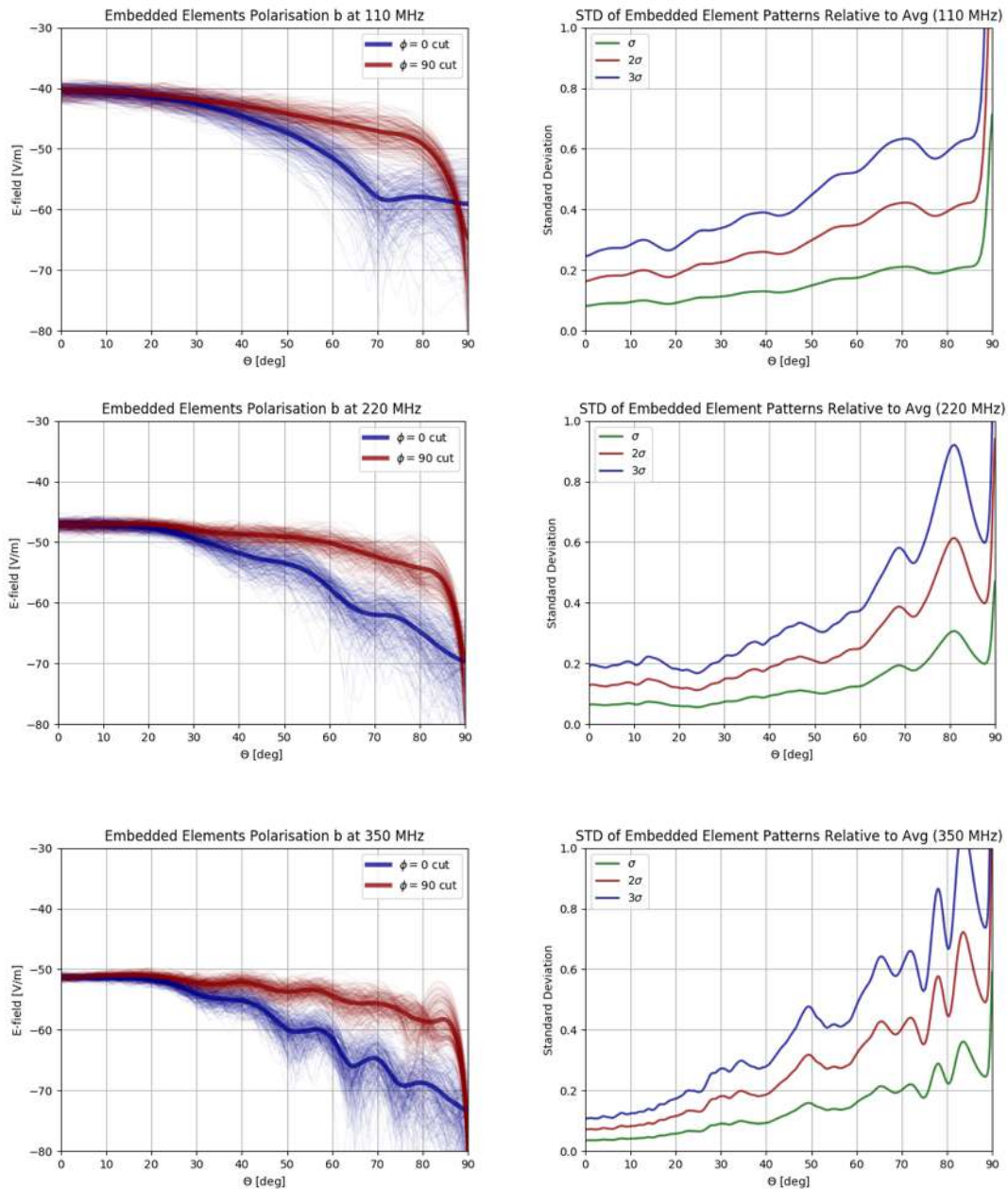


Figure 41: EEPS and Standard deviation of the embedded element pattern beams at multiple frequencies (all patterns in the station), 2nd polarization.

In the following figures we show the amplitude and phase of an embedded element pattern. It is clear that once the phase due to the position of the antenna in the array is removed, the phase pattern is a relatively smooth function.

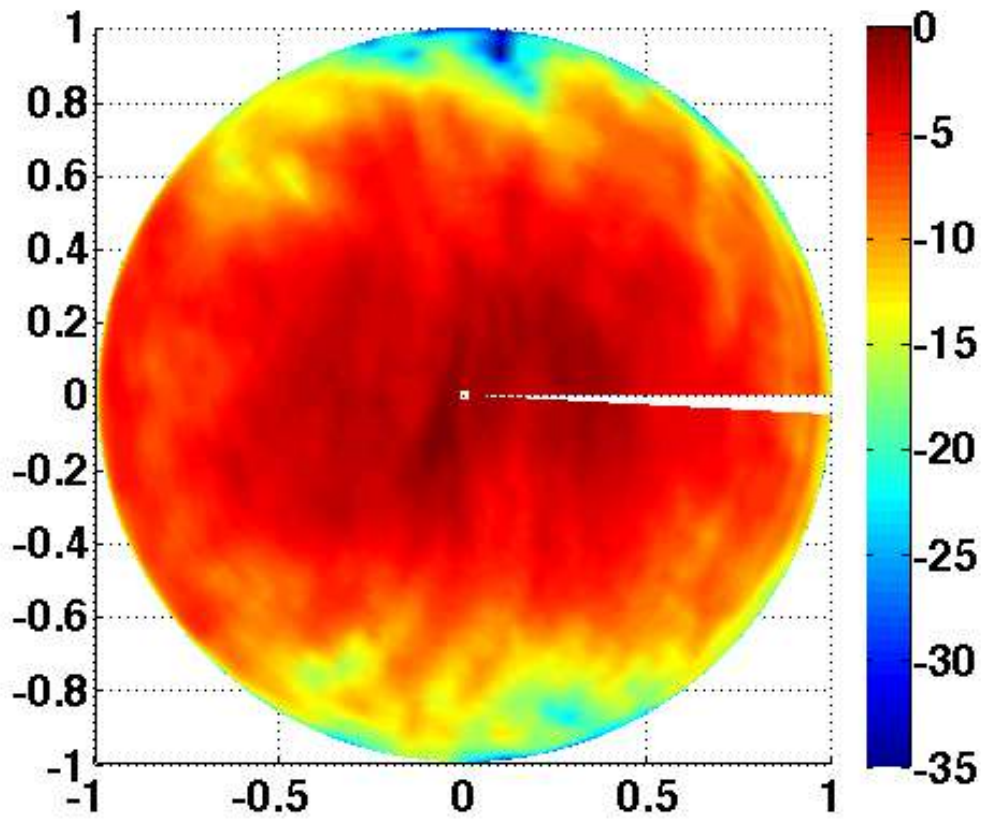


Figure 42: Full EEP of an element in a SKA1-LOW station (absolute value) in dB and normalized to the maximum (160 MHz).

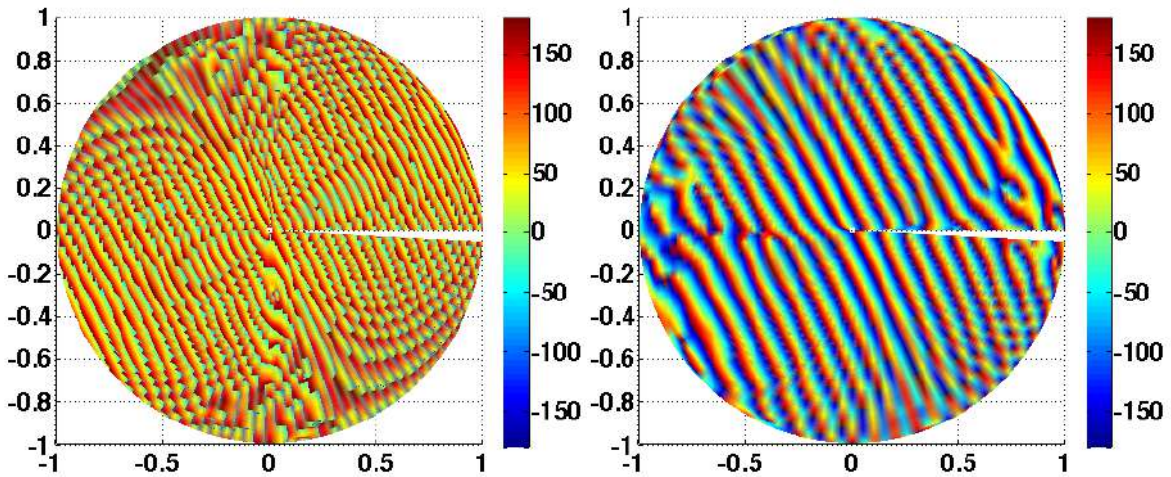


Figure 43: Phase of EEP of an element in a SKA1-LOW station with respect to the center of the station (horizontal (left) and vertical (right) components of the field) in degrees (160 MHz).

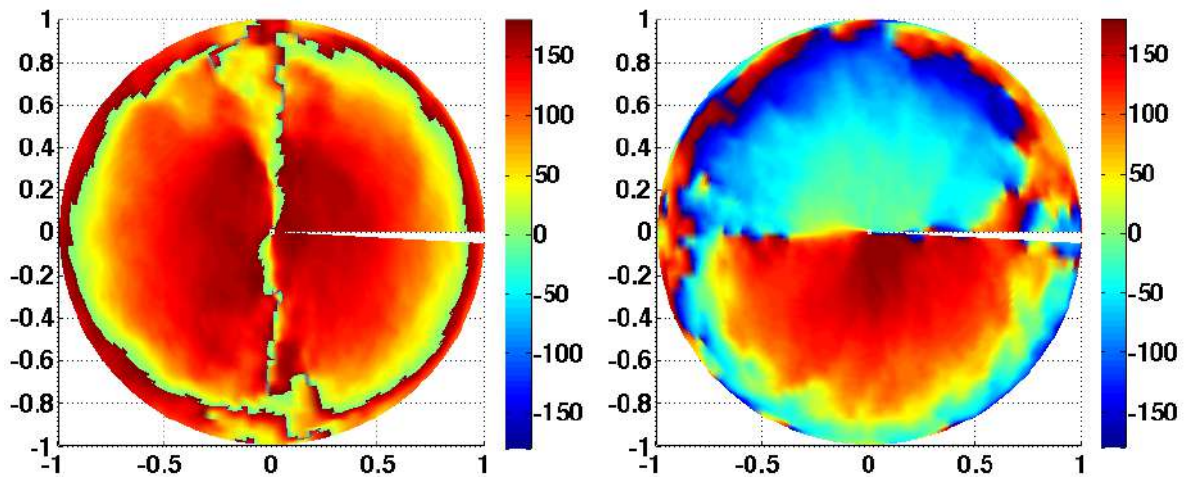


Figure 44: Phase of EEP of an element in a SKA1-LOW station with respect to the center of the antenna (horizontal (left) and vertical (right) components of the field) in degrees (160 MHz).

The following plots show the simulated beams for the station with and without mutual coupling. It can be seen that the differences are larger as we approach the horizon.

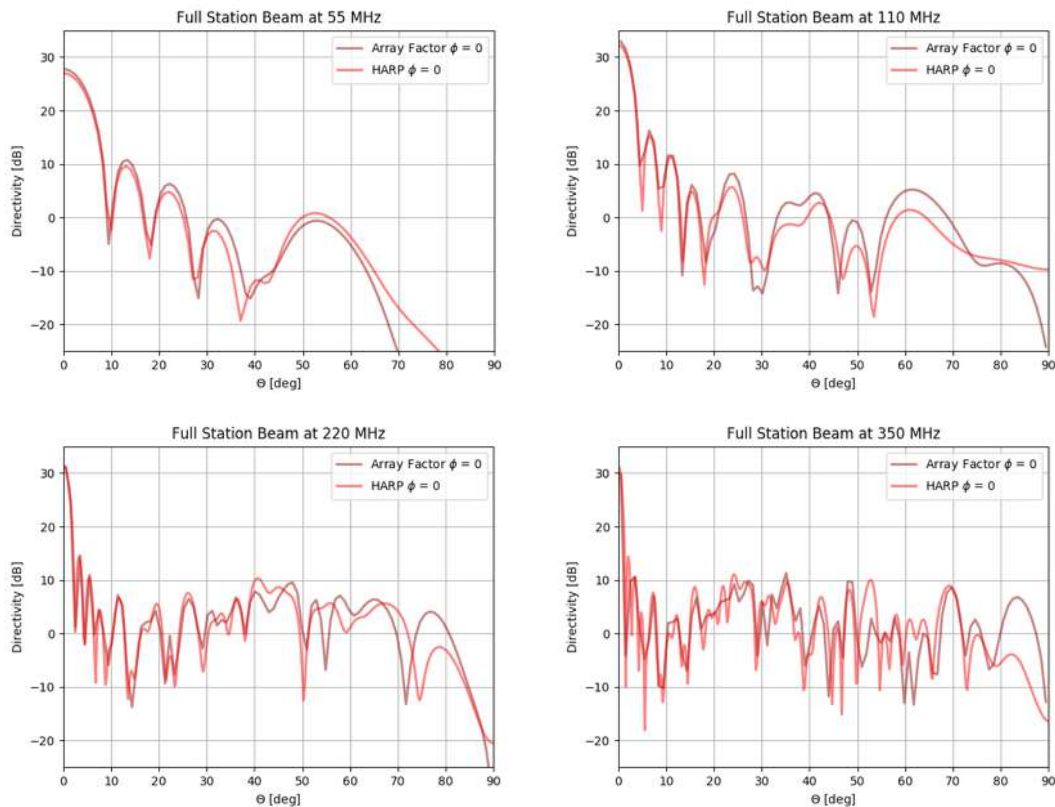


Figure 45: Station beams with and without mutual coupling included at 4 different frequencies.

7.2.1 Mutual coupling, beams and nulling

A typical operation of SKA1-LOW station beams would be nulling strong natural or artificial (narrow or wide) sources. When nulling beams in the presence of mutual coupling it is essential to

understand the effects of mutual coupling via models and or measurements. In **Figure 46** we show the impact on the null if mutual coupling effects are not accounted for in the nulling operation. It is clear that the quality of the null will be substantially degraded if these effects are not properly accounted for. More information on nulling of SKA1-LOW stations can be found in [RD35].

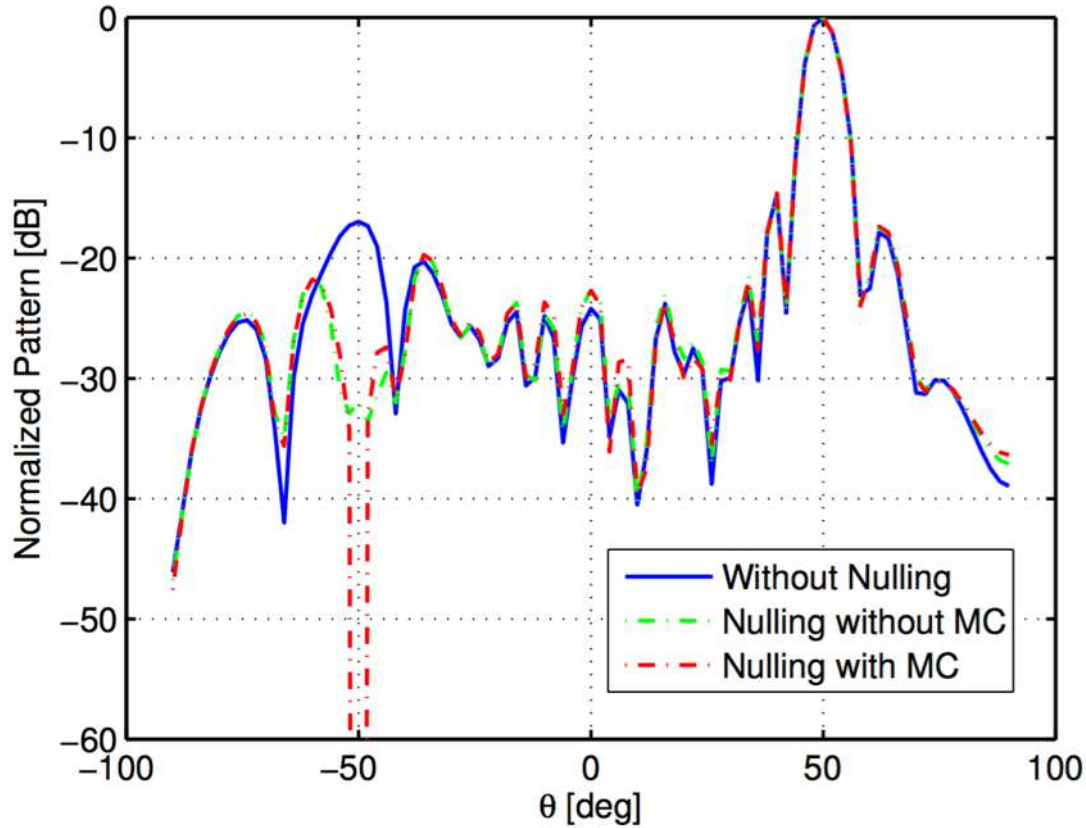


Figure 46: Nulling with SKA1-LOW station accounting for mutual coupling when the main beams is scanned off zenith.

7.2.2 Mutual coupling and array size

The effects of mutual coupling increase with the proximity of elements in the array and it is highly dependent on the specific array layout and size (diameter and number of elements). In this section we highlight this size dependency for random arrays such as a SKA1-LOW station.

Below we show the mean embedded pattern and the standard deviation of all the patterns for a 16 element array and a 256 element array at 200 MHz. Please note that the color scale for the pattern and the standard deviation are different but the same between the 16 element and 256 element array. What this shows is that there is at least 1 order of magnitude difference in the dispersion of the beams between a small 16 element array and a full SKA station.

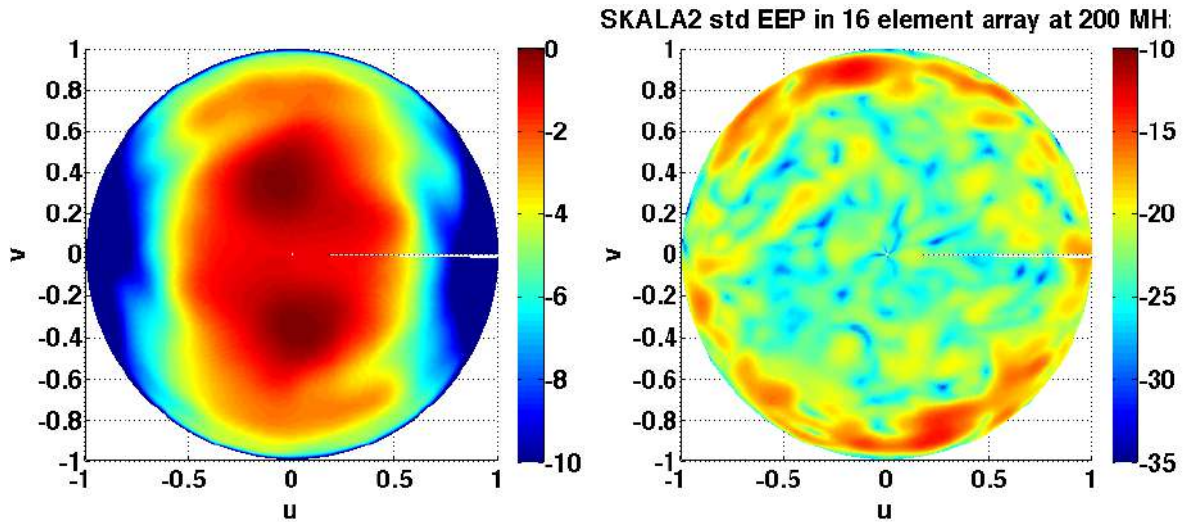


Figure 47: 16 element array (mean embedded pattern (left) and standard deviation (right) of all the patterns in the array in dB).

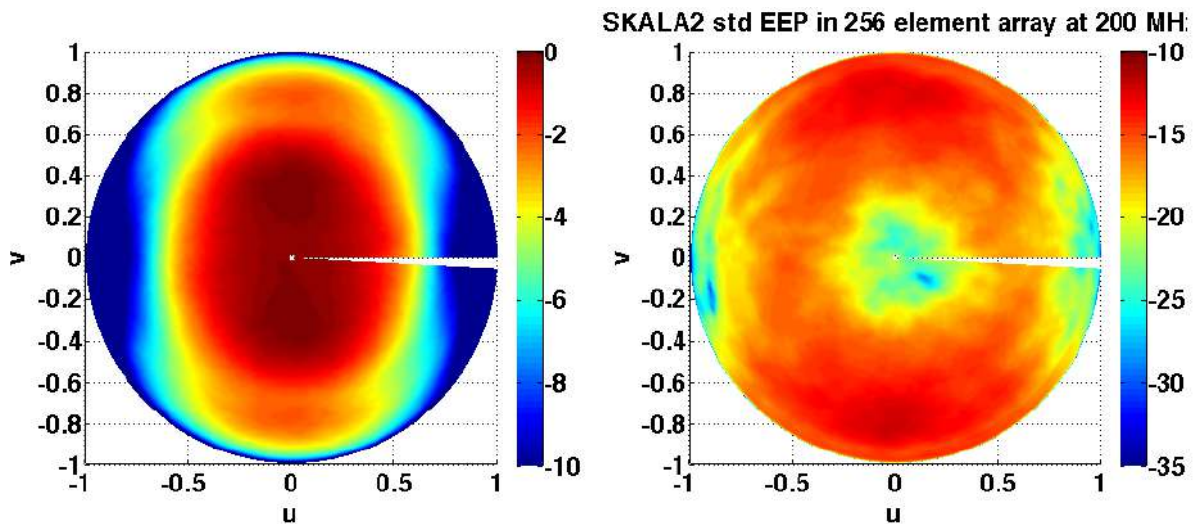


Figure 48: 256 element array (mean embedded pattern (left) and standard deviation (right) of all the patterns in the array in dB).

Furthermore, the spatial scale of the artifacts due to mutual coupling for a small and a large array is different and basically directly related to λ/D with D the diameter of the array. See below for a graphical representation of this effect.

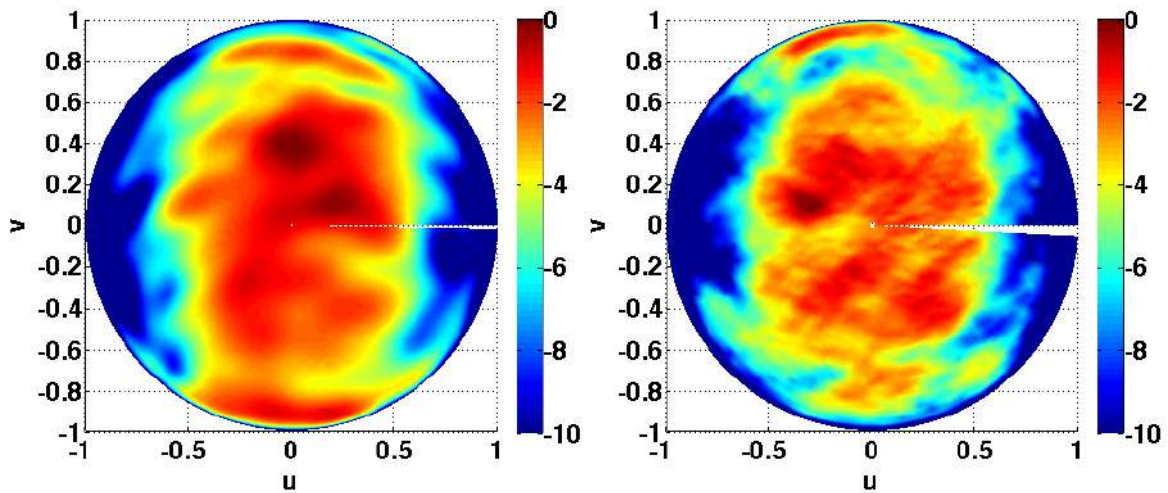


Figure 49: Embedded patterns in dB for 2 individual antennas in a 16 element array (left) and 256 element array (right) at 200 MHz.

We also simulated random arrays containing 10, 32, 100, 317 and 1,000 dipole elements to understand better the link between array size and mutual coupling. The latest has a diameter of 60λ and the population density has been preserved for the other arrays. Figure 50 shows the normalized mean error (across all angles) for the 5 arrays (noe stands for number of elements) versus the radius of influence (RI) i.e. including the mutual coupling with all the other elements of the array, and the errors for smaller RI. This plot shows a clear tendency of decreasing error for larger RI and suggests that for a larger array the size of the RI (normalized to the array size) needed to achieve a given error is lower than for smaller arrays.

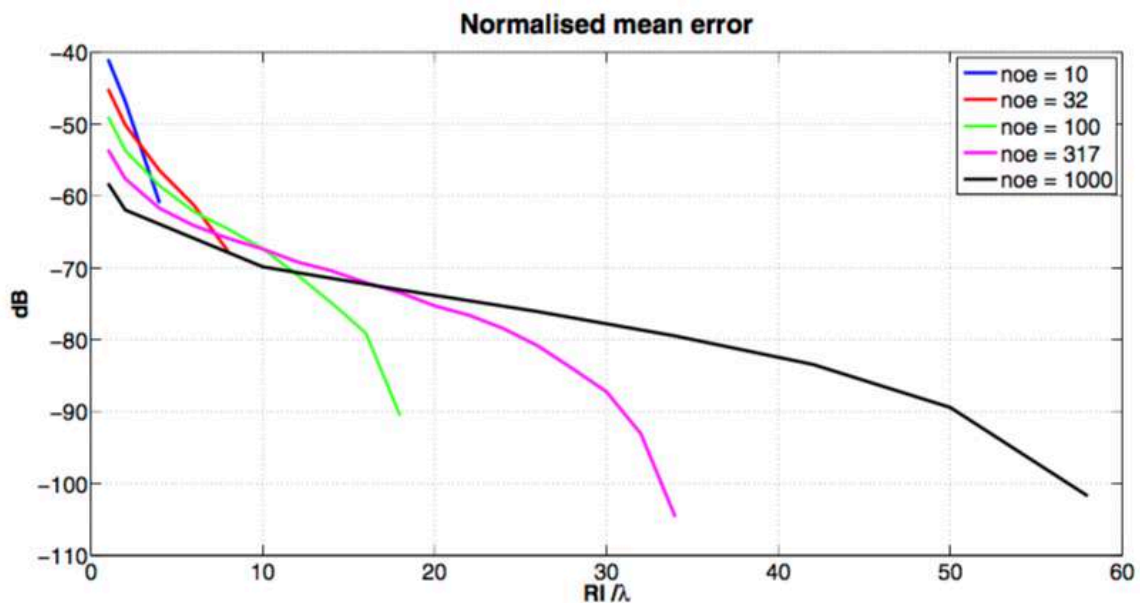


Figure 50: Convergence of the effects of mutual coupling for different number of elements in the array (of increasing size) and an increasing radius of influence (radius of the area around each individual antenna in where the effects of mutual coupling are accounted for). The error across the whole sky of the station beam is shown here.

7.2.3 Polarization and IXR

The calculation of the station IXR [RD36] shows the IXR of the station beam when pointed to a specific direction of the sky. Therefore, the following plots account for the effects of mutual coupling as well as antenna effects. What the polar plots below show is the IXR across the whole sky, so every point in the graphs represents the array scanning to that direction with the centre of the plot corresponding to the zenith of the array.

The overall minimum IXR is always above 10 dB (see **Figure 56**) with IXR values at zenith as high as 60 dB. This is due to projection effects on the antenna. As seen from zenith, the antenna represents a very orthogonal pair of dipoles while as one approaches larger incident angles this orthogonality is lost. The point of minimum IXR is always found at the edge of the field of view although is not at the same scanning angle at every frequency as shown in **Figure 51 - Figure 55**. The IXR of the station fluctuates around the IXR of the isolated antenna, although mutual coupling effects can enhance/degrade slightly this at certain frequencies, especially at low frequencies where these effects are stronger.

The average IXR within the field of view (± 45 deg. cone from zenith) is around 40 dB below 100 MHz and 30 dB from 100 to 350 MHz. The IXR contours show a circular symmetry.

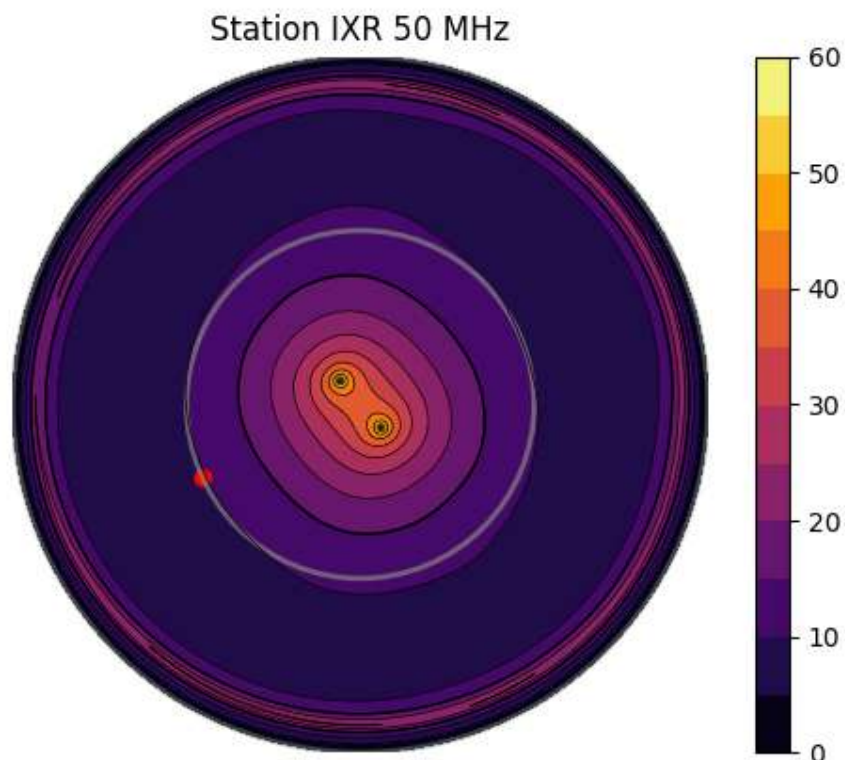


Figure 51: Station IXR at 50 MHz. The grey line marks 45 degrees. The solid black line marks the 15 dB IXR requirement. The red dot marks the point of minimum IXR within the ± 45 deg. cone from zenith.

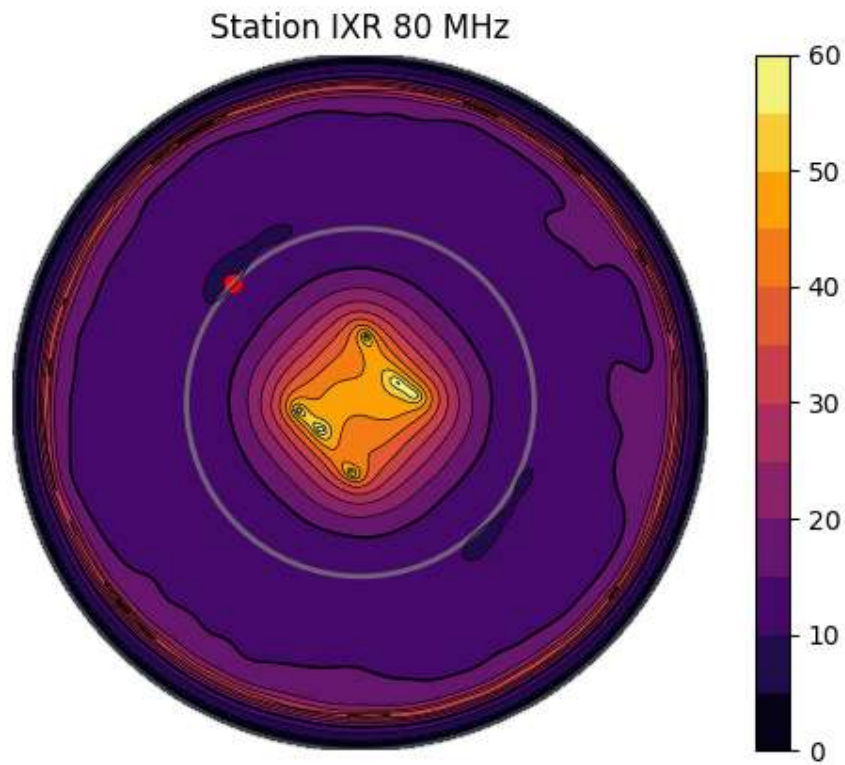


Figure 52: Station IXR at 80 MHz. The grey line marks 45 degrees. The solid black line marks the 15 dB IXR requirement. The red dot marks the point of minimum IXR within the +/- 45 deg. cone from zenith.

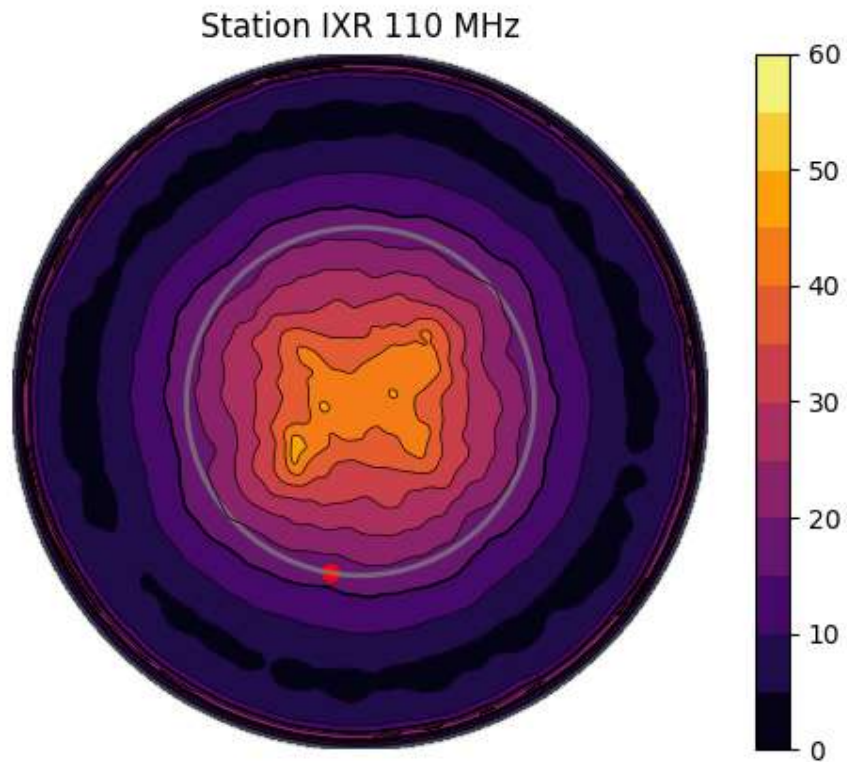


Figure 53: Station IXR at 110 MHz. The grey line marks 45 degrees. The solid black line marks the 15 dB IXR requirement. The red dot marks the point of minimum IXR within the +/- 45 deg. cone from zenith.

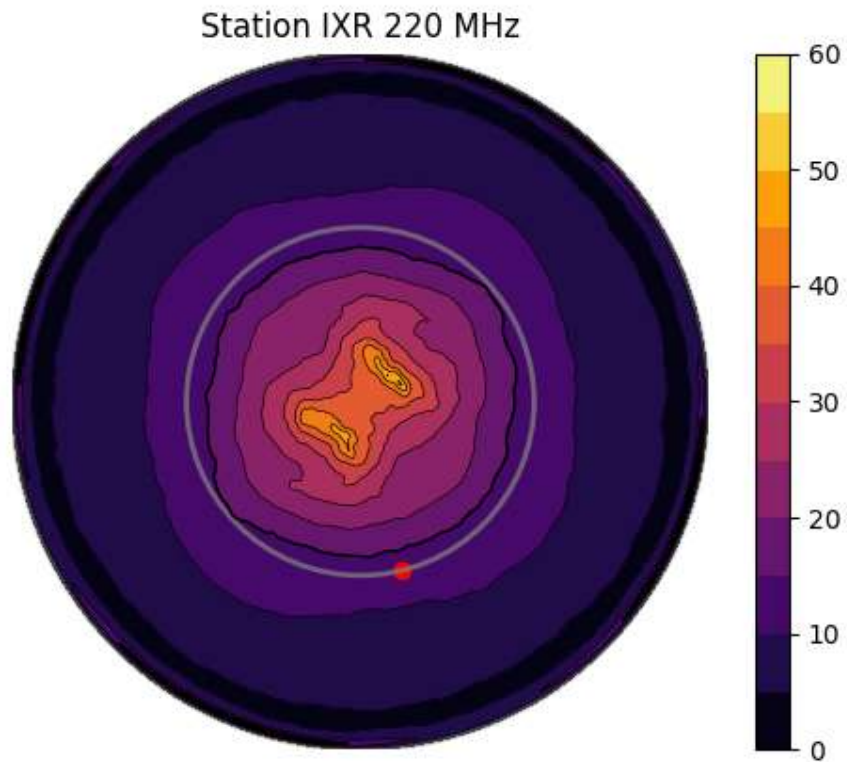


Figure 54: Station IXR at 220 MHz. The grey line marks 45 degrees. The solid black line marks the 15 dB IXR requirement. The red dot marks the point of minimum IXR within the +/- 45 deg. cone from zenith.

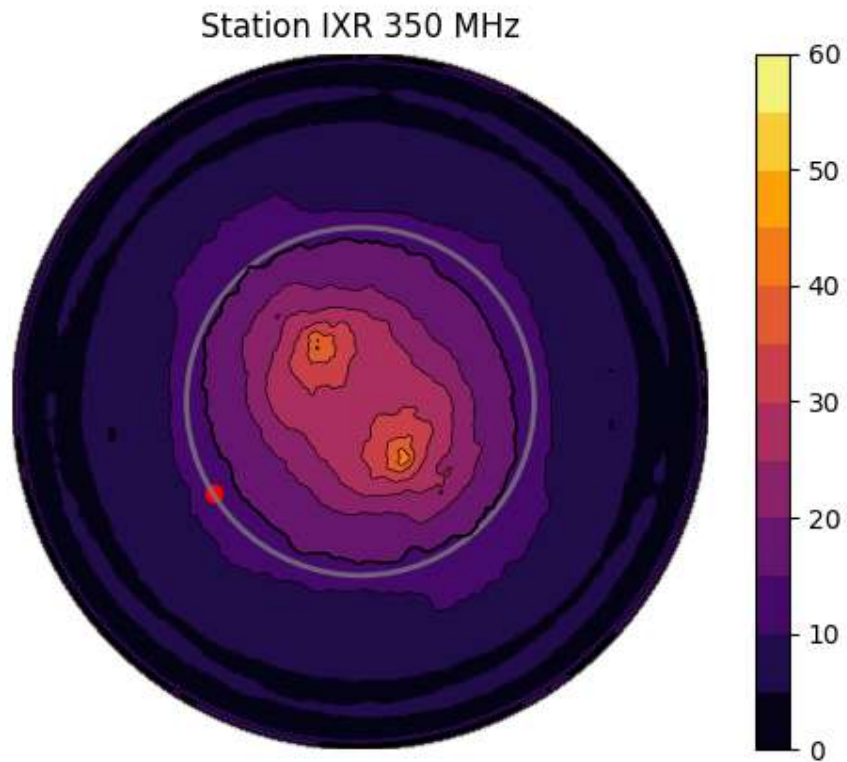


Figure 55: Station IXR at 350 MHz. The grey line marks 45 degrees. The solid black line marks the 15 dB IXR requirement. The red dot marks the point of minimum IXR within the +/- 45 deg. cone from zenith.

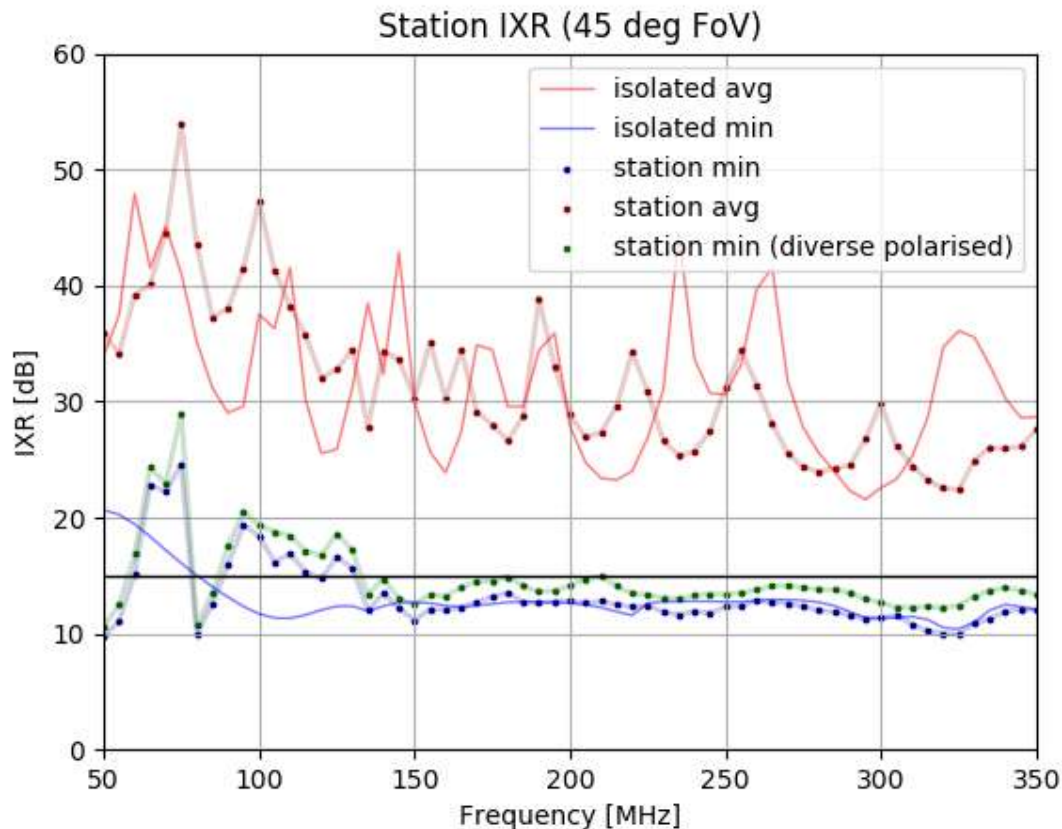


Figure 56: Station IXR across frequency. Minimum and average values within the field of view (+/- 45 deg cone from zenith) are shown. It is worth noting that the minimum values always occur at the edge of the field of view but not at the same point at every frequency. Also shown is the minimum IXR if a simple polarization diversity algorithm is applied to the antenna's rotational positions [RD37]. For comparison the IXR values for the isolated element are also shown.

Furthermore, it is worth noting, as described in [RD38] that for an IXR of 15 dB, we find that the thermal noise level in the final image may be raised by a factor 1.69. Although this may seem significant, the images with the highest dynamic range made so far have a noise floor that lies between a factor 1.5 and 2.

7.3 Sub-station beams

Although there are no specific requirements for sub station beams (beams formed by a group of antennas inside a field station), there is the intention to potentially access these beams. The LFAA architecture allows for the formation of these beams including any set of antennas in that subarray. In this station we present a brief summary of the expected beam response of these substations for different cases.

In **Figure 57** we present the 4 different configurations of 16 elements analysed here. 3 configurations are aggrupation of antennas in the central area of the field station and the final one represents an aggrupation of antennas at the edge of the field station. Independently of the TPM

these antennas may be connected to, these sub arrays could be formed. Therefore, more work will be needed to establish the quality of specific beams to target a specific science case.

It is known [RD39] that the effects of mutual coupling won't randomize out as well for smaller arrays. Furthermore, it appears evident from **Figure 58 - Figure 61** that, again as expected, the side lobe level increases for the substations and could potentially be an issue, especially at the high end of the band. Finally, it is worth noting that the sub station beams, even if for the same number of elements, could be quite different from each other depending on the layout of the substation, including substantially different beam widths (and therefore directivity and sensitivity). Obviously a careful consideration of the choice of these substation layouts is needed since the field station layout has not been designed to provide optimum substation beams.

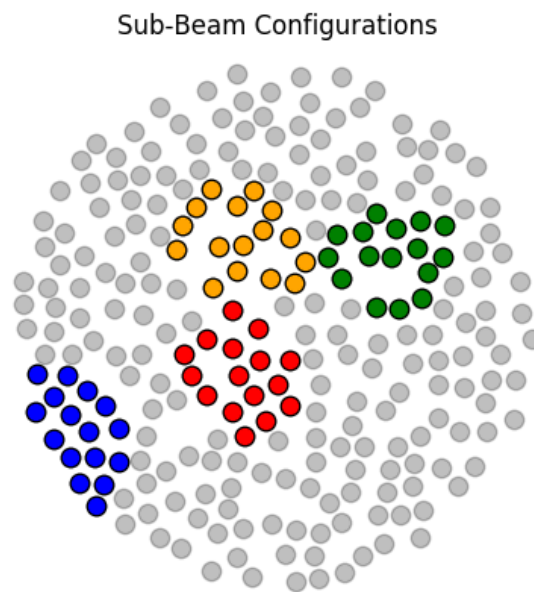


Figure 57: Sub-station configurations analyzed in this section.

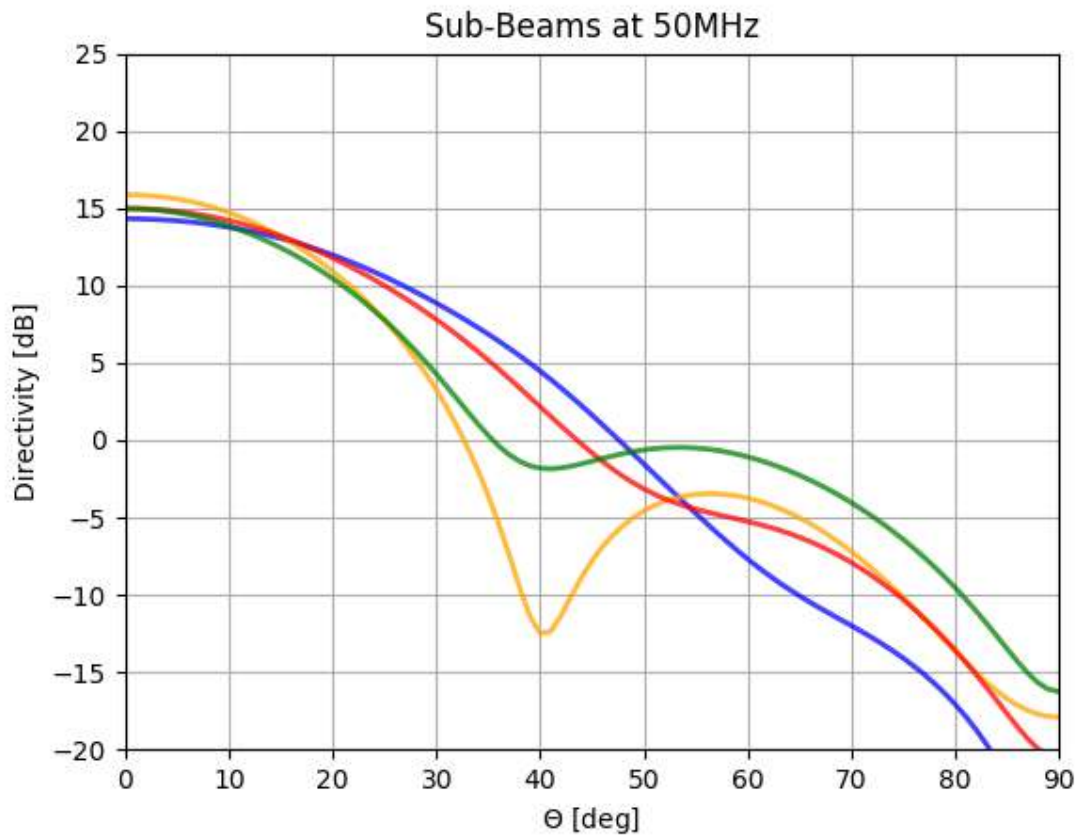


Figure 58: Sub-station beams at 50 MHz. The different colors represent the different configurations presented in **Figure 57**.

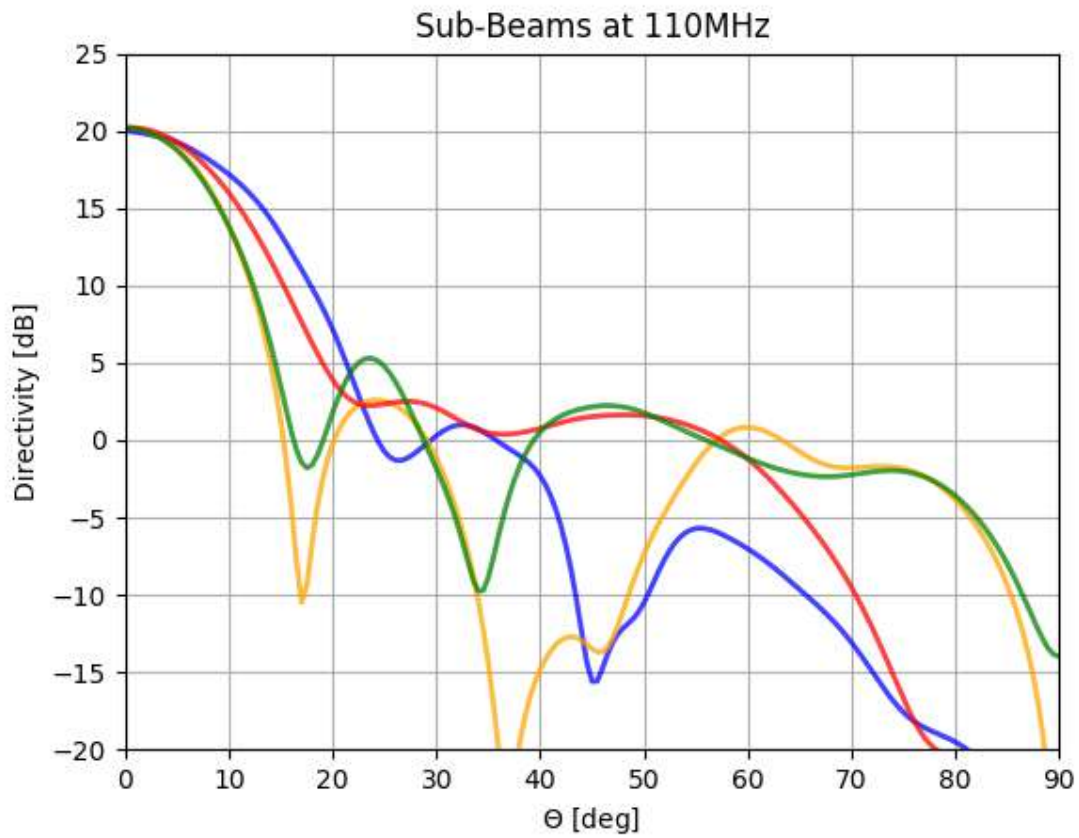


Figure 59: Sub-station beams at 110 MHz. The different colors represent the different configurations presented in **Figure 57**.

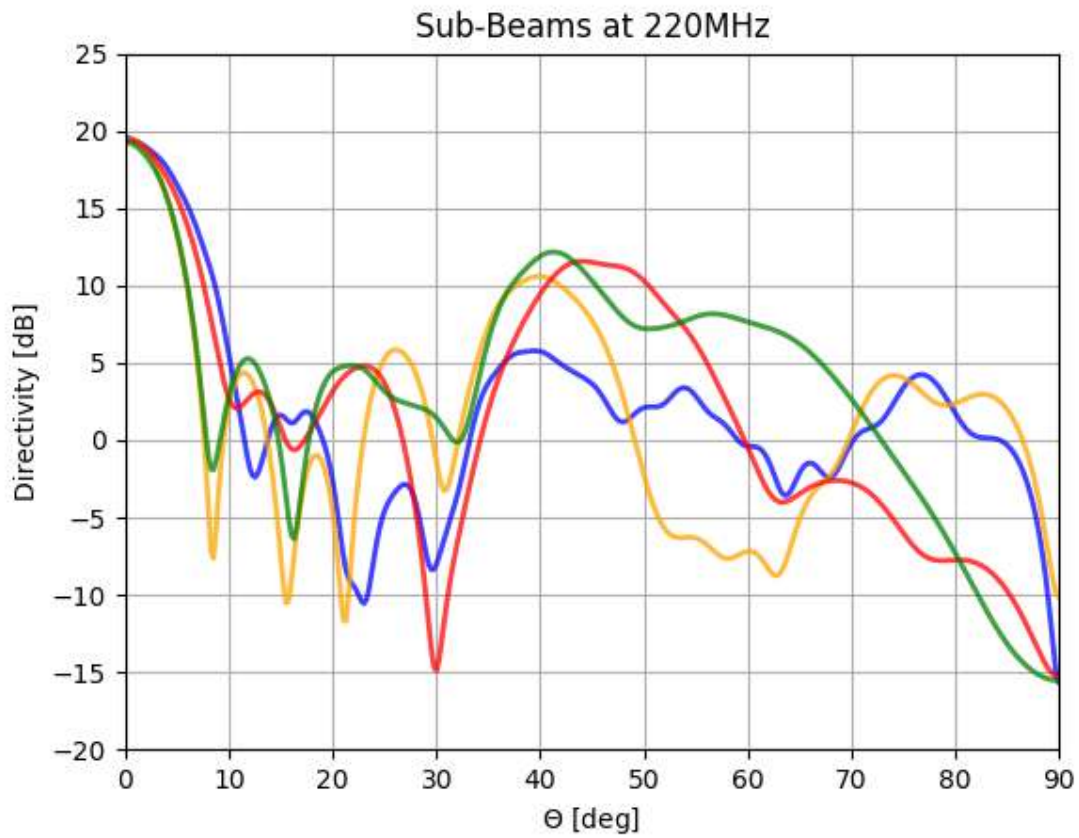


Figure 60: Sub-station beams at 220 MHz. The different colors represent the different configurations presented in **Figure 57**.

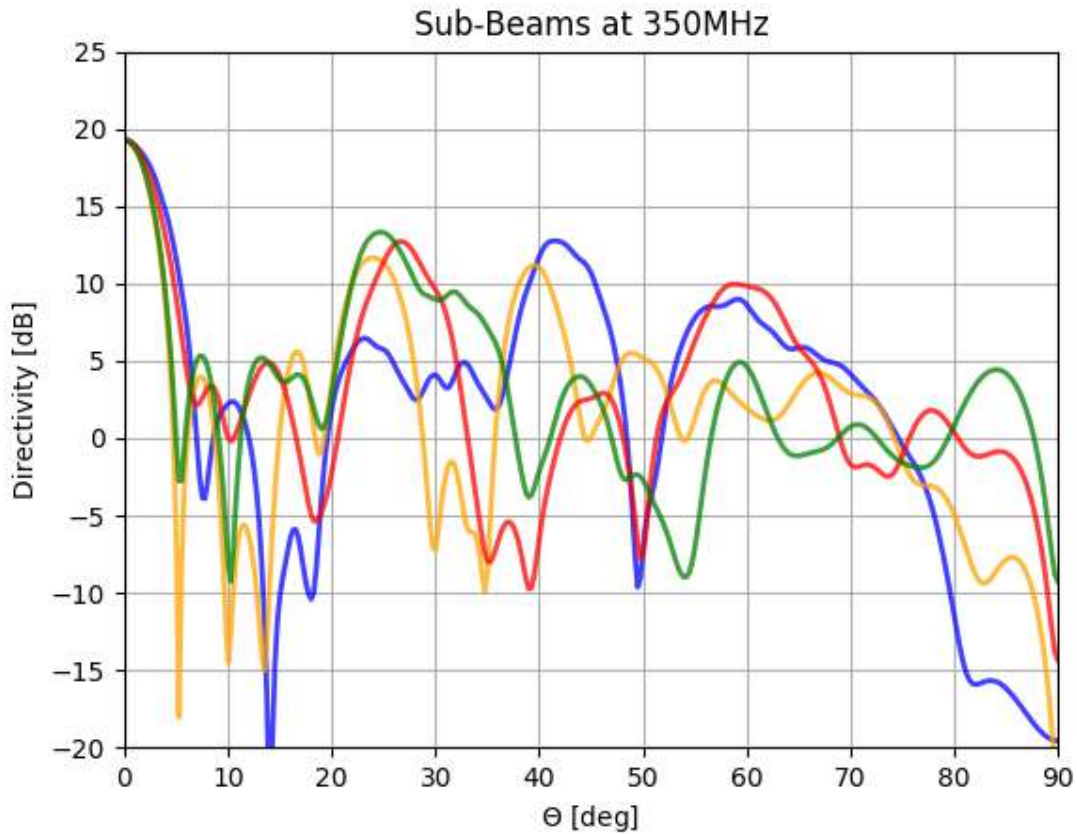


Figure 61: Sub-station beams at 350 MHz. The different colors represent the different configurations presented in Figure 57.

7.3.1 Spatial Smoothness and array beam modelling and predictability (AAVS1)

Our ability to model the station beam with a few coefficients is critical for the calibration of the instrument. The spatial smoothness of the station beam limits this ability and will be dominated by the layout of the station, that defines the main beam and by mutual coupling, rather than by artefacts of the antenna beam. We have used Zernike polynomials with orders $M = N = 2$ to 5 to model the field pattern of the AAVS1 station. The AAVS1 station and the SKA1-LOW station (practically the same random layout and filling factor) should have a very similar performance in this metric. The error is calculated in the main beam down to -6dB from the peak value. The results are shown below. See [RD40] for more information. This shows a very low error for a relatively low number of coefficients. The use of Zernike polynomials is inspired by the fact that a SKA1-LOW station is in essence a sampled circular aperture like a dish with errors in its panels.

Freq. [MHz]	$M=N=2$		$M=N=3$		$M=N=4$		$M=N=5$	
	$\theta_0 = 0^\circ$	$\theta_0 = 45^\circ$						
50	0.0009	0.0030	6.5579e-05	0.0003	1.3236e-05	0.0001	1.1911e-05	3.9171e-05
70	0.0010	0.0027	3.3455e-05	0.0002	2.9338e-05	0.0002	1.6988e-05	5.6419e-05
110	0.0008	0.0034	0.0001	0.0003	1.6498e-05	0.0001	1.6247e-05	3.6796e-05
250	0.0019	0.0058	0.0002	0.0043	6.0895e-05	0.0003	2.8421e-05	0.0001
350	0.0049	0.0066	0.0004	0.0016	0.0001	0.0006	6.326e-05	0.0001

Table 10: RMS error – spatial smoothness for a set of frequencies and 2 different scan angles (zenith and 45 degrees).

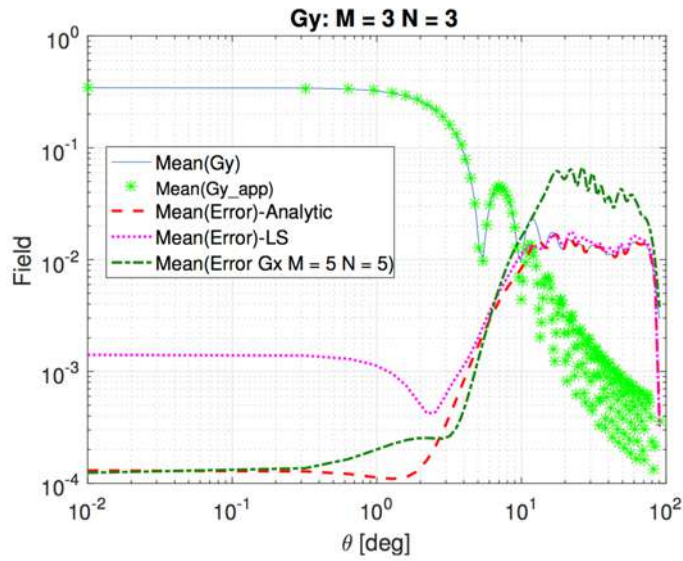


Figure 62: Station beam (in log-log scale) and model.

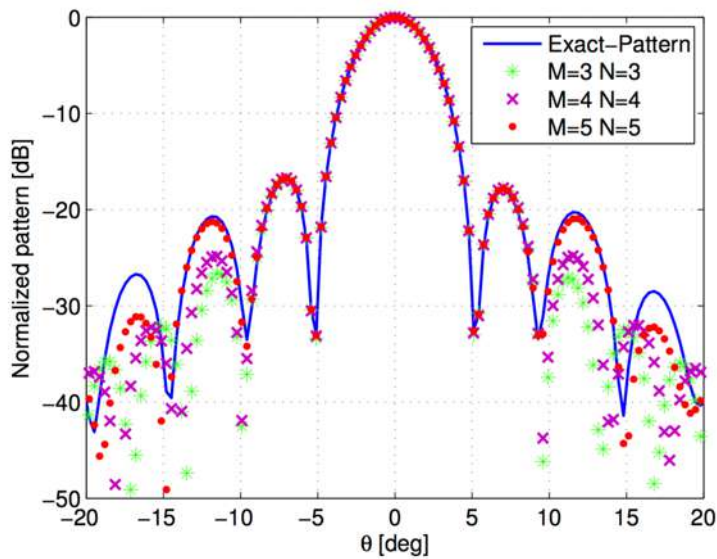


Figure 63: Station beam scanned at zenith; exact and modeled with different orders.

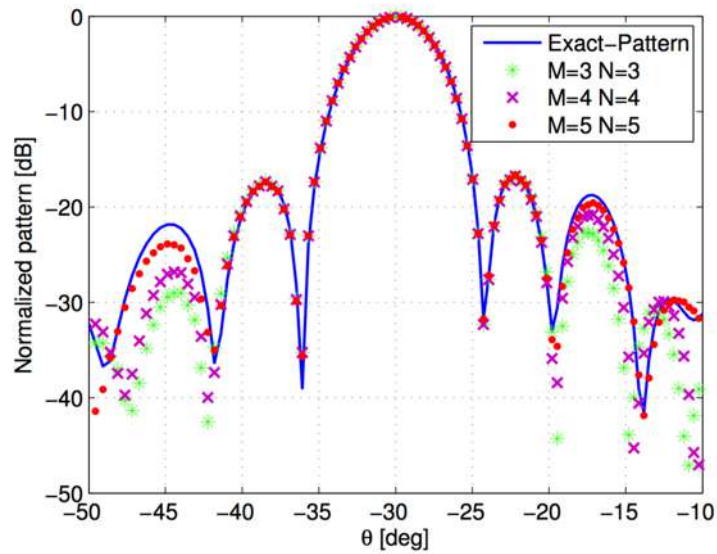


Figure 64: Station beam scanned at 30 degrees from zenith; exact and modeled with different orders.

A follow up of this work will analyse the residual errors and their relevant scales (spatial and spectral) for an EoR observation.

7.3.2 Smoothness of the Embedded Patterns (AAVS1 and SKALA4)

This section describes different smoothness criteria (see [RD7] for more information) for the embedded element patterns of the station.

7.3.2.1 Deviation from idealized pattern

The average Embedded Element Pattern $EEP_{avg}(\vartheta, \varphi)$ is chosen as an Idealized Pattern for each frequency. We then try to calculate the deviation of all the EEPs in a station from that one. It should be noted that the subscript avg denotes the average across array elements. **Figure 65** shows an example of average EEP for AAVS1 SKALA2 array at 120 MHz.

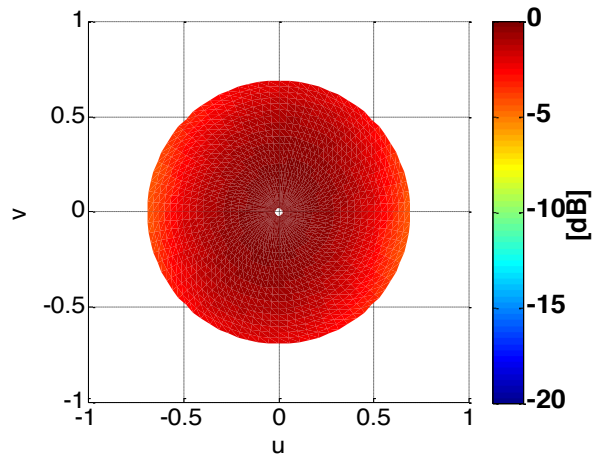


Figure 65: Example of average EEP at 120 MHz.

In particular, all the patterns have been divided by the $EEP_{avg}(\vartheta, \varphi)$

$$p_i(\vartheta, \varphi) = \frac{EEP_i(\vartheta, \varphi)}{EEP_{avg}(\vartheta, \varphi)} \quad (1)$$

This quantity has then been divided by its mean (across observation angle). Finally, one has been subtracted obtaining

$$q_i(\vartheta, \varphi) = \frac{p_i(\vartheta, \varphi)}{\bar{p}_i(\vartheta, \varphi)} - 1 \quad (2)$$

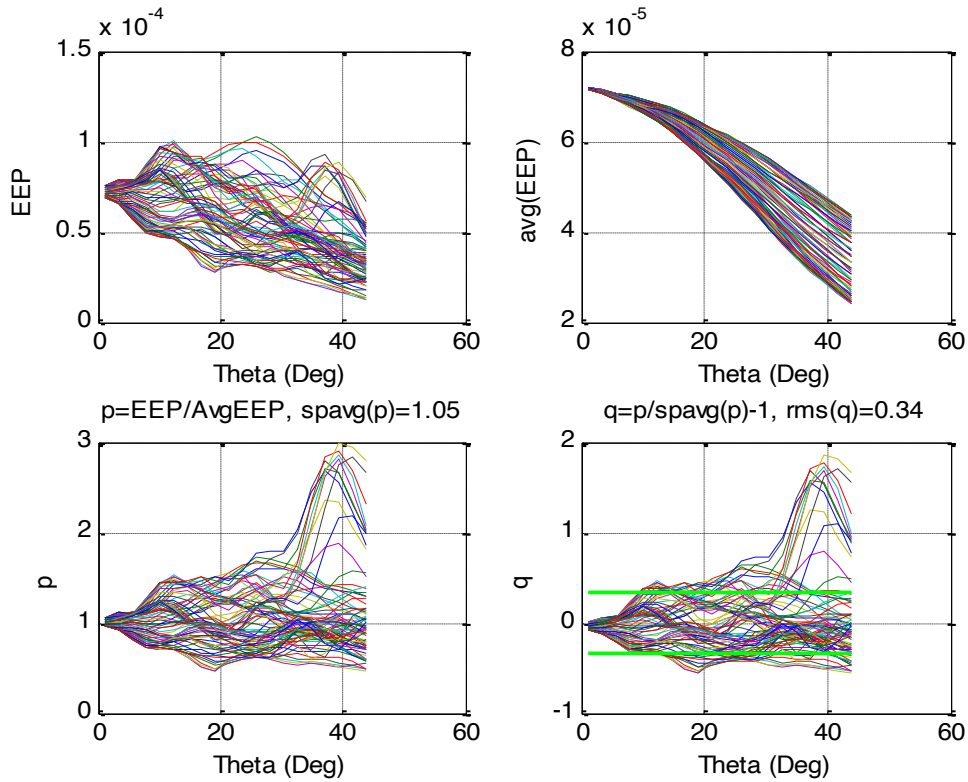


Figure 66: Pattern smoothness metric for the first element of the AAVS1 SKALA2 Array at 120 MHz. The scale of the two upper axes is $|E|^2$, where E is the E-field pattern. The different colors identify the various azimuth angles.

Figure 66 shows the values of the $p_i(\vartheta, \varphi)$ and $q_i(\vartheta, \varphi)$ quantities for the first element of the AAVS1 array. This data have been arranged on the histogram of Figure 67 (left). The histogram on the right contains all the elements.

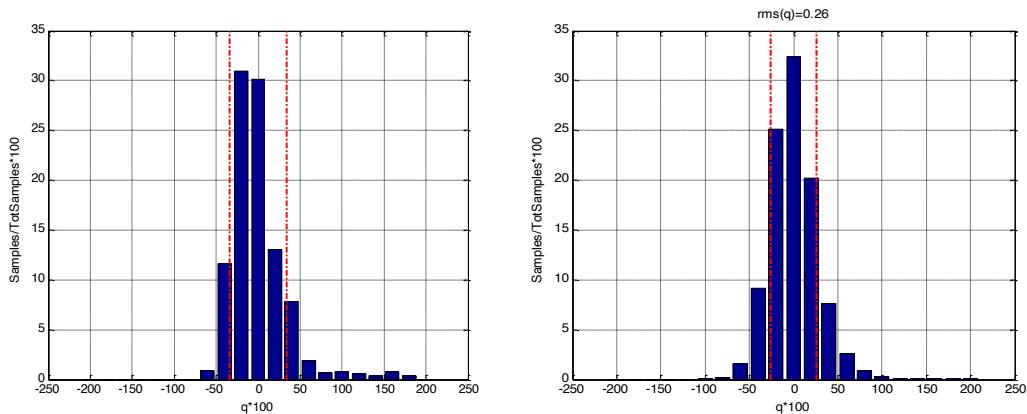


Figure 67: Histograms of the $q_i(\vartheta, \varphi)$ data for the first AAVS1 element (left) and all elements (right).

A Gaussian distribution of the $q_i(\vartheta, \varphi)$ is apparent in Figure 67: , therefore, the root-mean-square of the data can be adopted as a more synthetic figure of merit.

Frequency [MHz]	$Rms(q_i(\vartheta, \varphi))$	$10*\log_{10}(1+q_i(\vartheta, \varphi))$
80.64	0.22	0.86 dB
120.32	0.26	1 dB
152.46	0.35	1.3 dB
199.68	0.23	0.9 dB

Table 11: RMS of histograms for all the elements of AAVS1 array.

7.3.2.2 The first derivative

The first derivative criterion is described in [RD7] and has been implemented and verified against the reference data reported in the same document. The same procedure has been then applied to the average Embedded Element Pattern of the AAVS1 array (an example of average EEP is shown in Figure 68). In particular the gradient calculation has been performed on amplitude data ($|E|$, where E is the radiated electric field). Before making the gradient, the data have been also normalized to their maximum value across the observation angle in order to compare them to the reference solution (analytical dipole at $\lambda/4$ from an infinite conducting ground). The histogram for the reference solution is reported on the left side of Figure 68: , the maximum value is about 1. The histogram computed on the average EEP of the AAVS1 at 120 MHz is instead reported on the right side for comparison. The maximum value is 0.97 in this case.

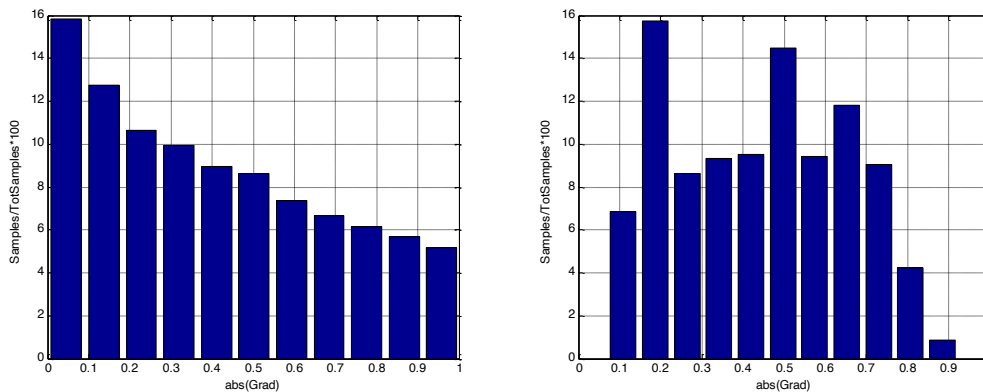


Figure 68: Histograms for the gradient of an analytical dipole placed at $\lambda/4$ from an infinite conducting ground (left) and for the Average Embedded Element Pattern of the AAVS1 array at 120 MHz (right).

Table 4 reports the gradient value across frequency. The reference value from the analytical solution mentioned above is equal to one at all frequencies.

Frequency (MHz)	Max. Grad for Avg. EEP (rad^{-1})
80.64	0.95
120.32	0.9
152.46	0.9
199.68	1.4

Table 12: Maximum gradient of the average Embedded Element Pattern of the AAVS1 array. The reference value from the analytical solution is equal to 1 at all frequencies.

7.3.2.3 Modelling of the Embedded Element Patterns

The embedded element patterns of all the antennas are different as expected for a random array layout. Furthermore, the structure of the features in the embedded beams tend to show scales of the order of λ/D , with D being the station effective diameter. Our ability to model and predict these

embedded elements is very important for the station calibration [RD4], since one needs to assume a level of knowledge of these beams to calculate the correct weights for the beam-former.

A possible approach is to use the well-known spherical harmonic expansions to decompose and reconstruct the complex embedded patterns. Another possibility, even more compact, would be to use the coefficients of the Macro Basis Functions used in HARP. For the later, storing the beam information for all the EEPs of 1 station would require of the order of a few tens of complex coefficients (~ 15 , although this is frequency dependent) \times 256×256 (MBF interactions matrix) \times 400 frequency channels, giving ~ 6 GB per station using double precision complex numbers.

Spherical harmonics are typically used to describe full sphere problems and have been used in the past for array and antenna applications [RD39]. Furthermore, they are implemented by several of the commercial codes capable of simulating the SKA1-LOW stations.

Furthermore, it is worth noting that the log-periodic antenna works as a collection of simple dipoles in and out of phase, which makes it relatively easy to model (eg. [RD41][RD31], amongst a vast amount of literature on the topic). With the main difference with respect to a standard dipole being that the active region (region of the antenna supporting the currents at a given frequency) is made of multiple dipoles (~ 3 dipoles support the strongest currents) and moves up and down the antenna with frequency (see figure below).

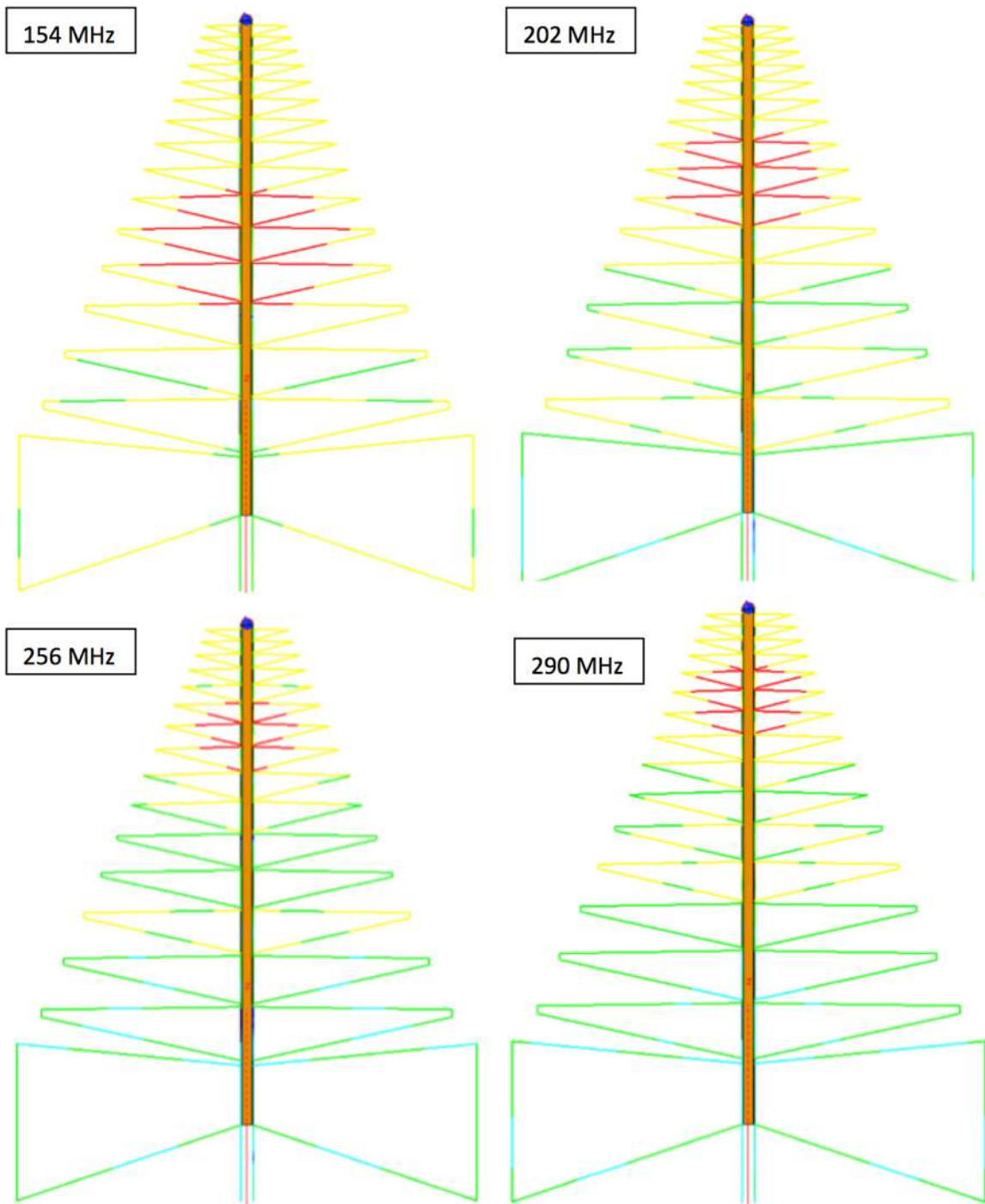


Figure 69: Antenna active region moving with frequency.

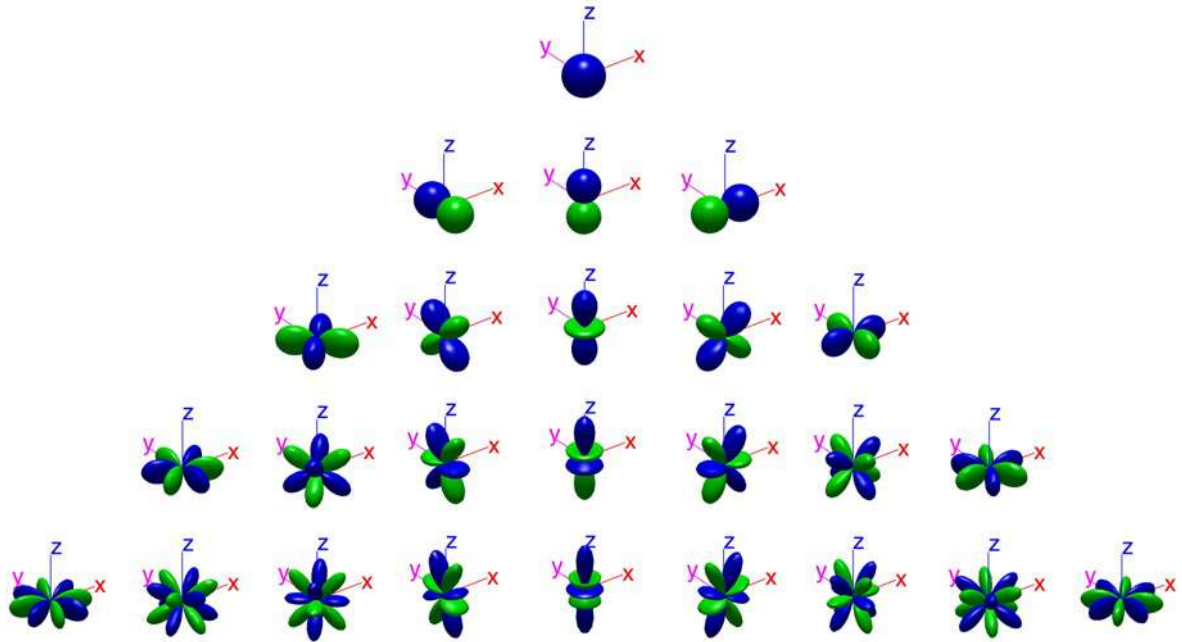


Figure 70: Complex spherical harmonics functions (Image credit: Mathworks).

In here we show 2 examples of the use of spherical harmonics expansion to represent the embedded patterns of the station, together with the residual error when one reconstructs the station pattern using those modelled beams.

Furthermore, using low order models opens the possibility to do effective sky based or artificial source based beam measurements for the validation/correction of the simulated beams.

The AAVS1 station beam (pointing at zenith) has been reconstructed using models of the embedded element patterns using spherical harmonics basis functions of the orders shown below. The average error across the sky between the reconstructed station beam and the ideal (simulated) beam has been computed. We would like to point out that since the models are of the embedded element patterns and then the station beam is reconstructed using those models, we don't expect different levels of error for other scan angles. The results are shown below. For a similar accuracy on individual beams higher orders would be required.

<i>Freq. [MHz]</i>	<i>Order of SH: 3</i>	<i>Order of SH: 4</i>	<i>Order of SH: 5</i>	<i>Order of SH: 6</i>	<i>Order of SH: 7</i>	<i>Order of SH: 8</i>	<i>Order of SH: 9</i>	<i>Order of SH: 10</i>	<i>Order of SH: 12</i>	<i>Order of SH: 15</i>
50	-39.24	-39.65	-40.95	-41.77	-42.78	-43.50	-44.42	-45.32	-46.20	-48.13
70	-41.59	-43.41	-44.23	-46.79	-49.02	-51.36	-53.50	-54.93	-58.98	-63.27
110	-42.14	-42.55	-43.66	-45.51	-45.86	-47.25	-47.46	-48.51	-49.86	-51.64
250	-33.08	-34.19	-36.34	-37.04	-39.07	-39.86	-41.29	-41.40	-42.24	-43.31
350	-31.51	-32.19	-32.79	-33.42	-34.48	-35.13	-37.02	-37.52	-39.44	-41.14

Table 13: Number of Spherical Harmonic coefficients 3:10, 12 and 15, at 5 different frequencies. The average error across the sky is in dB.

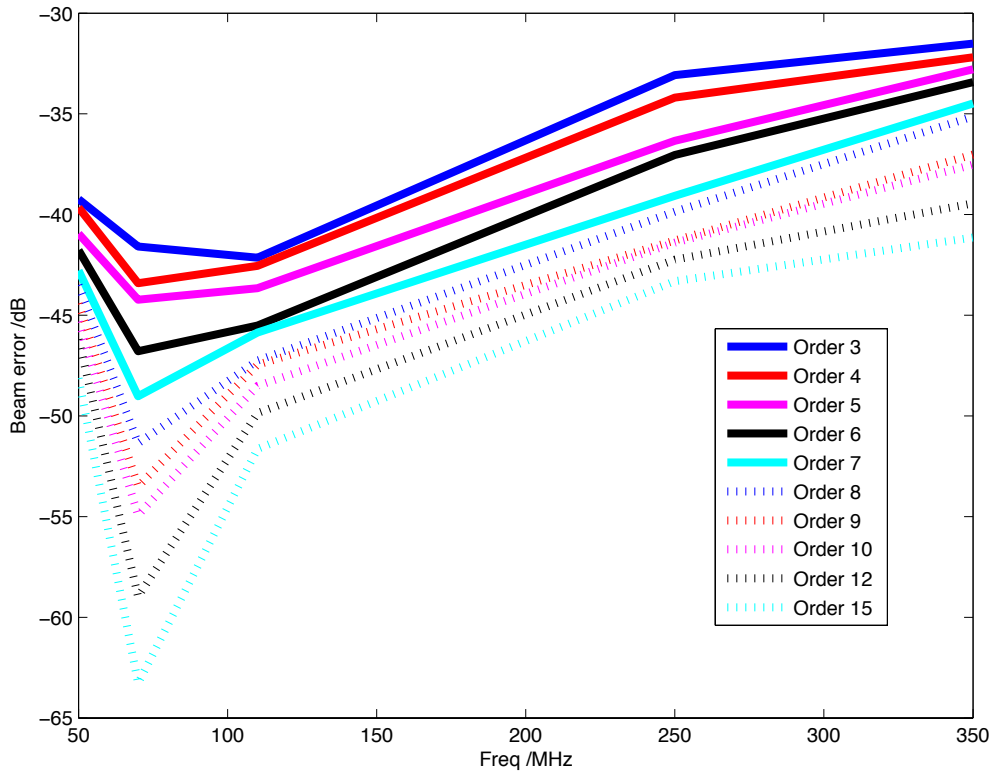


Figure 71: Complex spherical harmonics full sky beam reconstruction error wrt to real beam (for different orders of decomposition).

Using a SKA1-LOW station we repeated the same procedure and here we show the details of those residual errors and their spatial scales.

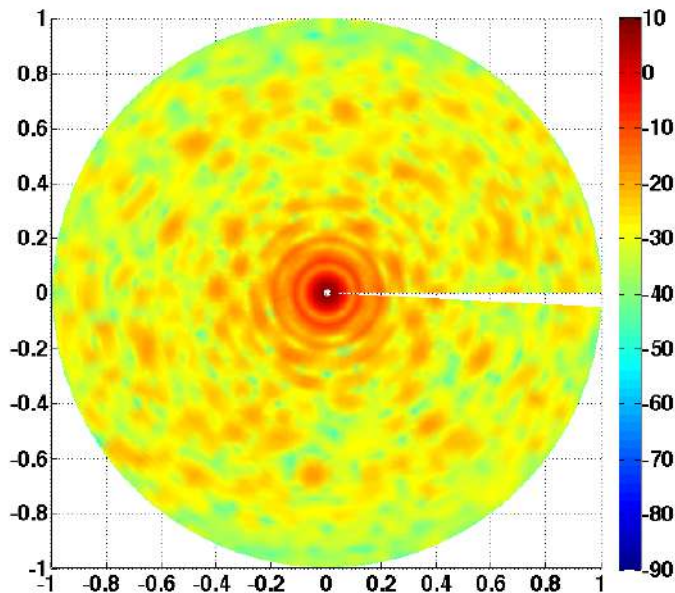


Figure 72: Full sky station beam scanned at zenith (110 MHz) in dB.

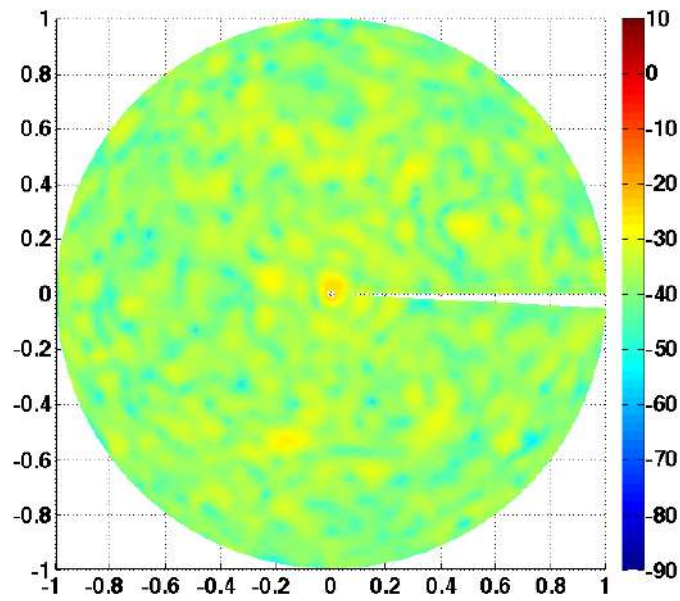


Figure 73: Error of the reconstructed station beam using spherical harmonic models of the embedded patterns or order 5 with respect to the full sky station beam scanned at zenith (110 MHz) in dB.

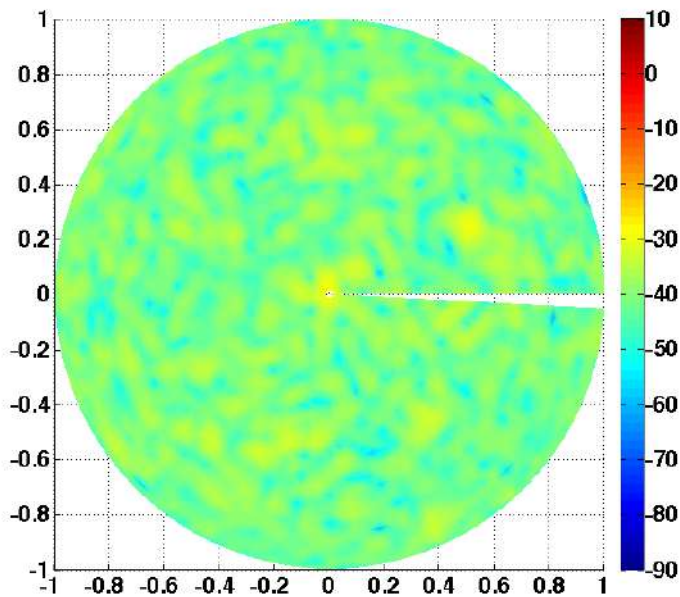


Figure 74: Error of the reconstructed station beam using spherical harmonic models of the embedded patterns or order 10 with respect to the full sky station beam scanned at zenith (110 MHz) in dB.

7.4 Budget of mechanical tolerances on the EM performance

In this section we present an analysis of the effect of the main potential deviations from the ideal EM design due to mechanical tolerances on SKALA4. In all cases we present the worst case found when applying a uniform distribution of deviations from the ideal design within the ranges indicated. This analysis is done for the individual antenna due to limitations in the available software codes to do this for the full array in the available time with the latest SKALA4 antenna design. We expect that these tolerances will mainly affect the antenna response rather than the coupling and therefore this analysis should be a good indicator of expected effects in the station behaviour.

7.4.1 Rotational alignment between polarisations

In this section we present the results of rotational misalignments between polarizations of ± 1 degrees. This is a pessimistic assumption for what we expect to find on the antenna. The results indicate a minor impact on the main antenna parameters (directivity, polarization metric, S11).

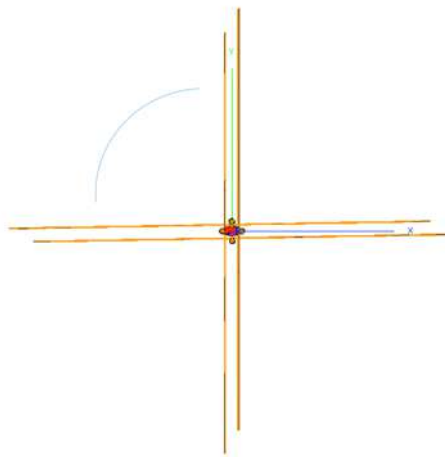


Figure 75: View of the misalignment angle from above.

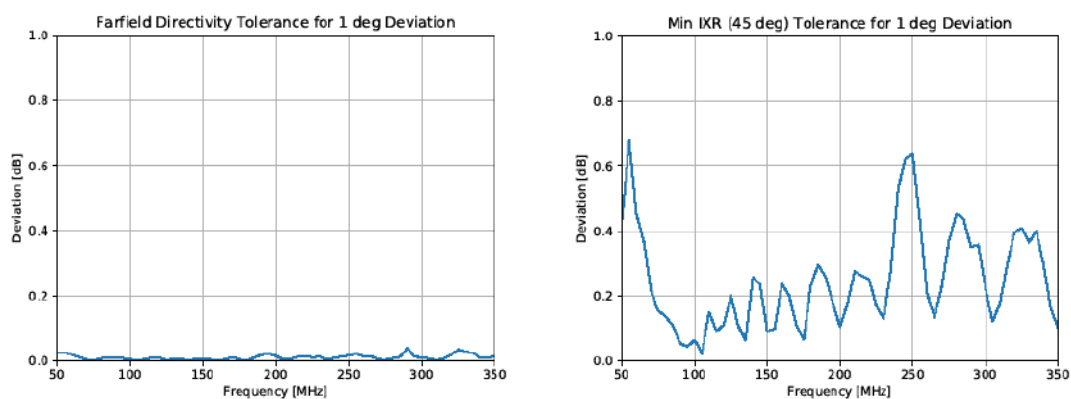


Figure 76: Effect of a ± 1 degree rotational misalignment between polarizations of the antenna on the zenith directivity (left) and the minimum IXR within the field of view (right) across frequency. Absolute deviations are shown.

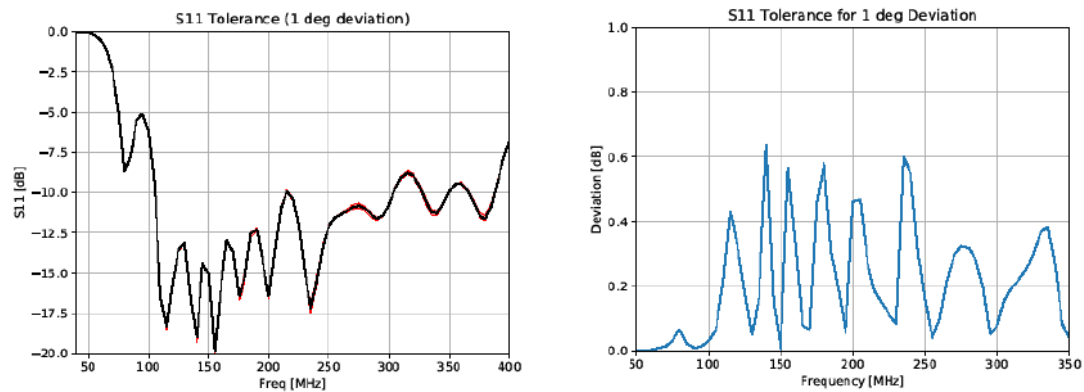


Figure 77: Effect of a +/- 1 degree rotational misalignment between polarizations of the antenna on the S11 (left) and the absolute deviation of S11 (right) across frequency.

7.4.2 Vertical alignment

In this section we present the results of vertical misalignments of +/-1 degrees. This is a realistic assumption for what we expect to find on the antenna. The results indicate a moderate impact on the main antenna parameters (directivity, polarization metric, S11) with the largest deviations found in the polarization metric and S11.

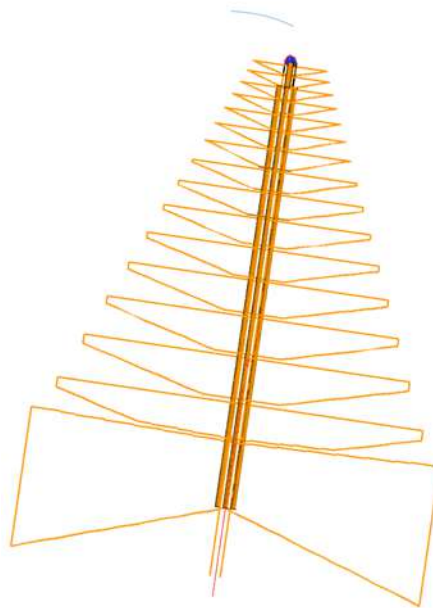


Figure 78: Side view of the vertical misalignment angle.

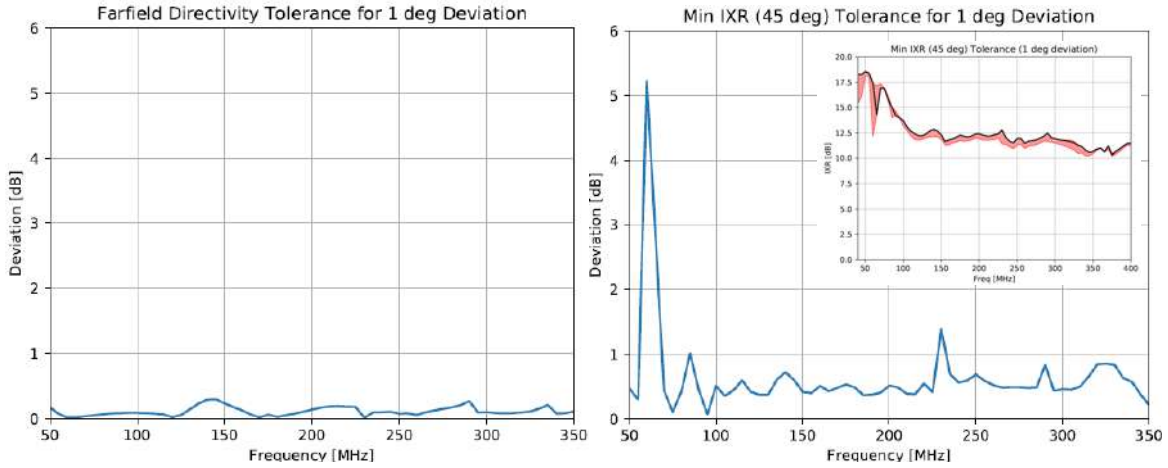


Figure 79: Effect of a +/- 1 degree vertical misalignment on the zenith directivity (left) and the minimum IXR within the field of view (right) across frequency. Absolute deviations are shown.

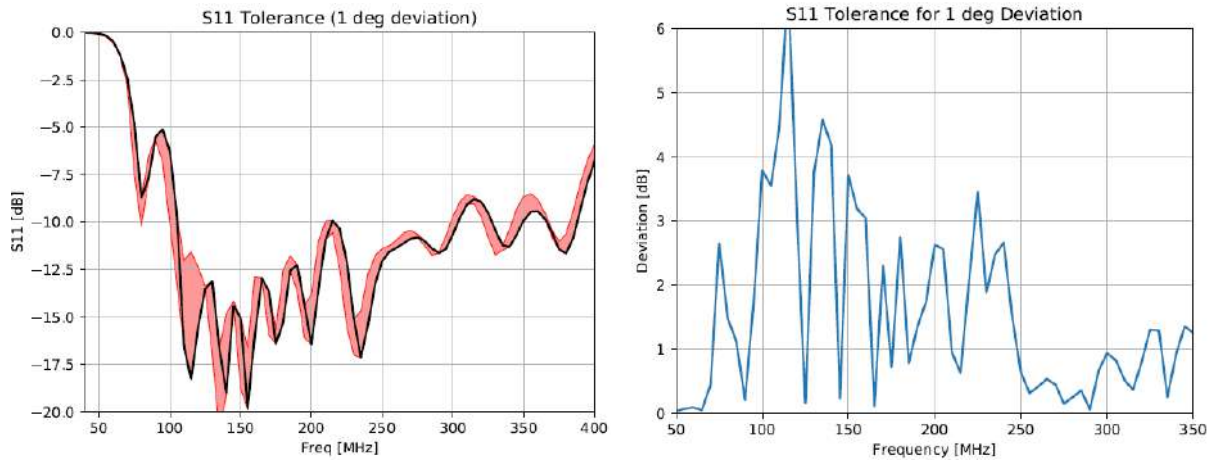


Figure 80: Effect of a +/- 1 degree vertical misalignment on the S11 (left) and the absolute deviation of S11 (right) across frequency.

7.4.3 Feed gap deviation

This is the distance between the booms, so the width of the transmission line. In this section we present the results of a tolerance in the width of the transmission line (gap width) of 1mm. This is a realistic assumption for what we expect to find on the antenna. The results indicate a mild impact on the main antenna parameters (directivity, polarization metric, S11).

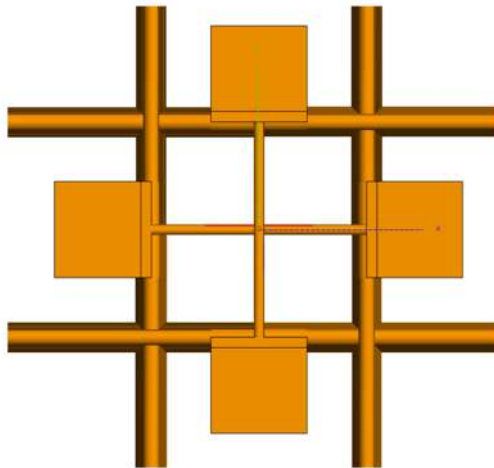


Figure 81: View of the feed gap from above.

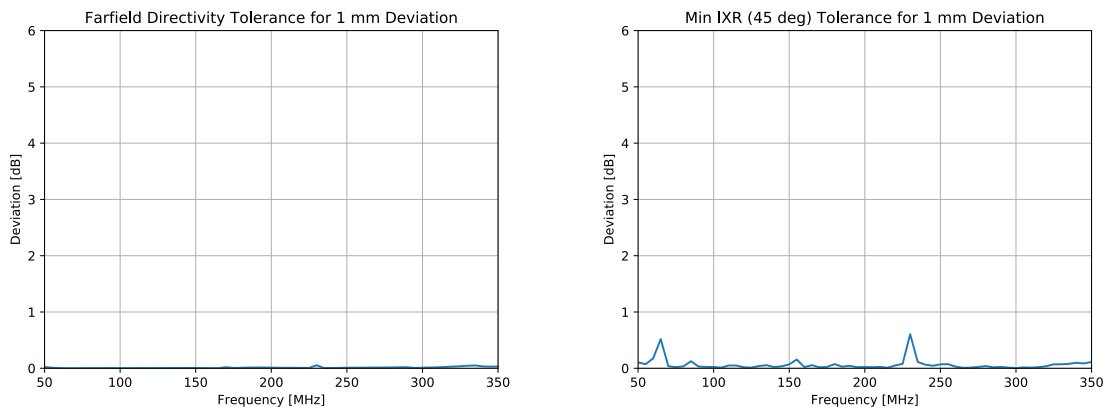


Figure 82: Effect of a 1mm deviation in the feed gap of the antenna (inwards) on the zenith directivity (left) and the minimum IXR within the field of view (right) across frequency. Absolute deviations are shown.

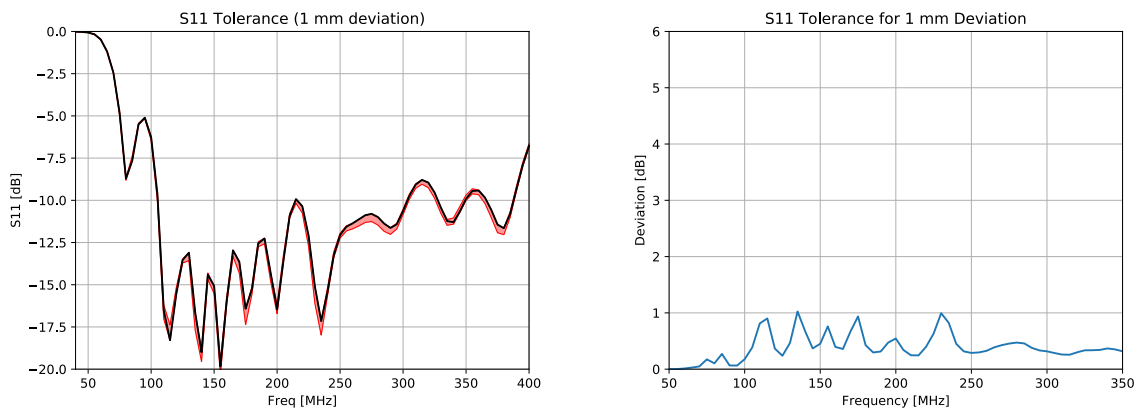


Figure 83: Effect of a 1mm deviation in the feed gap of the antenna (inwards) on the S11 (left) and the absolute deviation of S11 (right) across frequency.

7.4.4 Distance to ground

In this section we present the results of variations in the distance to the ground of +/- 2cm. This is a realistic assumption for what we expect to find on the antenna. The results indicate a moderate impact on the main antenna parameters (directivity, polarization metric, S11) with the largest deviations found in the polarization metric (towards an improvement) and S11.

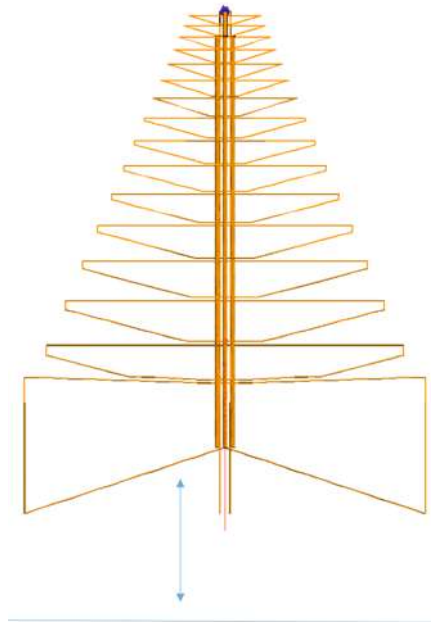


Figure 84: Side view of the distance to ground tolerance.

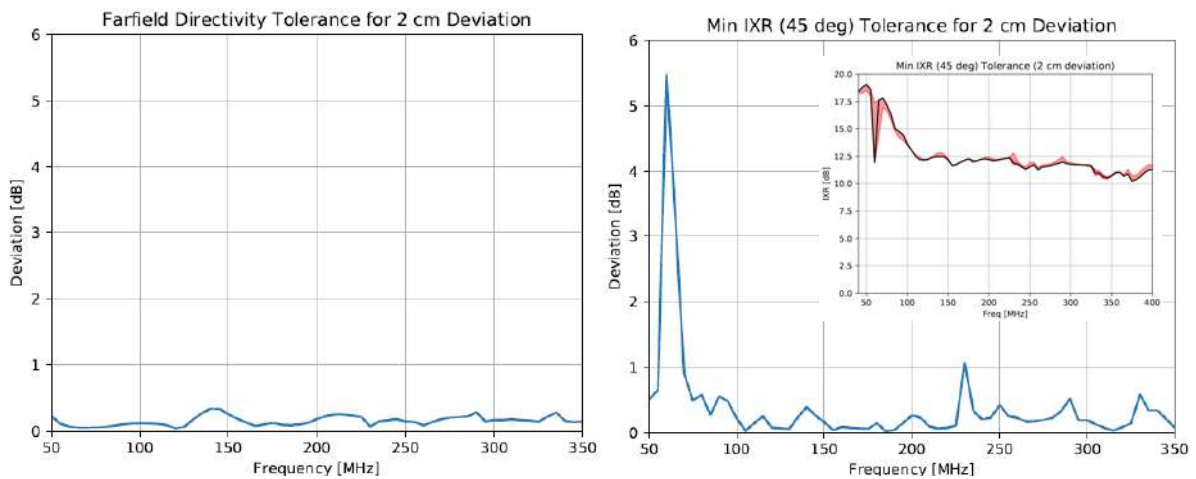


Figure 85: Effect of a +/- 2 cm variation on the distance to ground on the zenith directivity (left) and the minimum IXR within the field of view (right) across frequency. Absolute deviations are shown.

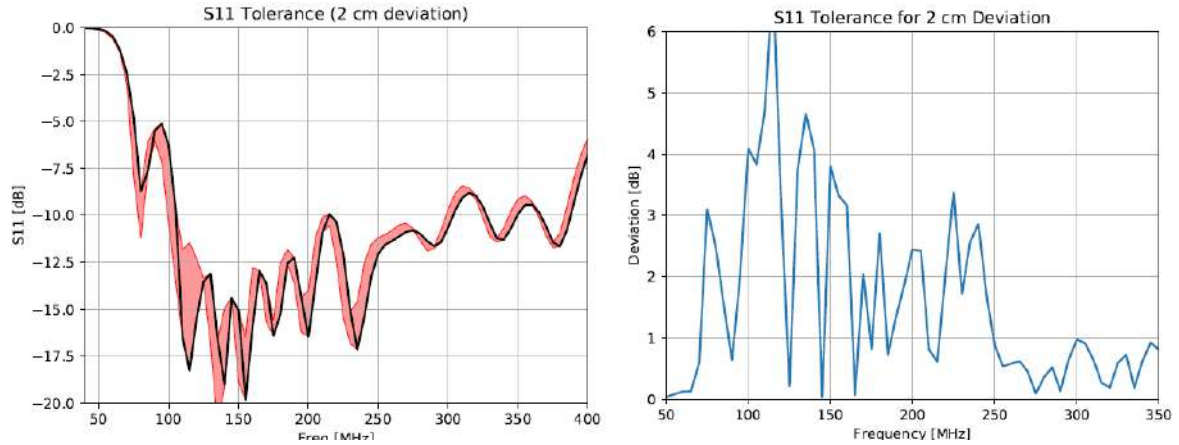


Figure 86: Effect of a +/- 2 cm variation on the distance to ground on the S11 (left) and the absolute deviation of S11 (right) across frequency.

7.4.5 Wire diameter deviation

In this section we present the results of variations in the wire thickness of 0.1 mm. This is a pessimistic assumption for what we expect to find on the antenna. The results indicate a moderate impact on the main antenna parameters (directivity, polarization metric, S11) with the largest deviations found in the polarization metric (towards and improvement) and S11.

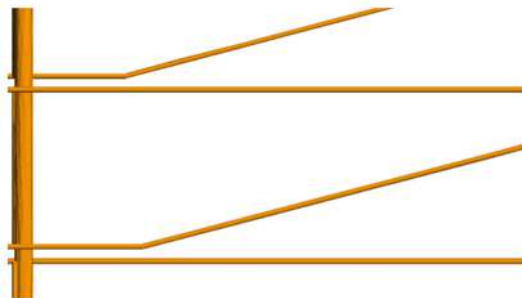


Figure 87: Side view of the one of the wire arms.

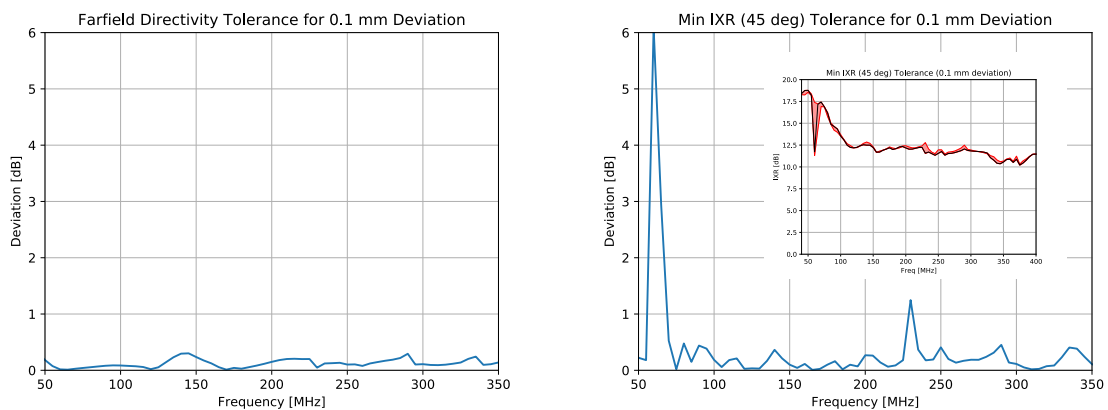


Figure 88: Effect of a 1mm deviation in the wire thickness on the zenith directivity (left) and the minimum IXR within the field of view (right) across frequency. Absolute deviations are shown.

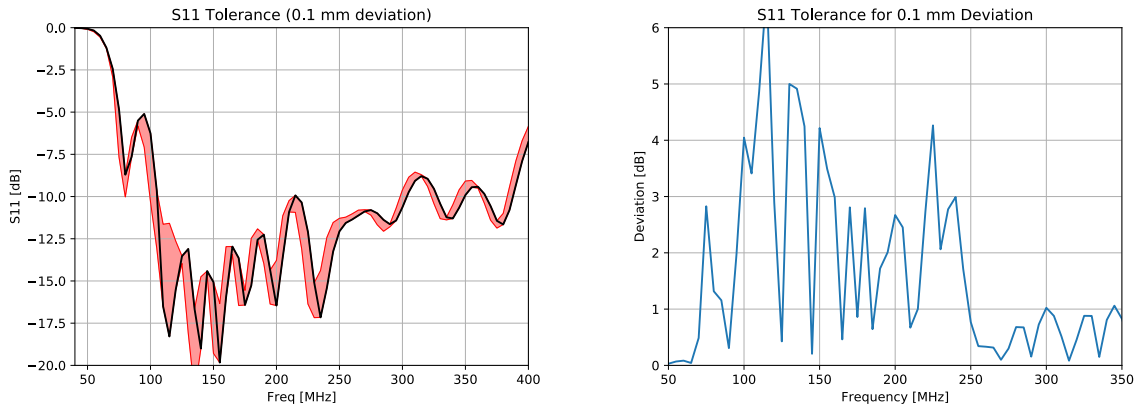


Figure 89: Effect of a 1mm deviation in the wire thickness on the S11 (left) and the absolute deviation of S11 (right) across frequency.

7.4.6 Conclusions

The tolerance analysis in this section represents the most likely variations we will find with the SKALA4 antennas. In the worst case scenarios the modifications of the main metrics for the antenna are only mildly or moderately affected.

It is also worth noting that at low frequencies, where the antenna is less well matched to its LNA due to its short electrical length, these effects tend to be less or positive compared to high frequencies, precisely due to the electrical length of the antenna and its sensitivity to variations. Therefore, any consequences of the mismatch at low frequencies such as the smoothness of the passband would tend to be less sensitive to these tolerances.

7.5 Array tolerances

In this section the main tolerances at the array level are studied and their impact on the station beams is presented.

7.5.1 Rotational misalignment between antennas

In [RD42] a simulated analysis was made for the AAVS1 (SKALA2 antennas) station. In there, the IXR of the station was simulated for different rotational variations between antennas. The conclusion was that small random rotations would not result on variations of the main beam IXR for the station, as also reported on [RD43].

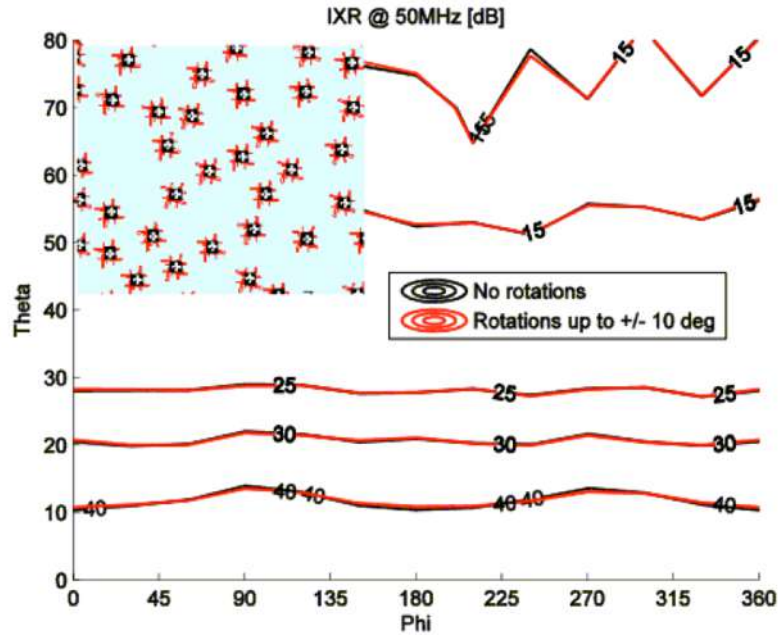


Figure 90: Effect of antenna rotations on the station's IXR.

Furthermore, as shown in [RD37], specific rotations, eg. half of the antennas rotated 90 degrees, could result in improvements of the station's polarization metric due to the better circular symmetry of the resulting station beam.

We have also compared telescope models using OSKAR [RD25] with varying degrees of error in the orientation of individual antenna elements across the entire array, by measuring the impact on the detected flux of a partially polarised and a randomly polarised source at the phase centre. The telescope was at 89 degrees latitude, and the source was at 60 degrees declination. Simulated observations were made for one snapshot, with the source on the meridian (so the zenith angle was 29 degrees).

In all cases, the measured flux from arrays with randomly oriented elements (m) was compared to that measured using a reference array with no element orientation errors (r). The percentage difference in the measured flux values (d) was calculated using:

$$d = 100 \left(\frac{m-r}{r} \right) \quad (3)$$

Results were obtained from differences of images in both uncalibrated Stokes I for a randomly polarised source and a source polarised with 50% Stokes Q, and images in uncalibrated Stokes Q for a randomly polarised source and a source polarised with 50% Stokes Q (see figures and tables below).

All stations had different random layouts. Tests were done with the SKALA2 element pattern at 100, 220, 350, 500 and 600 MHz, and also (for comparison) with a frequency-independent half-wavelength dipole. Element rotation angle deviations across the entire array were selected from random Gaussian distributions with a standard deviation of 2.5, 5.0 and 10.0 degrees. It should be noted that all tabulated results are for one realisation of the array: All random distributions were obtained using sequences with the same starting seed of 0.

Gaussian error [deg]	SKALA 100 MHz	SKALA 220 MHz	SKALA 350 MHz	SKALA 500 MHz	SKALA 600 MHz	Half-wavelength dipole
2.5	-0.188	-0.186	-0.180	-0.224	-0.183	-0.193
5.0	-0.751	-0.744	-0.721	-0.880	-0.730	-0.768
10.0	-2.974	-2.951	-2.880	-3.355	-2.899	-3.033

Table 14: Percentage difference in measured Stokes I source flux for a randomly polarised source at the phase centre.

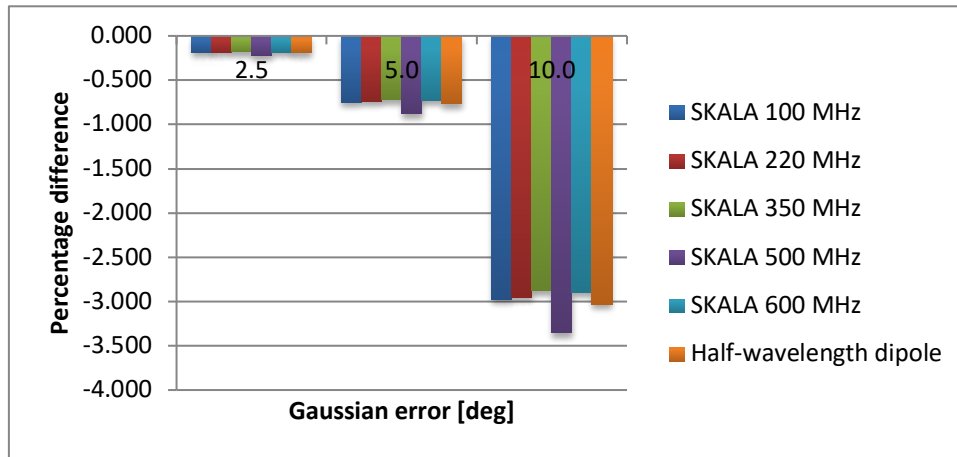


Figure 91: Percentage difference in measured Stokes I source flux for a randomly polarised source at the phase centre.

Gaussian error [deg]	SKALA 100 MHz	SKALA 220 MHz	SKALA 350 MHz	SKALA 500 MHz	SKALA 600 MHz	Half-wavelength dipole
2.5	-0.185	-0.190	-0.177	-0.233	-0.194	-0.182
5.0	-0.740	-0.760	-0.714	-0.913	-0.778	-0.724
10.0	-2.941	-3.017	-2.867	-3.469	-3.097	-2.870

Table 15: Percentage difference in measured Stokes I source flux for a source polarised with 50% Stokes Q at the phase centre.

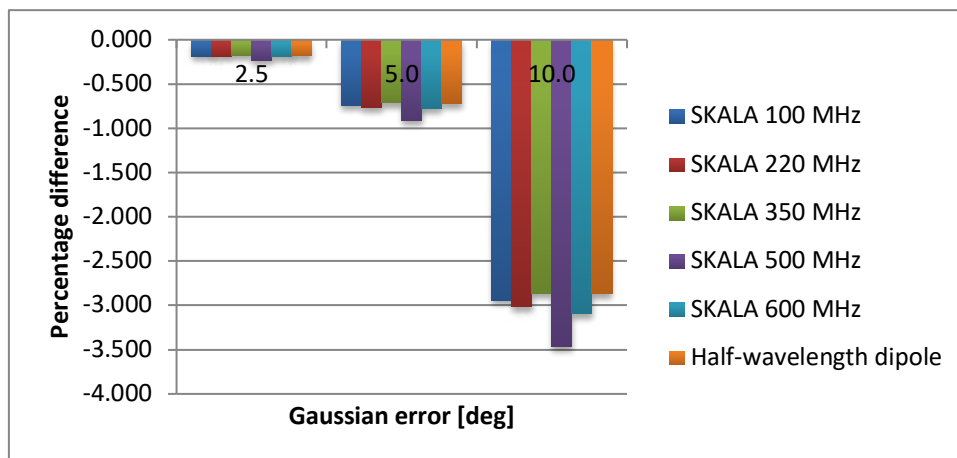


Figure 92: Percentage difference in measured Stokes I source flux for a source polarised with 50% Stokes Q at the phase centre.

Gaussian error [deg]	SKALA 100 MHz	SKALA 220 MHz	SKALA 350 MHz	SKALA 500 MHz	SKALA 600 MHz	Half-wavelength dipole
2.5	-0.248	-0.156	-0.197	-0.083	-0.088	-0.300
5.0	-0.956	-0.595	-0.767	-0.322	-0.334	-1.190
10.0	-3.573	-2.277	-2.940	-1.344	-1.260	-4.610

Table 16: Percentage difference in measured Stokes Q source flux for a randomly polarised source at the phase centre.

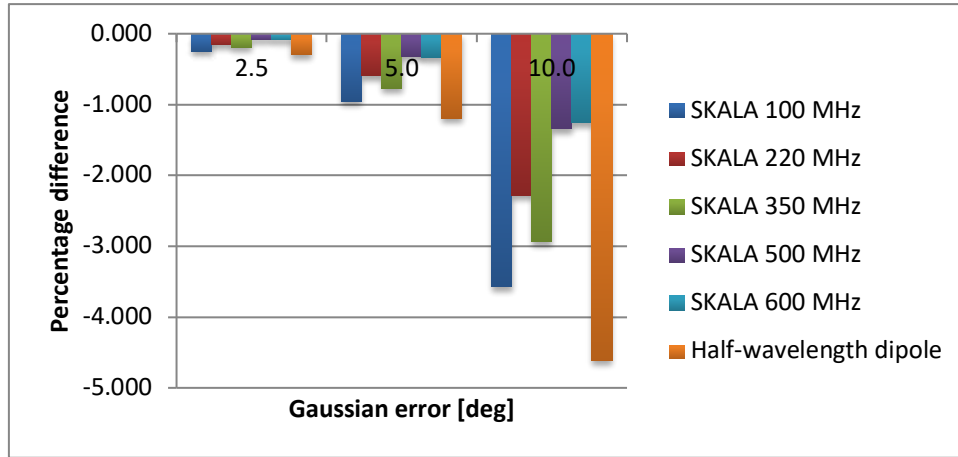


Figure 93: Percentage difference in measured Stokes Q source flux for a randomly polarised source at the phase centre.

Gaussian error [deg]	SKALA 100 MHz	SKALA 220 MHz	SKALA 350 MHz	SKALA 500 MHz	SKALA 600 MHz	Half-wavelength dipole
2.5	-0.160	-0.202	-0.161	-0.298	-0.242	-0.128
5.0	-0.668	-0.822	-0.670	-1.153	-0.979	-0.515
10.0	-2.749	-3.300	-2.789	-4.306	-3.940	-2.089

Table 17: Percentage difference in measured Stokes Q source flux for a source polarised with 50% Stokes Q at the phase centre.

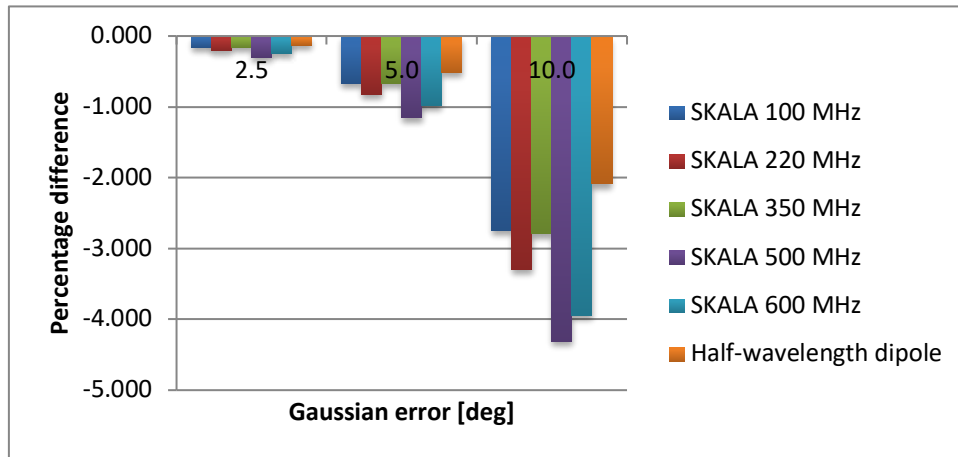
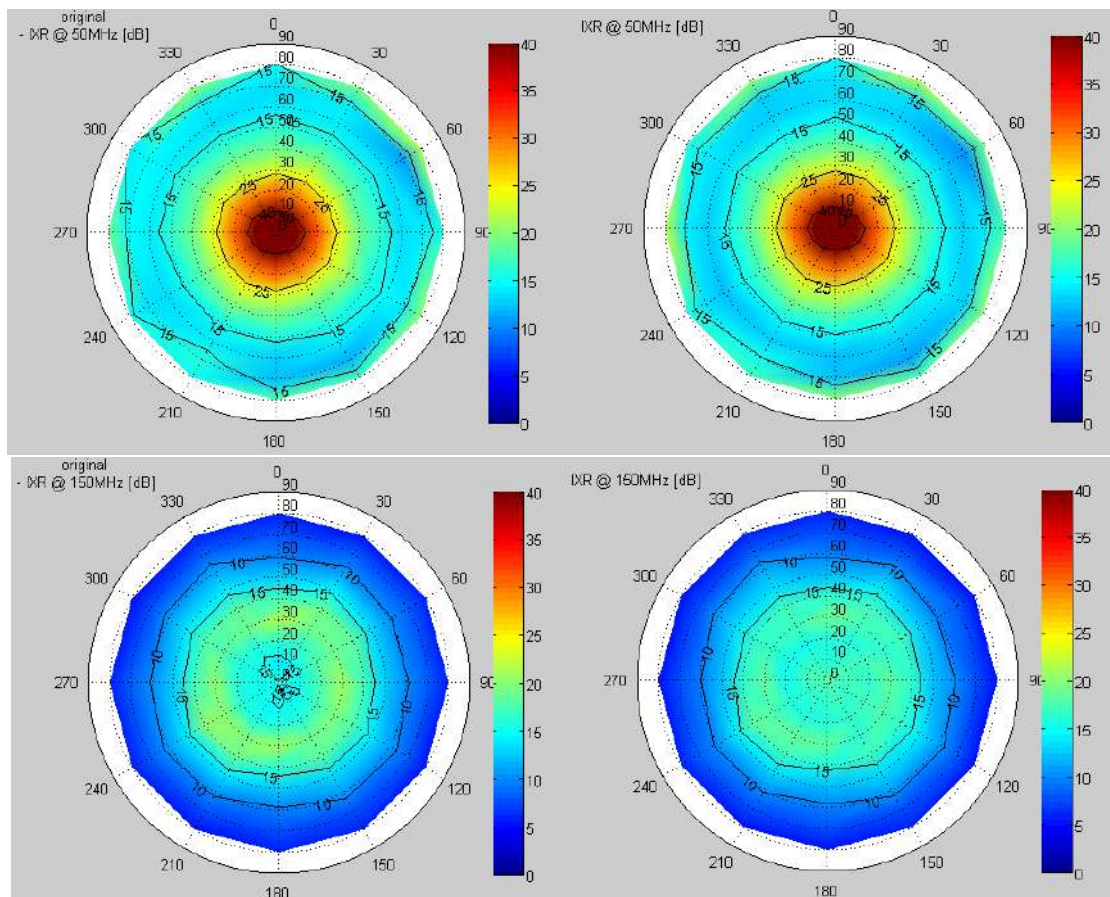


Figure 94: Percentage difference in measured Stokes Q source flux for a source polarised with 50% Stokes Q at the phase centre.

7.5.2 Rotational misalignment between antennas

In this section we present results for AAVS1 (SKALA2 antennas), showing the expected impact on IXR for variations in the vertical position of the antennas across the array of up to 10 cm. As it can be seen in **Figure 95** the effects are very small.



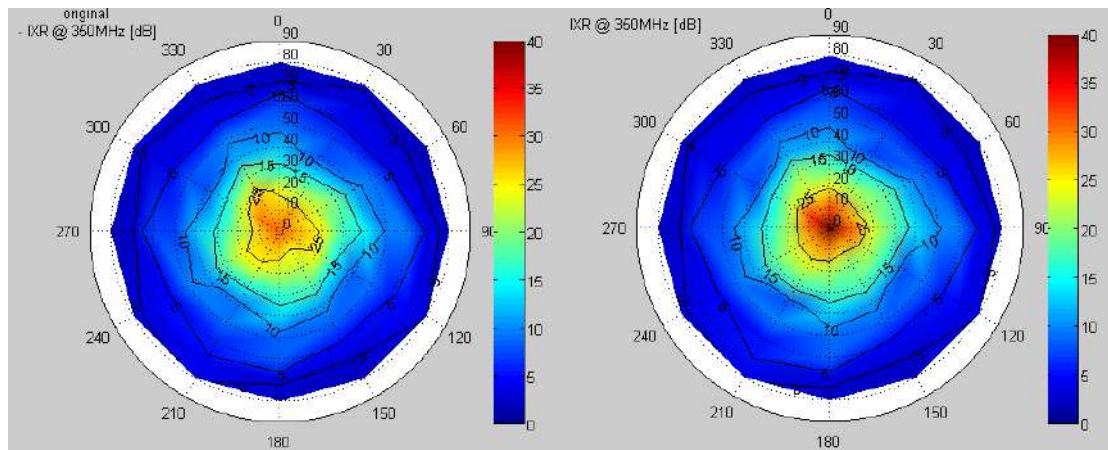
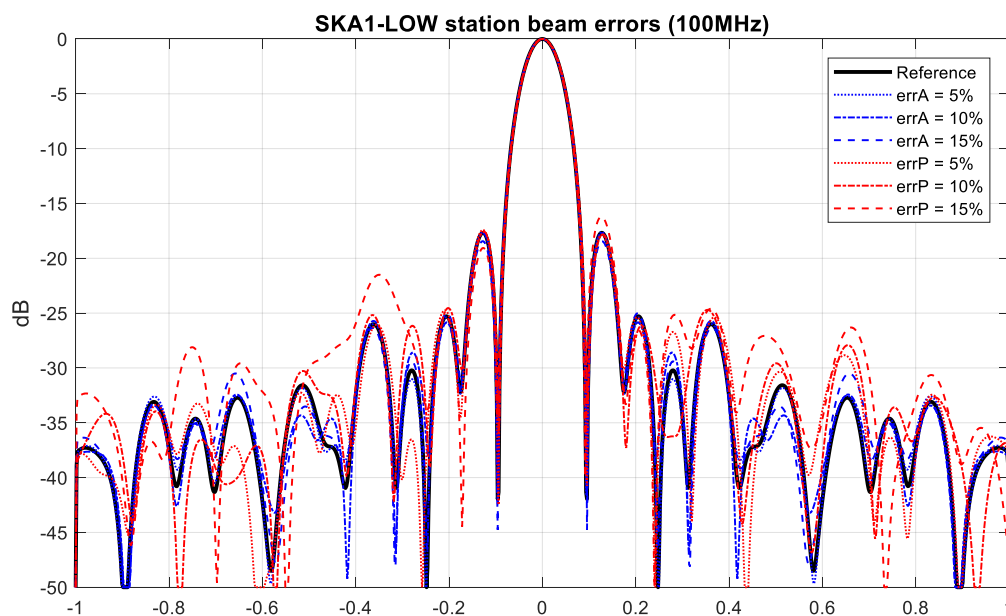


Figure 95: Effect of antenna vertical positions on the station's IXR at 3 different frequencies. All antennas same position (left column) and random variations up to 10 cm (right column).

7.5.3 Calibration uncertainties in the amplitude and phase of the weights

The figures below show the effect of random unaccounted amplitude and phase errors applied to the complex weights at beam forming in the station beam. This can be read at the impact of calibration errors.

These results show a more dominant effect of the phase errors with a special impact on the inner side lobes. This is expected since the inner side lobes are the ones that behave like in a regular array. The main beam width is only slightly modified. Its position is unmodified. These effects are similar in level when the array is scanned since the array factor is displaced in the angular domain but the relation between main beam and side lobes is retained.



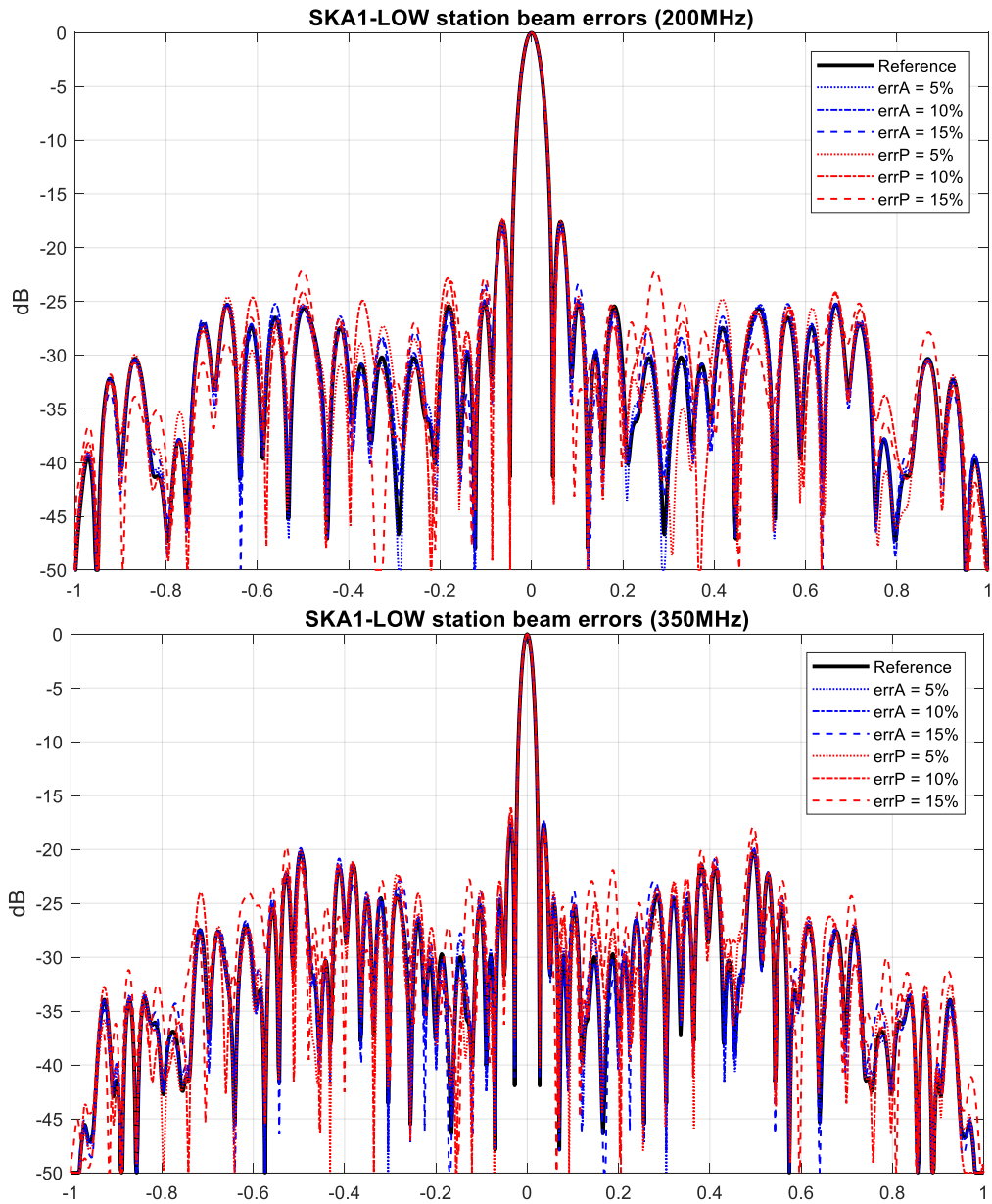
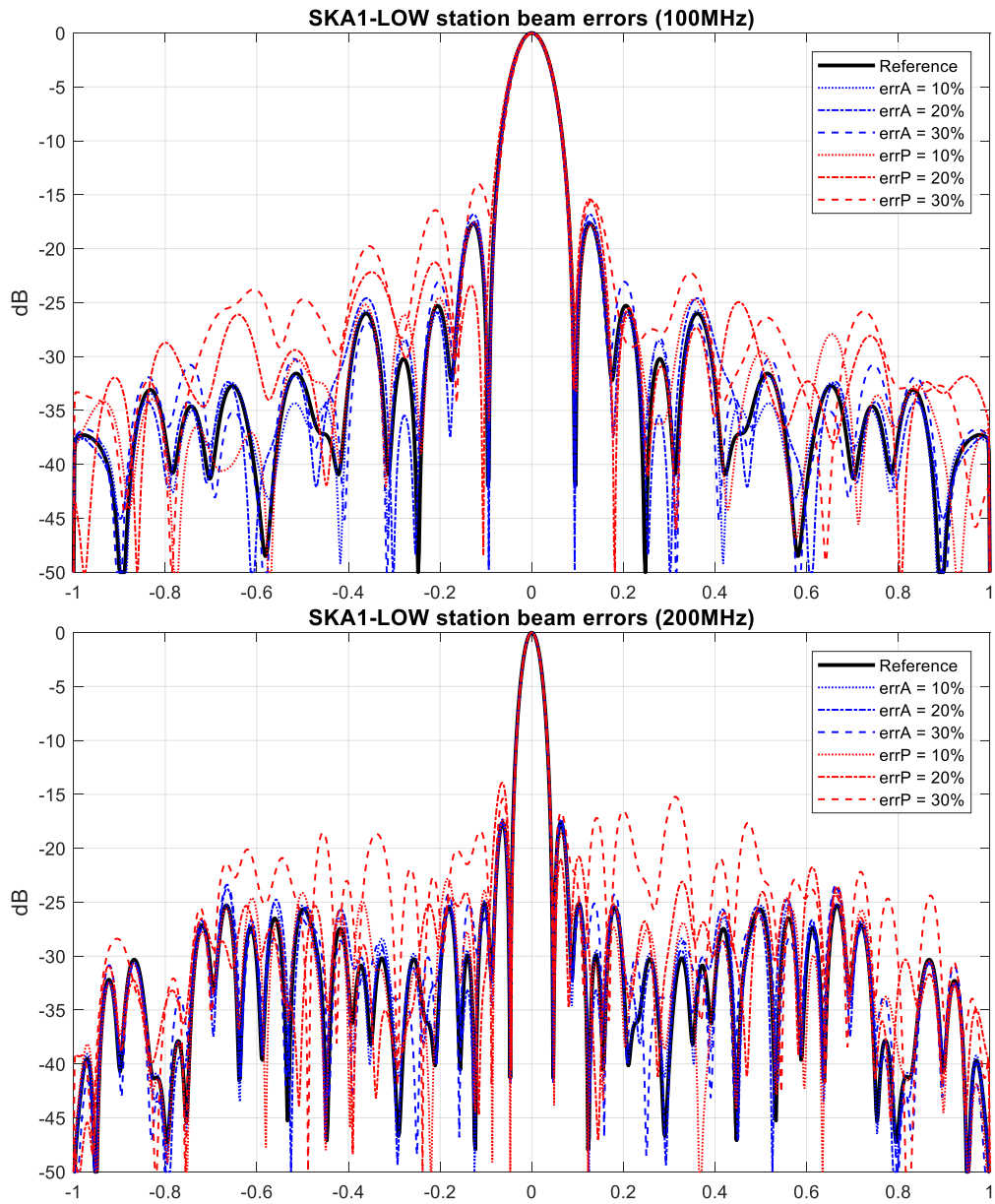


Figure 96: Effects of unaccounted phase and amplitude errors in the array beam (normalized directivity). Errors: 5%, 10% and 15% at 3 different frequencies: 100 (top), 200 and 350 (bottom) MHz.



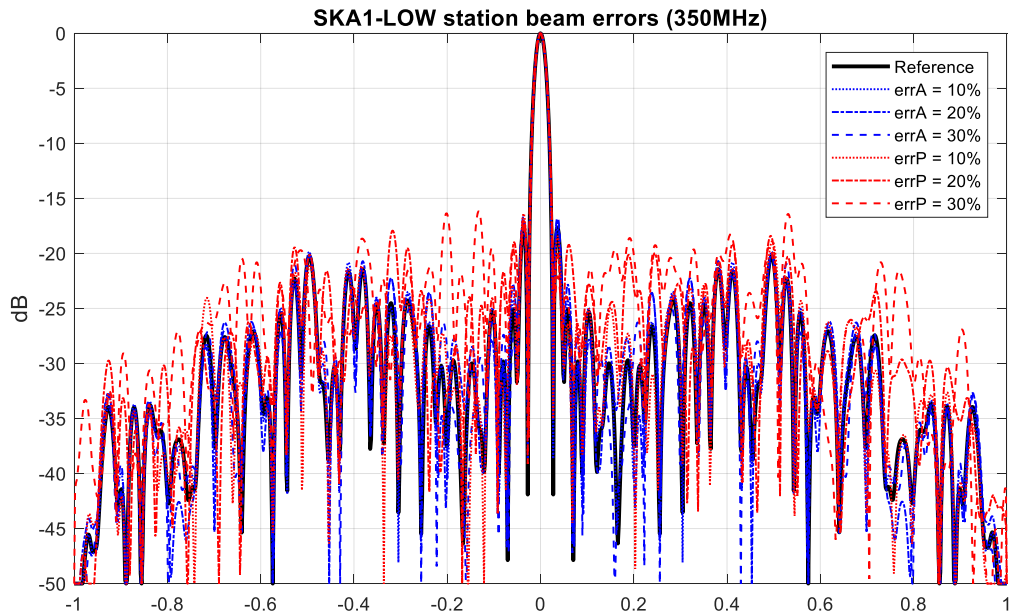


Figure 97: Effects of unaccounted phase and amplitude errors in the array beam (normalized directivity). Errors: 10%, 20% and 30% at 3 different frequencies: 100 (top), 200 and 350 (bottom) MHz.

An estimation of the statistical impact of calibration errors in the main peak gain and side lobe level can be found in **Figure 100** and **Figure 101**. This is based on 50 simulations such as the ones presented in **Figure 98** and **Figure 99**.

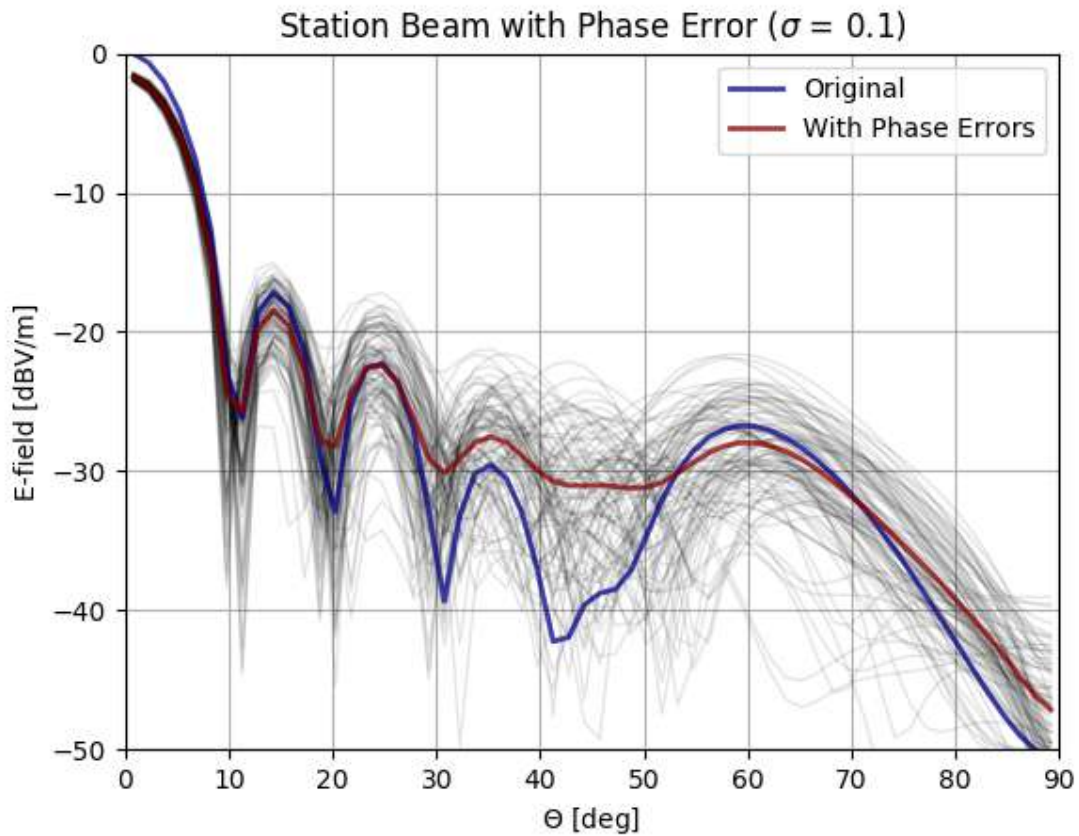


Figure 98: Example of 50 simulated E-field station beams for unaccounted phase errors equivalent to 0.1 STDEV. Frequency = 50 MHz.

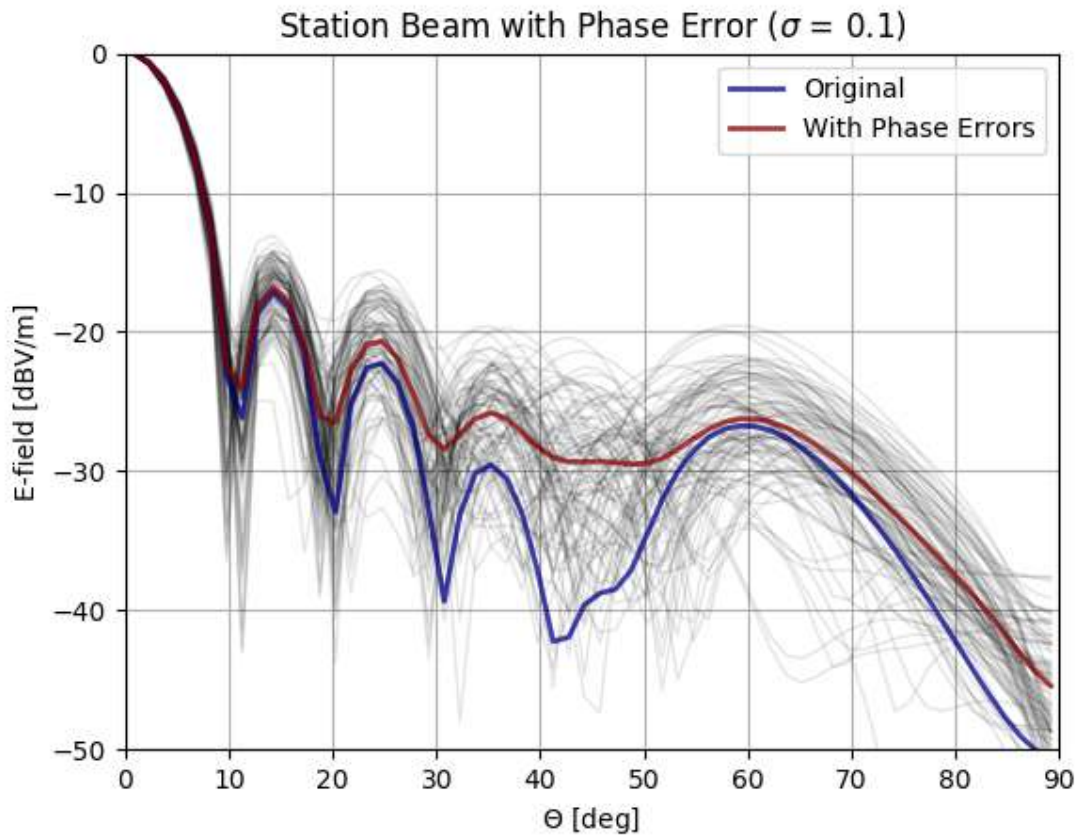


Figure 99: Example of 50 simulated E-field station beams (normalized) for unaccounted phase errors equivalent to 0.1 STDEV. Frequency = 50 MHz.

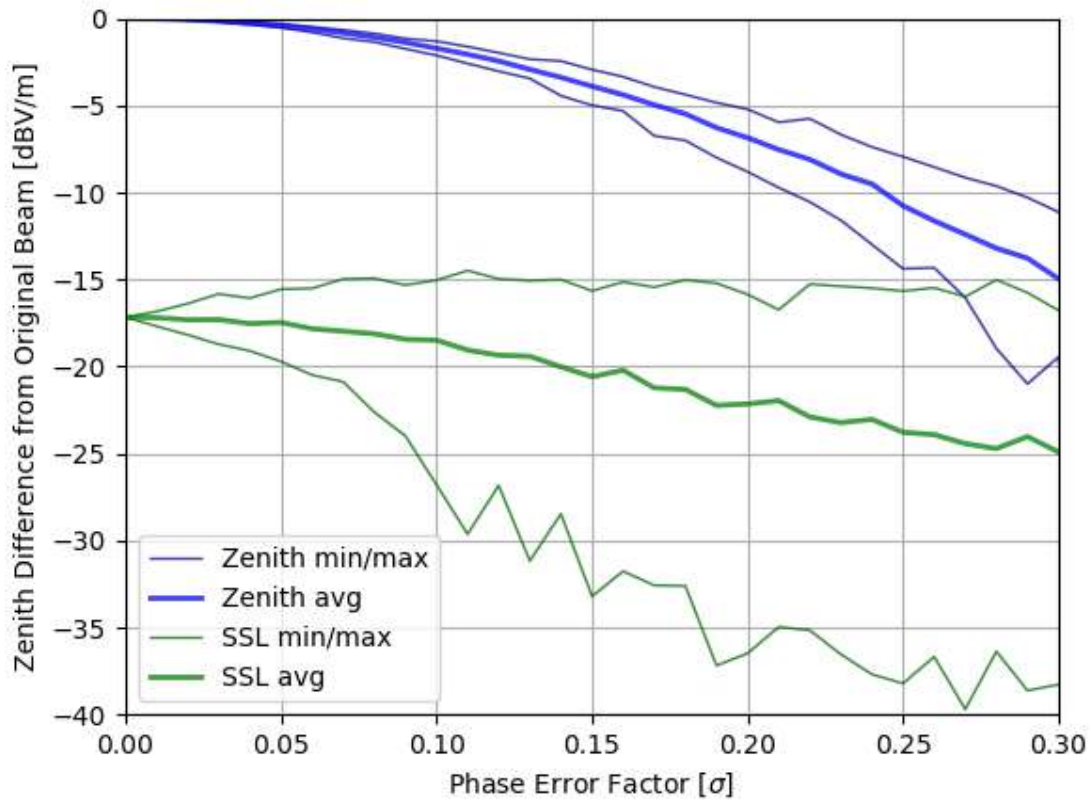


Figure 100: Statistical impact of unaccounted phase errors (as a function of the standard deviation of the error) in the main beam and maximum SLL. Field beams at frequency = 50 MHz.

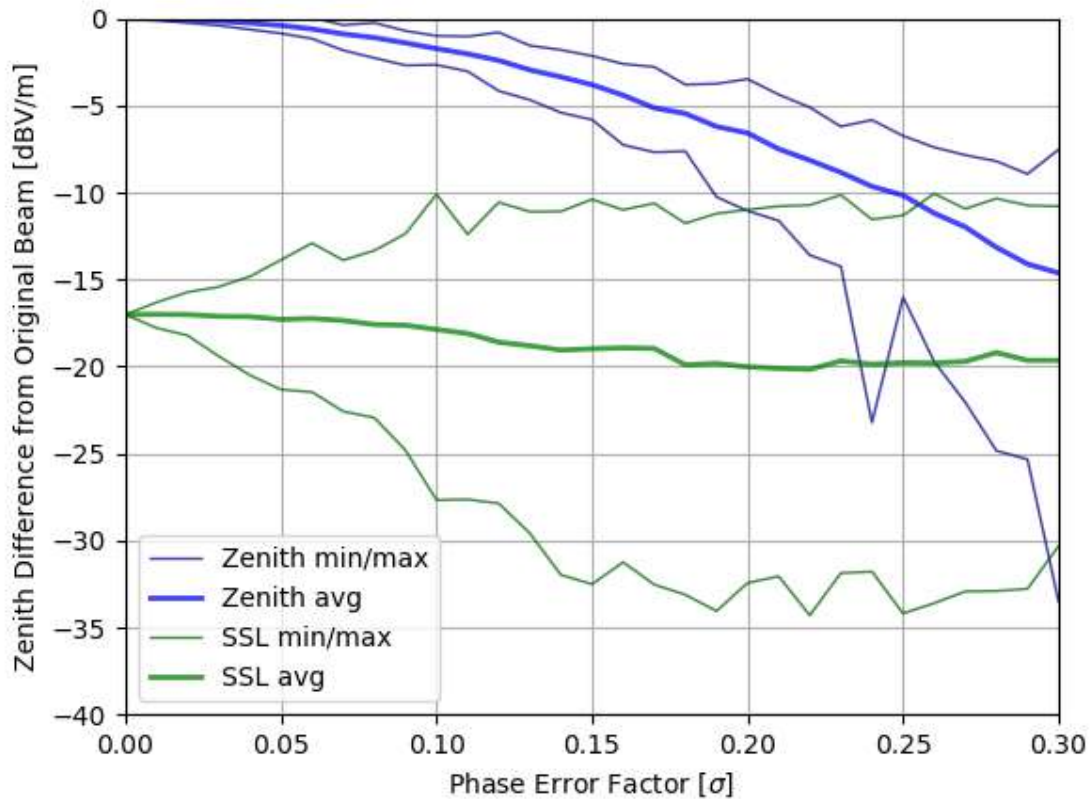


Figure 101: Statistical impact of unaccounted phase errors (as a function of the standard deviation of the error) in the main beam and maximum SLL. Field beams at frequency = 350 MHz.

Using this information one can calculate the expected impact on the array's sensitivity of position errors (based on the phase errors calculations). In here a position error is defined as the lack of knowledge of the exact position of the antenna. See Table 6 for a summary of these.

frequency /MHz	Position error	Effect on sensitivity
50	5% (30 cm)	-1.1%
	10% (60 cm)	-4.9%
	15% (90 cm)	-9.4%
100	5% (15 cm)	-1.1%
	10% (30 cm)	-5.6%
	15% (45 cm)	-9.8%
200	5% (7.5 cm)	-1.1%
	10% (15 cm)	-4.5%
	15% (22.5 cm)	-10.8%
300	5% (5 cm)	-1.1%
	10% (10 cm)	-4.8%
	15% (15 cm)	-8.5%
350	5% (4.28 cm)	-1.1%
	10% (8.57 cm)	-4.9%
	15% (12.84 cm)	-9.4%

Table 18: Approximate effect of unknown random position/phase errors on the array sensitivity.

7.6 Ground plane and APIU/station box effects

In the following we present the effect of the size and shape of the ground plane on the array beams as well as the effect of the APIU and station box. The soil used in the electromagnetic simulations is characteristic Western Australian soil [RD44] and the ground plane is a solid ground plane.

The goal of the first set of simulations was to understand the effect of the finiteness and size of the ground mesh. We explore the effects of extending the radius of a circular ground plane as well as the use of the proposed “digital edges” ground plane [RD3]. We compare these with an infinite ground plane for a small array (64 elements) in **Figure 102** since this is a very expensive simulation to run requiring an extremely large amount of RAM (the server where this simulation run has 384 GB). Given the results we don’t expect differences in our conclusion for a 256-element station. It seems clear that minor effects can be observed at low frequencies in the far out side lobes but overall we don’t expect a significant effect on the beams.

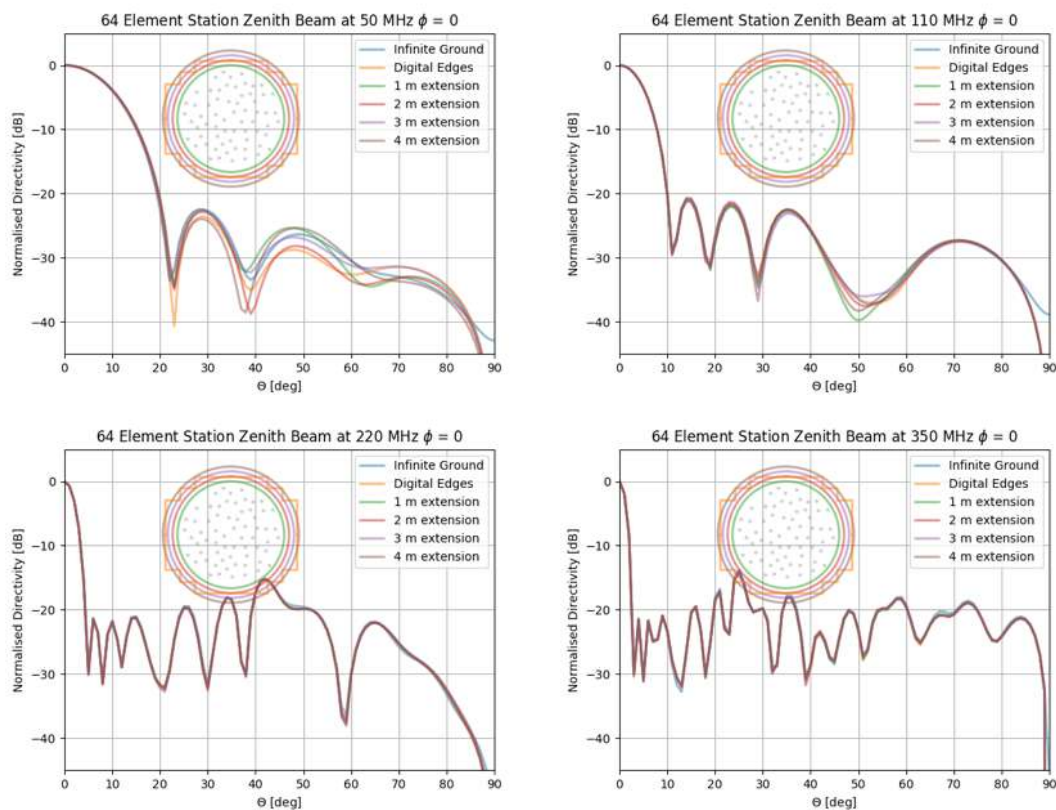


Figure 102: 64-element array directivity at 4 different frequencies (50, 110, 220 and 350 MHz) for different ground plane configurations. The added extensions to the circular ground planes are radial (eg. 1 m extension means 1 m radially).

The next set of simulations were used to explore the effect of both the use of a “digital edge” ground plane in comparison with a circular one and an infinite ground plane for a 256-element station, as well as the effect of the APIU and station boxes (see [RD3] for information on their size and Figure 1 for a view of their location in the array) in the beams. It seems clear that again only minor and predictable effects can be seen on the edge of the beam and for low frequencies.

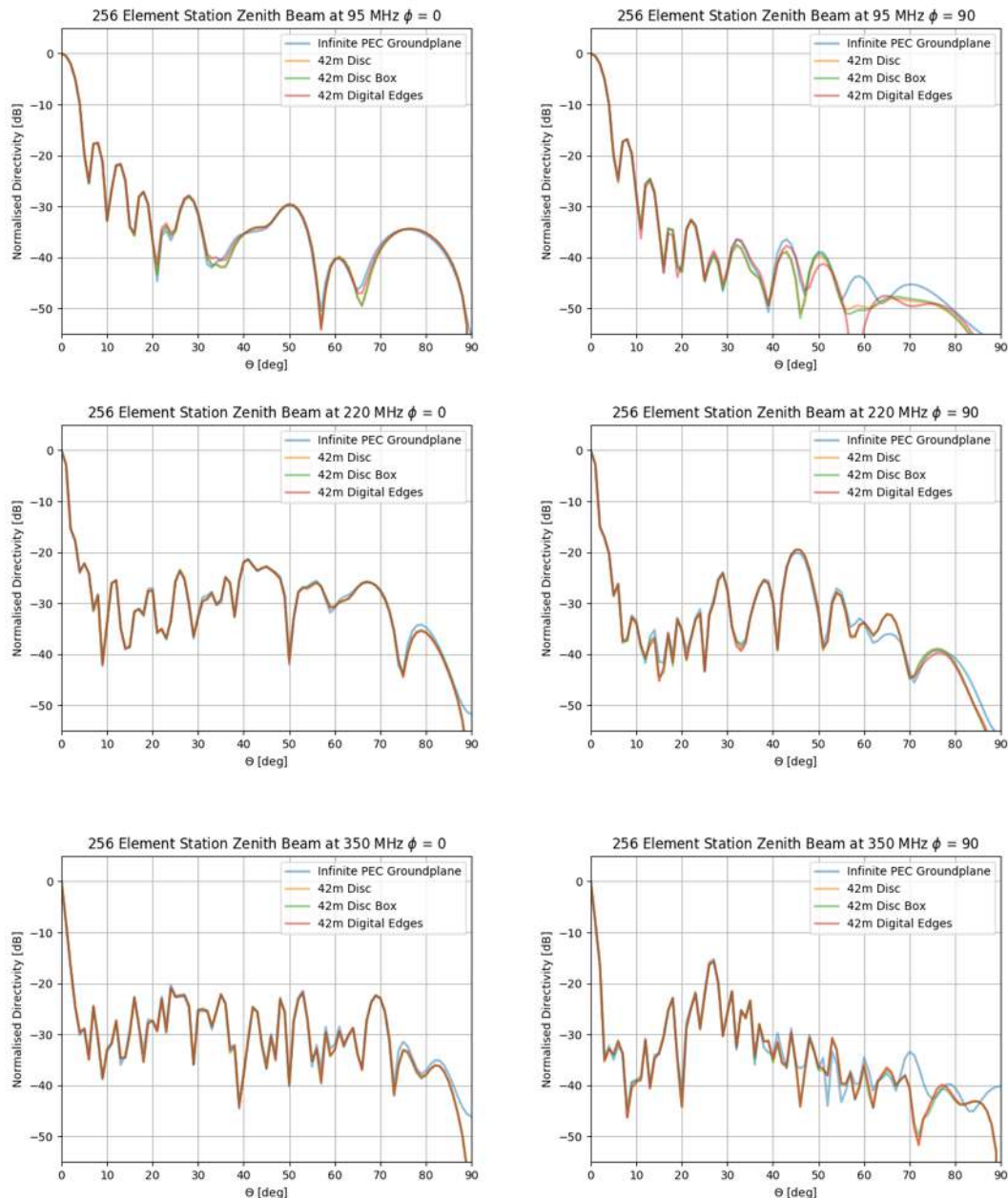


Figure 103: 256-element array directivity at 3 different frequencies (95, 220 and 350 MHz) for different ground plane configurations and also including the station boxes.

7.7 Impact of antenna and TPM failures

In this section, the expected loss for a given number of antenna failures is presented.

7.7.1 Failing antennas and Tile Processing Module

The signals of 16 antennas (32 signal paths) are combined in one Tile Processing Module (TPM). A failing TPM will result in 16 failing antennas. In the LFAA design 16 antennas are placed near each other and combined in one TPM module. An impression from an availability point of view gives the idea that the impact of 16 random missing antennas is lower. Simulations are executed to have an

idea about the impact of failing antennas and tile processing modules. The following situations of a failing TPM are analysed:

- Tile/group of 16 antennas belonging to a TPM
- Cumulative TPM fails
- Random failing antennas

7.7.2 Tile/group of 16 antennas belonging to a TPM

Based on the current assignment of antennas to TPMs in AAVS1 (following a pizza-slice type of assignment due to logistic considerations), simulations have been run to assess the impact on the station beams of TPM fails. Obviously this assignment (see **Figure 104** and Figure 105) could be done in a different manner and the expected effects may differ from the ones shown in here.

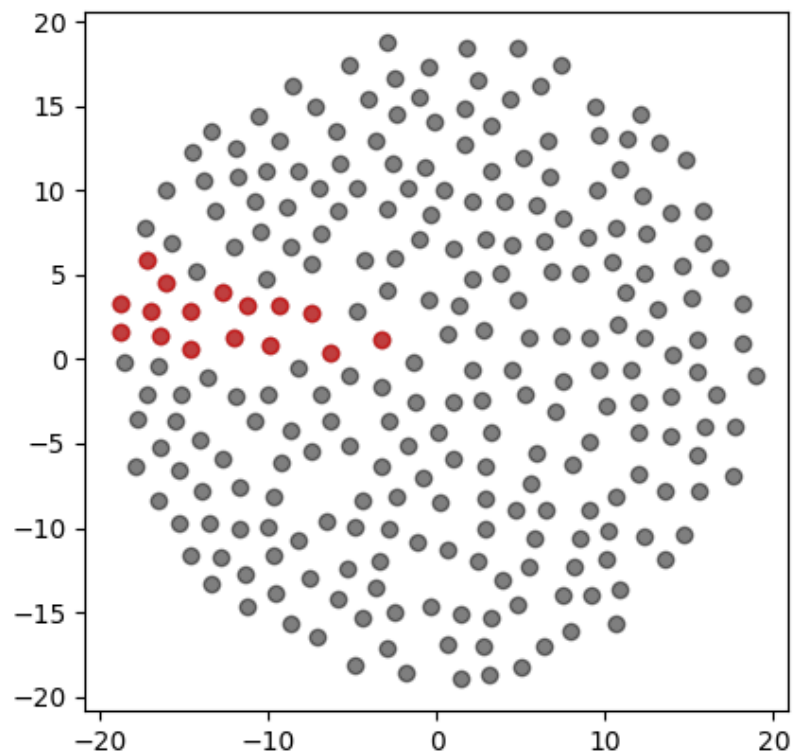


Figure 104: Station antenna coordinates (in m). Antennas belonging to TPM 15 are shown in red.

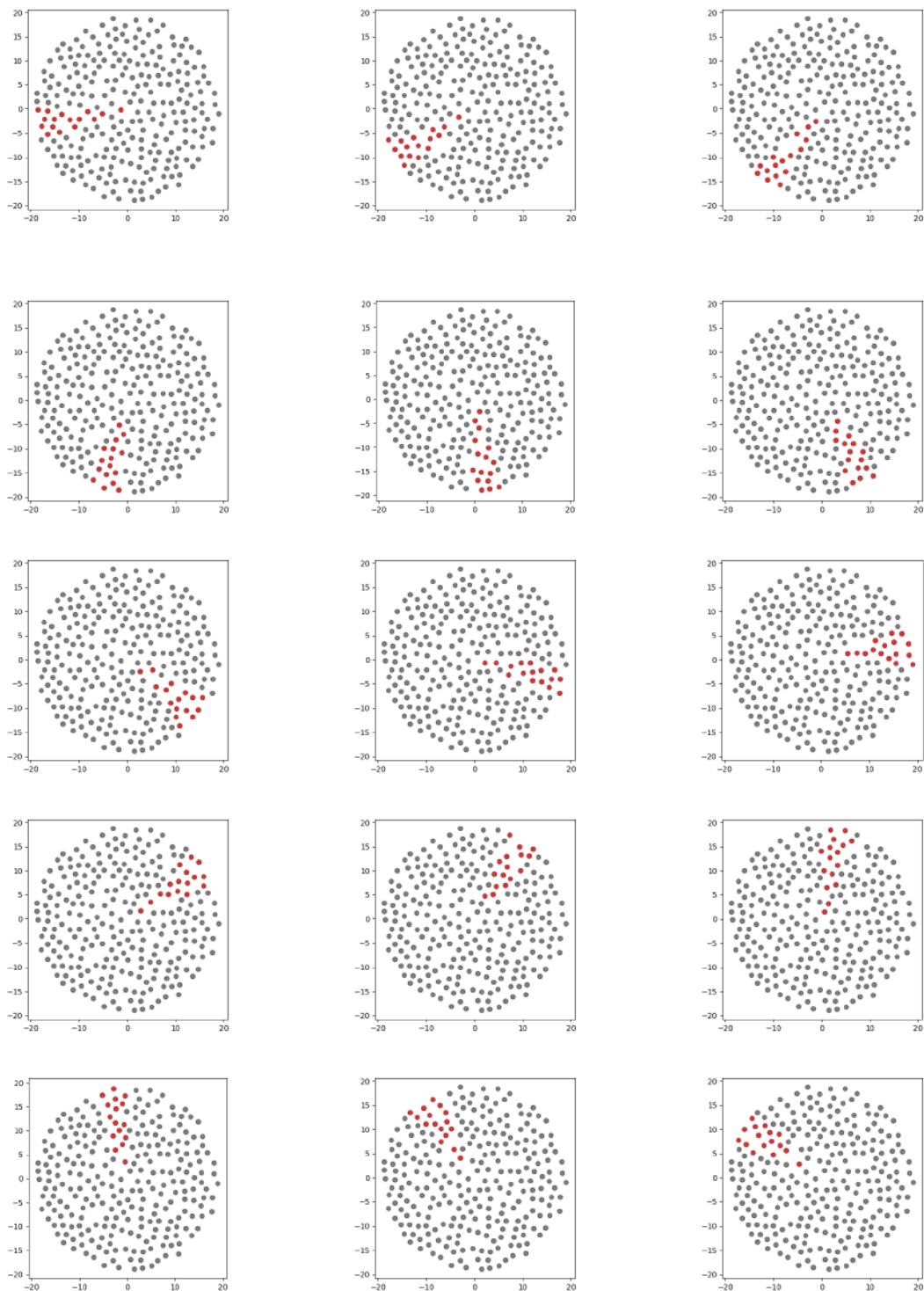


Figure 105: Station antenna coordinates (in m). Antennas belonging to TPMs 0-14 (top left to bottom right) are shown in red.

Figure 106 shows examples of the station's E-field beam at 4 different frequencies across the band for 2 different TPMs failing (no signal contribution to the beamformer). The following figure then shows the effect of the different TPMs failing (individually) on the station beam side lobes (no detail on the main beam shown) at 4 different frequencies. This shows a very small impact. Specific

simulations (eg. for off zenith scans) may be needed to assess the potential impact in a given mode of observation.

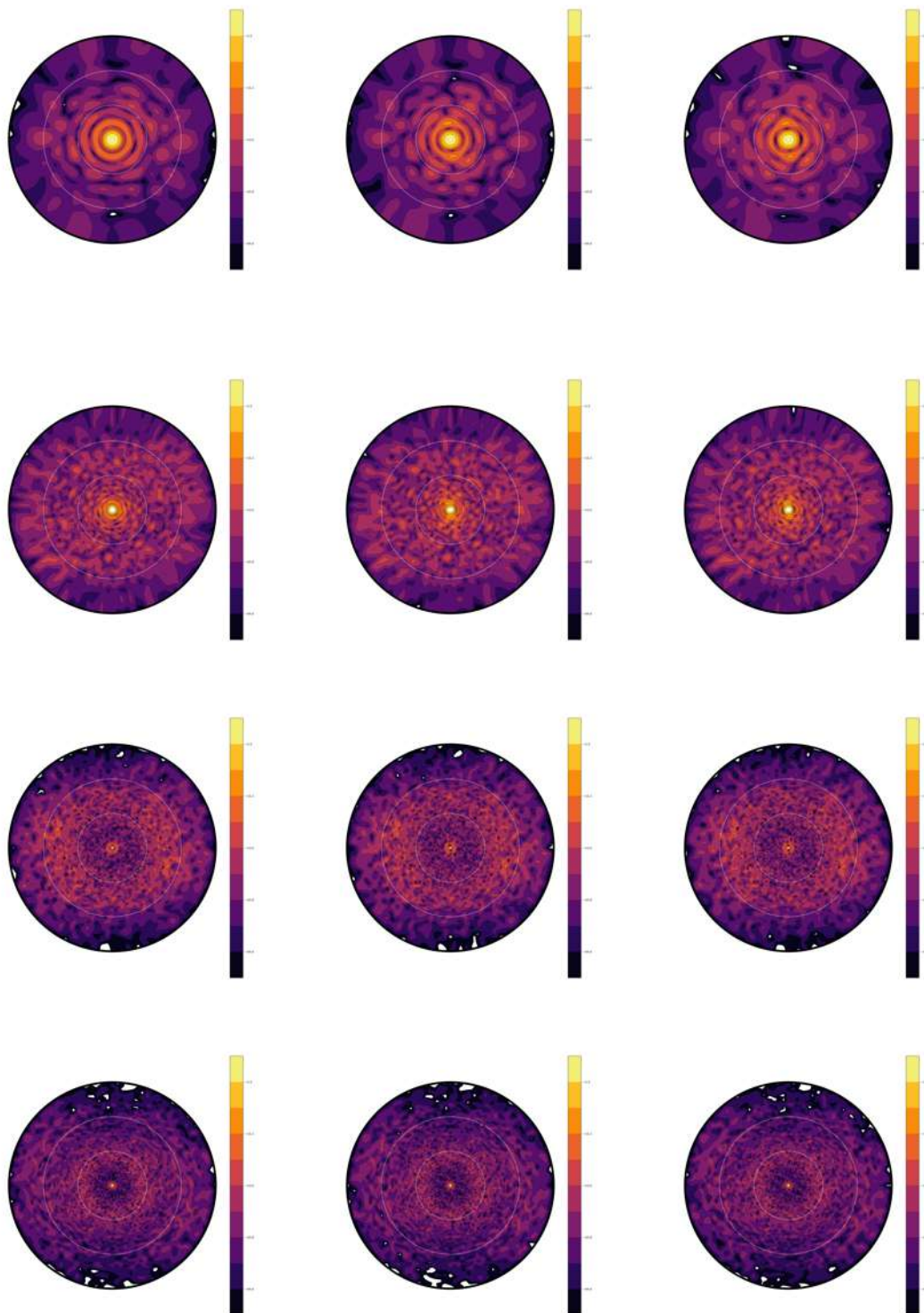


Figure 106: Station E-field beam (in dBV/m) at 50 MHz (top row), 110 MHz, 220 MHz and 350 MHz (bottom row) for no failing TPMs (left column), failing TPM 0 (central column) and failing TPM 8 (right column).

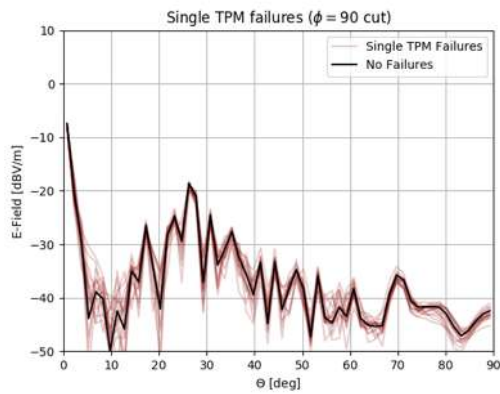
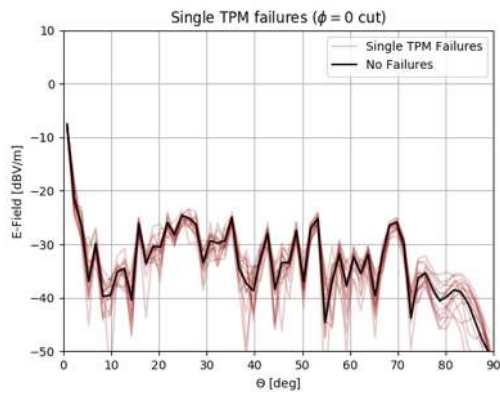
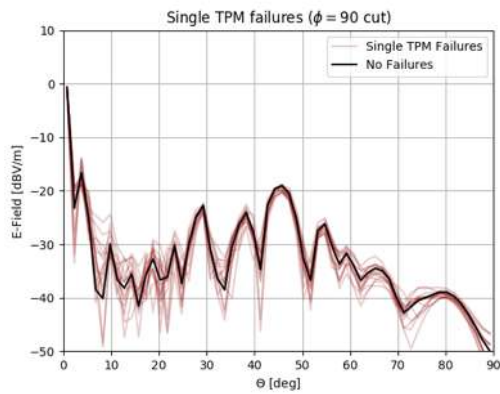
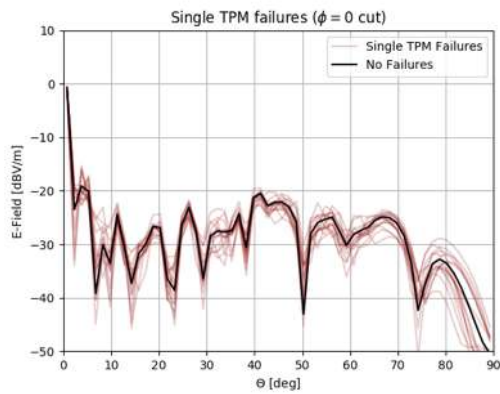
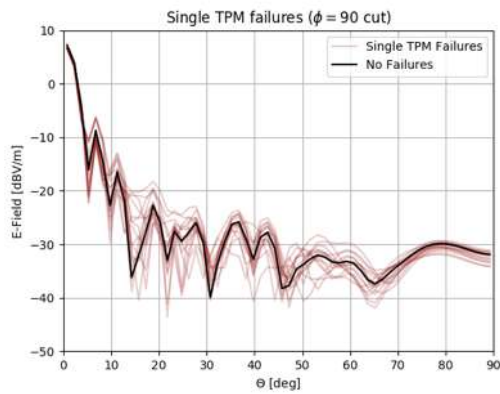
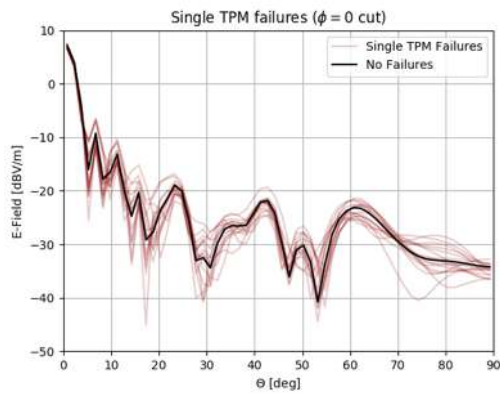
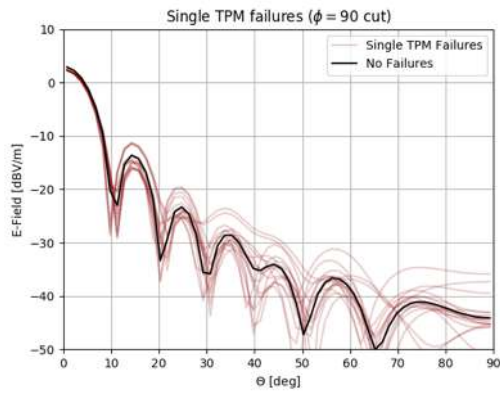
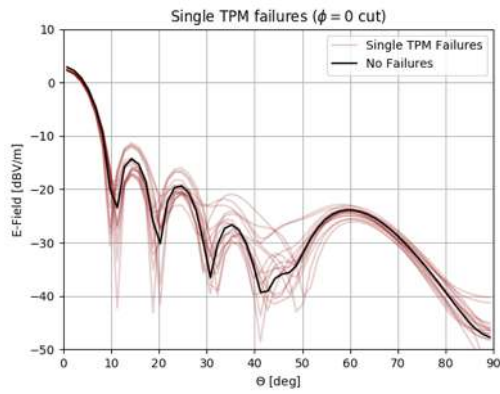
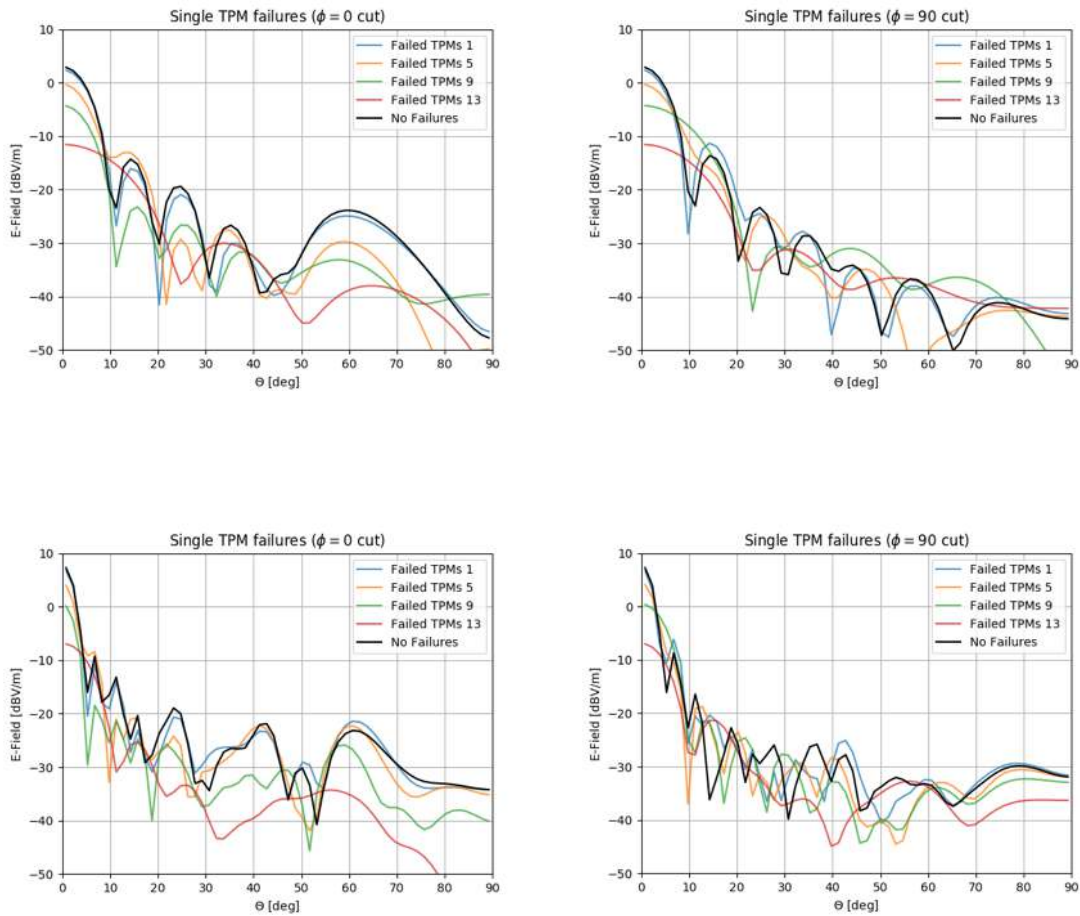


Figure 107: Station E-field beam cuts (in dBV/m) at 50 MHz (top row), 110 MHz, 220 MHz and 350 MHz (bottom row) for a $\phi = 0$ deg. cut and a $\phi = 90$ deg. Cut and the different TPMs failing individually. Zoom of the side lobe region.

7.7.3 Cumulative TPM fails

In the following we present the cumulative effect of TPM failures. This is multiple TPMs failing at the same time. While the beams would still be predictable it is clear that the beam degradation can be quite sever for a cumulative loss of TPMs as one would expect.



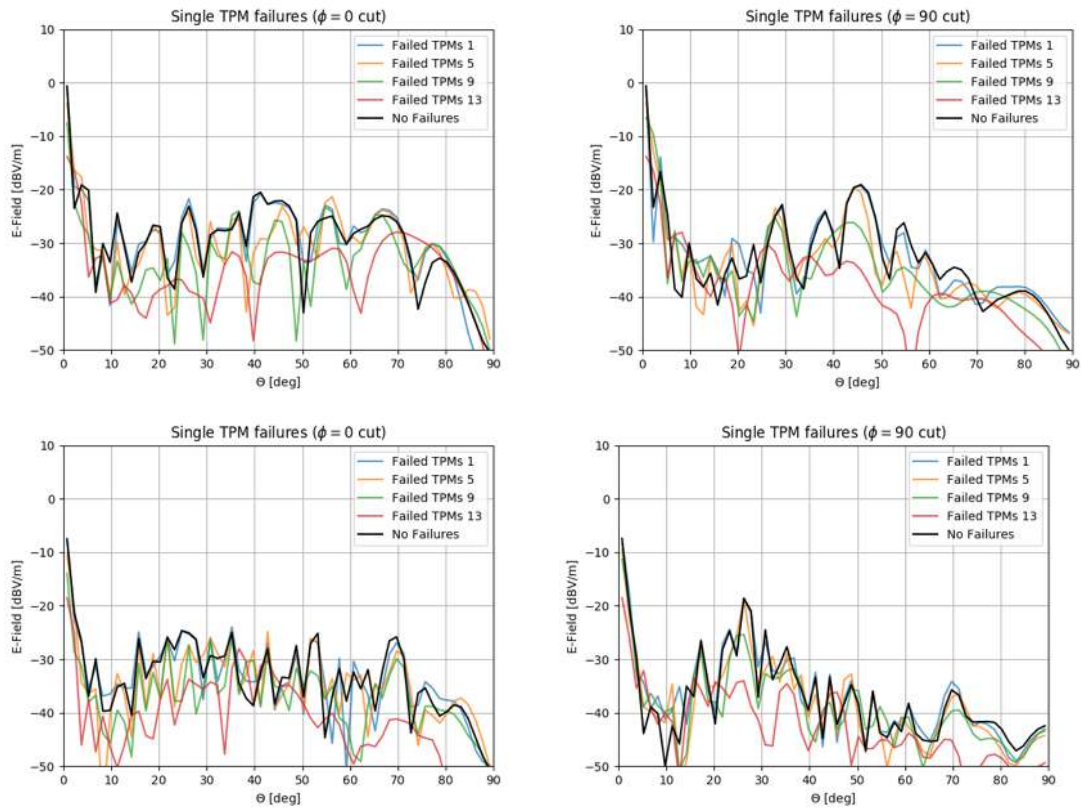


Figure 108: Station E-field beam cuts (in dBV/m) at 50 MHz (top row), 110 MHz, 220 MHz and 350 MHz (bottom row) for a $\phi = 0$ deg. cut and a $\phi = 90$ deg. Cut and a cumulative number of TPMs failing (0, 1, 5, 9, 13).

7.7.4 Random failing antennas.

The following plots show the impact of antennas failing randomly. We show the statistical impact on the effective area and sensitivity since the impact on the beam would be specific to the antennas failing. The results are the outcome of Montecarlo simulations with 1000 permutations.

7.7.4.1 Random failing 13 antennas (5% of a station)

A group of 13 randomly failing antennas on a station give the following performance:

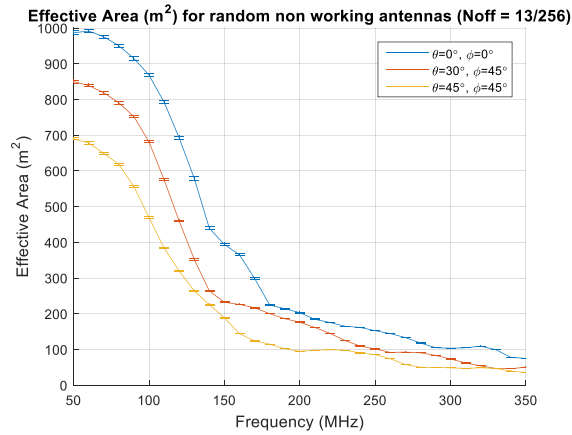


Figure 109: Loss of effective area for 13 random antennas failing. Simulations performed for an AAVS1 station (35m in diameter).

Calculated values of impact on sensitivity are available in Table 19.

7.7.4.2 Random failing 16 antennas

A group of 16 randomly failing antennas on a station would produce the following loss of effective area:

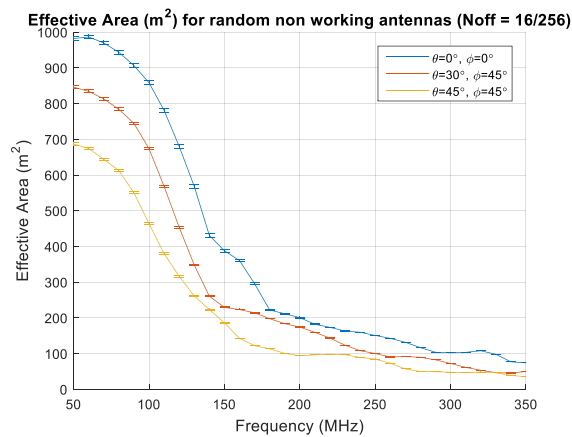


Figure 110: Loss of effective area for 16 random antennas failing. Simulations performed for an AAVS1 station (35m in diameter).

Calculated values of impact on sensitivity are available in Table 19.

7.7.4.3 Random failing 26 antennas (10% of a station)

A group of 26 randomly failing antennas on a station give the following performance:

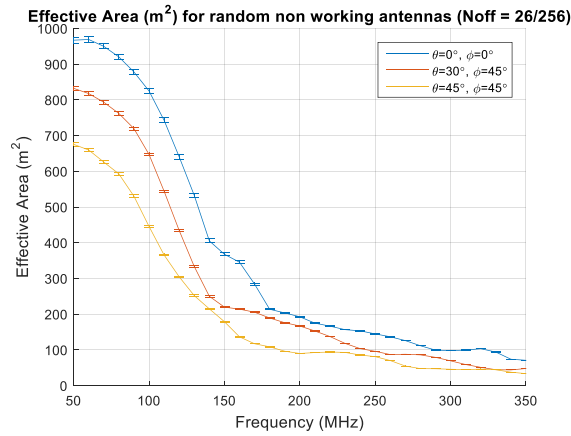


Figure 111: Loss of effective area for 26 random antennas failing. Simulations performed for an AAVS1 station (35m in diameter).

Calculated values of impact on sensitivity are available in Table 19.

7.7.4.4 Random failing 64 antennas (25% of a station)

A group of 26 randomly failing antennas on a station give the following performance:

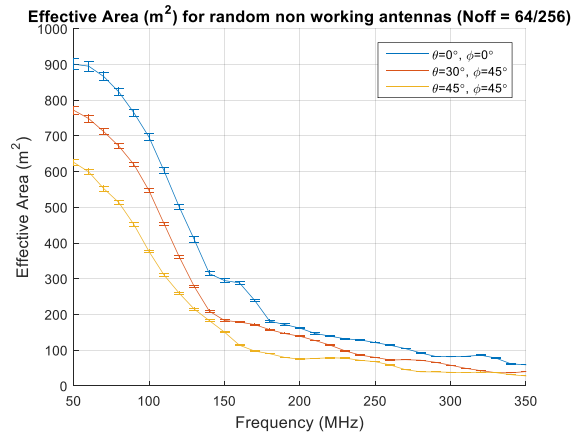


Figure 112: Loss of effective area for 64 random antennas failing. Simulations performed for an AAVS1 station (35 m in diameter).

Calculated values of impact on sensitivity are available in Table 19.

7.7.4.5 Summary table and effect on sensitivity.

The percentage impact on sensitivity converges to the percentage number of random failing antennas as we approach the high end of the frequency range. In this regime (sparse regime) the sensitivity is strongly dominated by the antenna sensitivity and the number of elements and thus this is expected. At lower frequencies (dense regime) the phased array behaviour has a stronger

impact and produces a sensitivity loss typically lower than the percentage of number of failing antennas. However, in the dense-sparse transition region, where the first grating lobes appear in the array factor, this percentage loss can be larger than the percentage number of antenna failures (see

Frequency (MHz)	Sensitivity - percentage error											
	Noff = 1		Noff = 16		Noff = 13 (~5%)		Noff = 26 (~10%)		Noff = 32		Noff = 64	
	Perc. err (0deg)	Perc. err (45deg)	Perc. err (0deg)	Perc. err (45deg)	Perc. err (0deg)	Perc. err (45deg)	Perc. err (0deg)	Perc. err (45deg)	Perc. err (0deg)	Perc. err (45deg)	Perc. err (0deg)	Perc. err (45deg)
50	0.14	0.15	2.29	2.45	1.85	1.99	3.80	4.05	4.76	5.07	10.39	11.09
60	0.16	0.19	2.55	3.12	2.05	2.50	4.27	5.21	5.31	6.47	11.58	13.88
70	0.18	0.25	2.97	4.15	2.39	3.36	4.97	6.84	6.19	8.48	13.35	17.78
80	0.22	0.30	3.65	4.82	2.95	3.92	6.04	7.90	7.52	9.81	15.97	20.23
90	0.29	0.33	4.62	5.43	3.74	4.41	7.61	8.89	9.42	10.98	19.56	22.37
100	0.36	0.36	5.80	5.81	4.72	4.73	9.46	9.50	11.67	11.69	23.56	23.60
110	0.47	0.34	7.43	5.64	6.05	4.58	11.98	9.21	14.68	11.35	28.67	22.98
120	0.58	0.33	8.90	5.44	7.27	4.41	14.21	8.89	17.32	10.98	32.84	22.30
130	0.62	0.34	9.69	5.40	7.93	4.39	15.35	8.85	18.66	10.93	34.87	22.23
140	0.60	0.34	9.27	5.54	7.57	4.49	14.75	9.06	17.98	11.15	33.82	22.63
150	0.51	0.37	7.90	5.90	6.44	4.80	12.68	9.64	15.54	11.86	29.97	23.89
160	0.38	0.39	6.22	6.26	5.04	5.08	10.12	10.20	12.48	12.55	24.94	25.11
170	0.36	0.39	5.85	6.31	4.75	5.15	9.54	10.25	11.77	12.61	23.69	25.18
180	0.34	0.41	5.59	6.45	4.53	5.24	9.16	10.47	11.32	12.87	22.92	25.67
190	0.36	0.41	5.78	6.55	4.69	5.33	9.43	10.62	11.65	13.06	23.54	25.97
200	0.37	0.40	6.02	6.36	4.89	5.16	9.80	10.35	12.06	12.74	24.23	25.41
210	0.37	0.40	5.98	6.39	4.85	5.18	9.77	10.36	12.03	12.74	24.16	25.43
220	0.38	0.39	6.12	6.18	4.97	5.03	9.94	10.04	12.23	12.35	24.56	24.74
230	0.37	0.39	5.95	6.13	4.82	4.98	9.68	9.98	11.93	12.29	24.02	24.69
240	0.37	0.38	6.02	6.12	4.88	4.96	9.80	9.95	12.06	12.27	24.27	24.60
250	0.39	0.39	6.12	6.20	4.97	5.03	9.92	10.08	12.21	12.40	24.51	24.82
260	0.41	0.39	6.37	6.25	5.17	5.08	10.34	10.15	12.73	12.50	25.37	24.99
270	0.41	0.40	6.53	6.41	5.32	5.20	10.57	10.39	12.99	12.79	25.84	25.47
280	0.41	0.40	6.56	6.43	5.33	5.23	10.63	10.44	13.07	12.83	25.96	25.56
290	0.40	0.41	6.40	6.48	5.20	5.27	10.40	10.52	12.79	12.94	25.50	25.76
300	0.39	0.40	6.31	6.39	5.13	5.19	10.27	10.38	12.65	12.78	25.27	25.46
310	0.39	0.39	6.28	6.19	5.10	5.03	10.21	10.08	12.56	12.40	25.13	24.82
320	0.40	0.39	6.41	6.26	5.21	5.08	10.39	10.16	12.78	12.50	25.49	25.01
330	0.40	0.39	6.47	6.20	5.27	5.03	10.49	10.08	12.91	12.41	25.70	24.82
340	0.38	0.39	6.19	6.23	5.02	5.07	10.06	10.14	12.38	12.47	24.79	24.96
350	0.40	0.39	6.34	6.28	5.15	5.10	10.31	10.20	12.69	12.56	25.30	25.11

** 0 and 45 deg refer to the pointing angles of zenith and (th=45Y,ah=45°) respectively

Table 19: Effect on sensitivity of random antenna failures

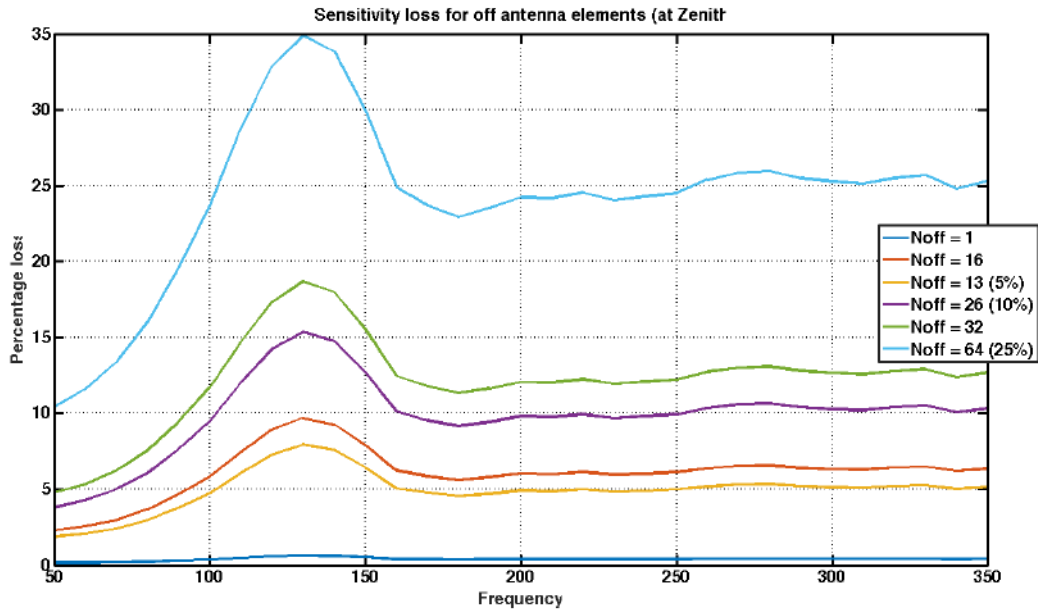


Figure 113: Loss of sensitivity for a single station for an increasing number of failing antennas. Zenith.

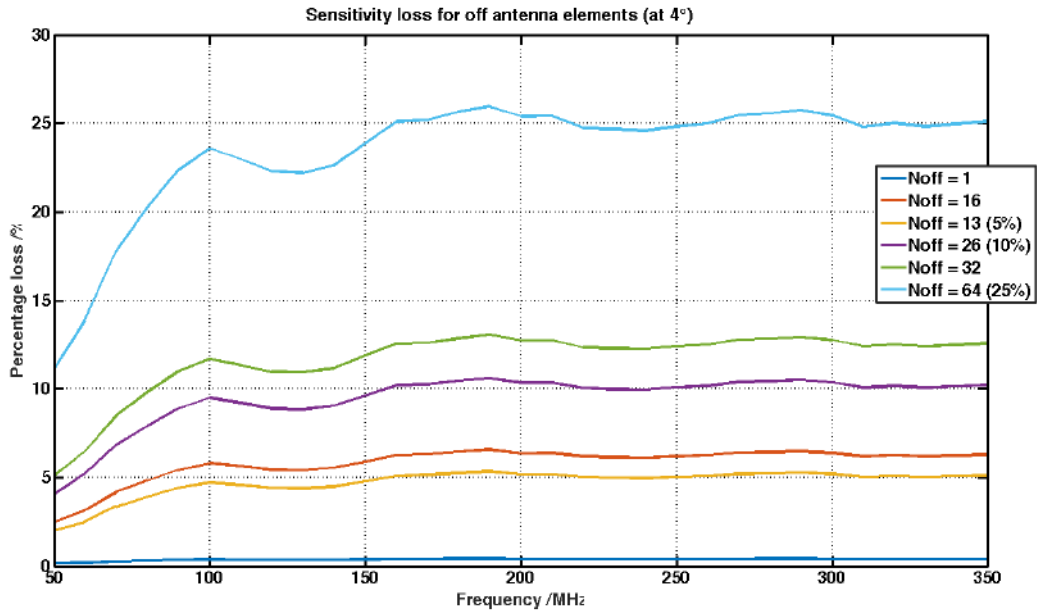


Figure 114: Loss of sensitivity for a single station for an increasing number of failing antennas. 45 deg. scan.

8 Measurements of the prototype arrays

The following subsections summarize the most relevant tests carried out with a 16-element SKALA2 array installed at the Mullard Radio Astronomy Observatory (MRAO) at Lords Bridge Cambridge in order to validate the designs and modelling of the array, antenna and front-end electronics. As per the antenna development plan [RD10], a SKALA4 array is being installed at the same location to repeat these tests. The tests carried out on this prototype followed from similar tests carried out on SKALA1 antennas. The system is equipped with an RF back end and TPM for signal processing.

8.1 AAVS0/Pre AAVS1

The AAVS0 (later called Pre-AAVS1) array (see **Figure 115**) was conceived as a test bed for the different technologies being developed for the aperture arrays that make the front-end of the SKA1-LOW instrument. This was the very first array built with LFAA technology, followed by the AAVS0.5 sister array in Western Australia. These include the antennas, LNAs, RFoF electronics and digital processing, but also the EM simulation software being developed for the project [RD31]. The AAVS0 is located at the MRAO at Lords Bridge and has 16 antennas arranged in a random configuration (see **Figure 118**:). The exact configuration of AAVS0, which is identical to the test array installed in Western Australia, has the same randomisation as the SKA1-LOW instrument.

The AAVS0 array is shielded from the soil by a 15 m diameter circular metallic mesh with a wire thickness of 2.5 mm and a pitch of 30 cm. The array processing back-end is located in a metallic hut, located 15 m from the edge of the ground plane. The close proximity of the hut intends to limit the length of the copper cables (2 per antenna) carrying power and RF signal. Both the metallic hut, the copper cables and the soil had to be included in the EM modelling in order to achieve good agreement between measurements and simulations at the low end of the frequency band.

An RF receiver chain was built for AAVS0. After the antenna and LNA, the 32 dual polarization signals were fed to the metal bunker using 30 m long coaxial cables. These signals were then terminated in pre analogue to digital (PREADU) boards which served the purpose of filtering and amplifying the signals as well as allowing a switched auxiliary noise input. The high RF environment at Lord's Bridge (see **Figure 116**) meant that FM filters had to be used to block the signal range 88-108 MHz, otherwise the receiver system would saturate. The total gain including the LNAs, could be modified from ~55 dB to ~85 dB in 0.5 dB steps with the PREADU gain range being nominally 12 – 43 dB. The output of the PREADU was filtered by 400 MHz anti-aliasing filters. Followed that a TPM is connected to process the signals from the 16 antennas, 2 polarizations.



Figure 115: AAVS0/PreAAVS1 array at Lords Bridge (MRAO, Cambridge, UK).

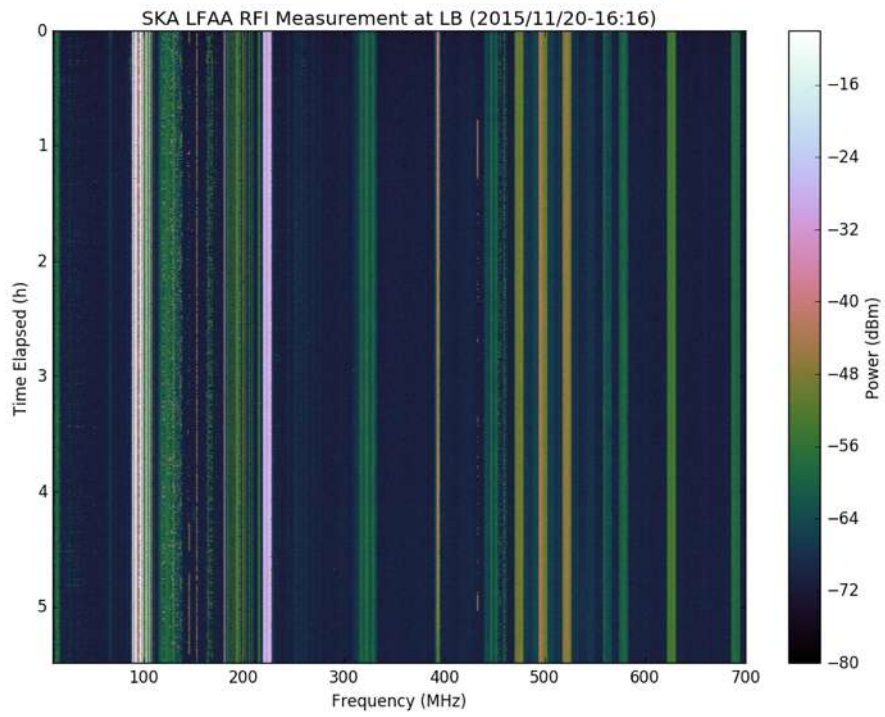


Figure 116: RFI waterfall plot at Lords Bridge (MRAO, Cambridge, UK).

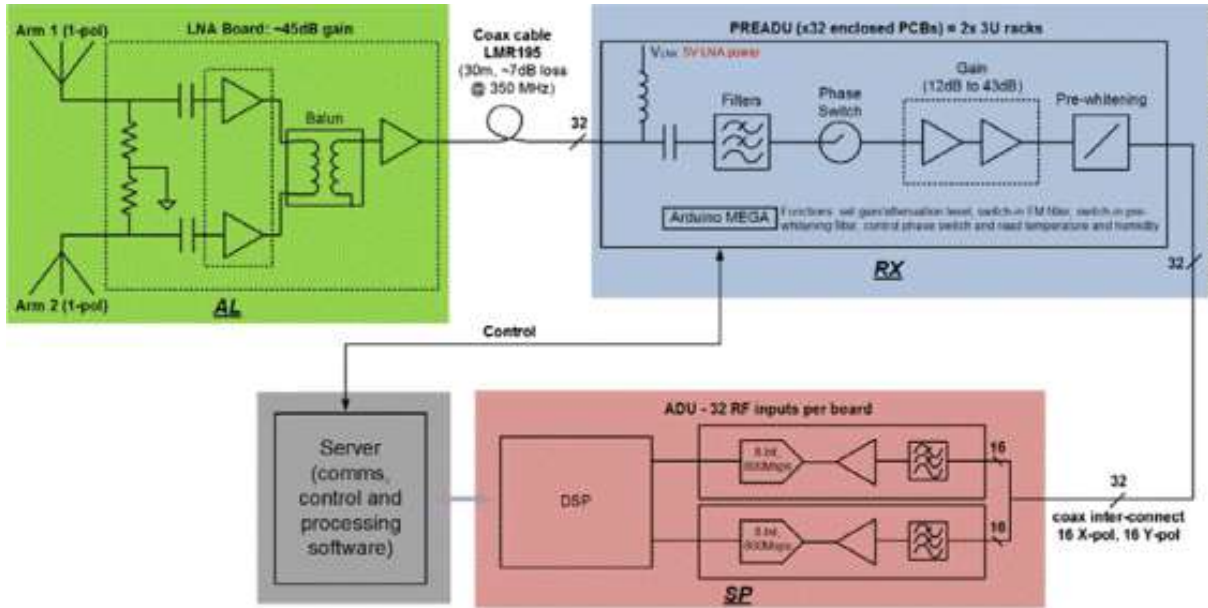


Figure 117: AAVSO receiver system (top) and PRRADU rack (bottom).

8.1.1 UAV measurements

Two extensive experimental campaigns have been carried out on the AAVSO and preAAVS1 array prototypes in September 2014 and 2016, respectively, in order to validate the computed radiation patterns (embedded-element and array). Both prototypes were composed of 16 antennas arranged in a random configuration (see **Figure 118**:). AAVSO was built with SKALA-1 antennas whereas SKALA-2 were featured in preAAVS1. The preAAVS1 system can be considered as a fully-operational subarray of both AAVS1 and an SKA1-LOW station.

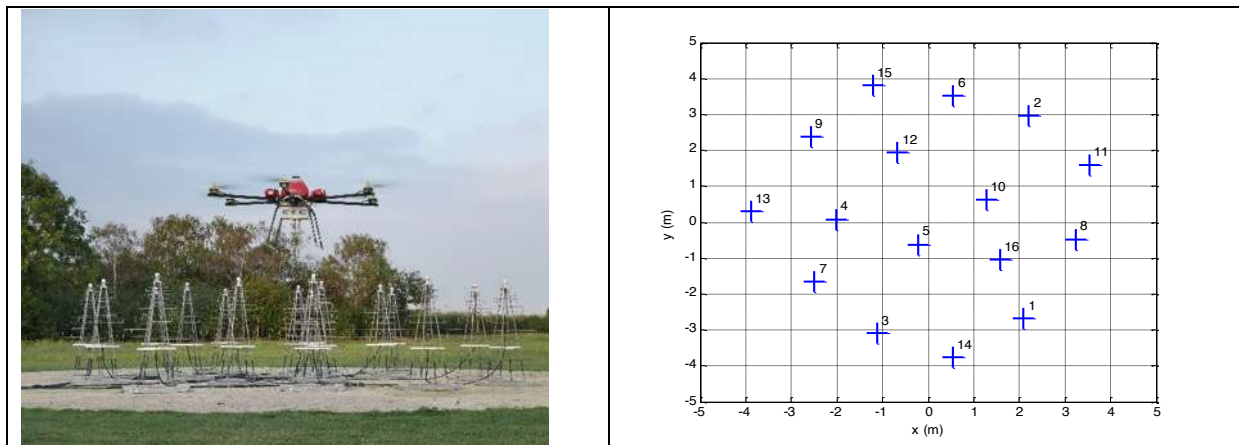


Figure 118: (left) UAV flying over the preAAVS1 array (SKALA-2 antennas), deployed at the Mullard Radio Astronomy Observatory, Lords Bridge, Cambridge. (right) Array geometry of both AAVS0 and preAAVS1.

A UAV-mounted test source (also visible in **Figure 118**;) has been exploited to perform end-to-end tests on the aperture array prototypes. It is based on a commercial hexacopter, which is equipped with RF devices such as a synthesizer, a balun and a dipole antenna (length is selected according to the specific test frequency). After the take off, the UAV follows an autonomous GPS-guided navigation according to a pre-programmed flight path. During the both the AAVS0 and preAAVS1 campaigns, this task has been accomplished performing constant-height flights at 100 m and 150 m for the operative frequencies 50-250 MHz and 350 MHz, respectively, in order to satisfy the far-field condition. The UAV position is measured using a differential GNSS system which provides an accuracy of 2-3 centimeters. Its three-axis orientation is measured by the onboard Inertial Measurement Unit with an accuracy of about 2 Degrees.

It should be noted that this UAV-based test methodology has some advantages with respect to astronomical tests. First of all, the transmitted RF power is sufficient to measure the embedded-element pattern of each array element with a very high signal-to-noise ratio. Moreover, arbitrary scan strategies can be performed in order to completely map the radiation patterns in the overall hemispherical region. Both co- and cross-polar data can be collected (the source is linearly-polarized). Finally, such an RF test source with known position in the sky can be used to both verify the time delay of digitized data [RD46] and perform the array calibration (both magnitude and phase) [RD45].

The results of AAVS0 are extensively discussed in [RD18],

The most interesting results of the preAAVS1 campaign are reported in Figure 119:. These results have been obtained from a linear scan along the x-axis (see **Figure 118**;), which corresponds to the H-plane of the dipoles oriented along the y-axis. The time series acquired with the digital back-end (for each element) have been equalized at zenith in both magnitude and phase to perform the array calibration . The effects of path loss and test source radiation pattern have been removed according to [RD47]. The extracted embedded-element patterns have been normalized to 0 dB at zenith in order to compare the simulated (blue) and measured (red) beam patterns to the array factor (dashed green). There is good agreement between measurements and simulations. In the main beam region, the discrepancy is lower than 0.3 dB . The only significant discrepancy is observable on

the second sidelobes at 350 MHz (right) around $\pm 20^\circ$ from zenith. This can be due to element positioning errors that are not taken into account in the simulations. Measured element positions acquired by means of aerial photogrammetry [RD18] could be adopted to further improve the models.

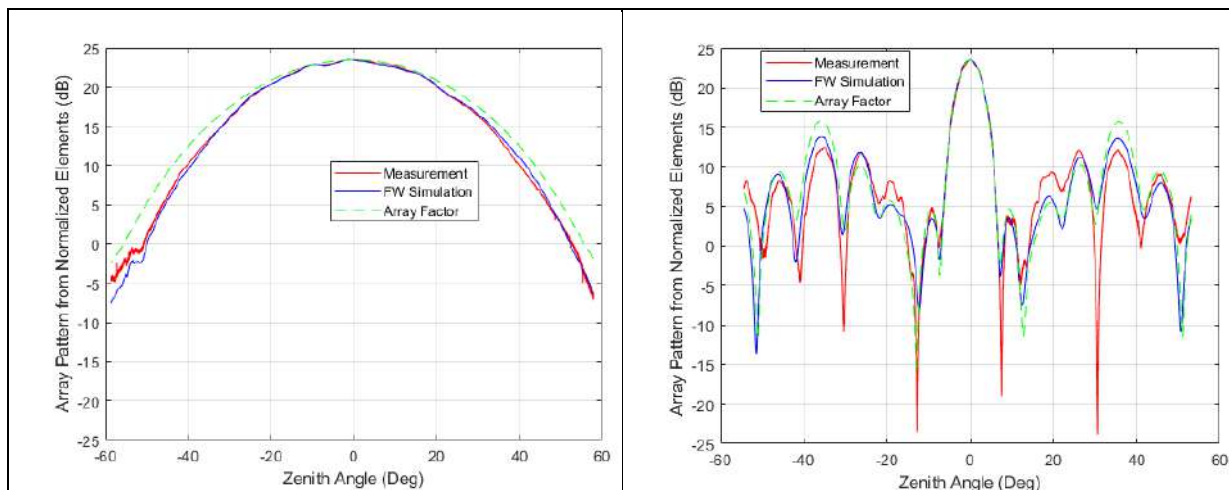


Figure 119: PreAAVS1 array (beam) patterns at 50 MHz (left) and 350 MHz (right).

An example of embedded-element pattern at 350 MHz is presented in Figure 120: for the central antenna (#5, see **Figure 118**;) of the preAAVS1 array. Both E- and H-plane are shown in the left and right pictures, respectively. Two different scans (labelled as TW1 and TW2 for E-plane and TW3 and TW4 for the H-plane) are reported in order to show the high repeatability of the measurement. The black and cyan solid (dashed) curves represent the co-polar measurements (simulation) for the two scans. The magenta and green colours are instead used to represent the cross-polar data.

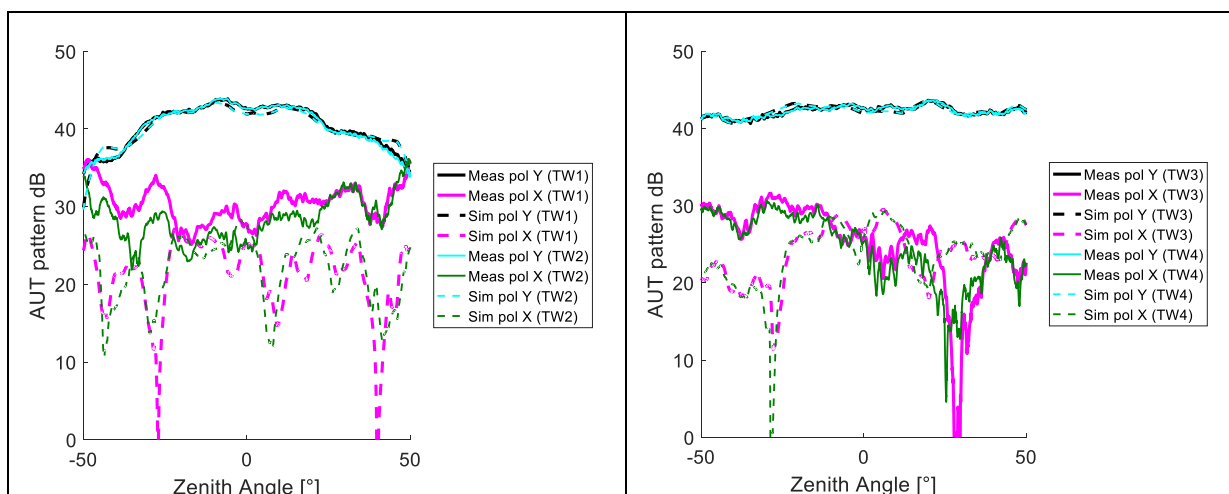


Figure 120: Embedded-element patterns of the central element (#5) of the pre AAVS1 array. Two different scans are shown for each measurement plane: E-plane (left, TW1 and TW2) and H-plane (right, TW3 and TW4).

The measured embedded-element patterns also include the LNA Gain. These are absolute measurements that have been obtained by normalizing the acquired time series with respect to a reference measurement. Such a reference measurement has been performed connecting the RF synthesizer (mounted on the UAV) to the inputs of the receiver [RD48] by means of a known attenuator. In this way, the contributions of the transmitter power, the receiver and digital back-end

gains have been calibrated out. A constant gain of about 37.7 dB has been added to the antenna simulation in order to fit the measured levels. This value is consistent with the combination of LNA Gain and cable attenuation.

As far as the co-polar measurements are concerned, the discrepancy between measurement (solid line) and simulations (dashed line) is generally within 1 dB. The cross-polar measurements show a higher discrepancy with respect to the corresponding simulations due to the geometrical uncertainties of both the AUT and the test source with particular reference to a) the AUT angular position accuracy on the measurement field, b) the alignment of the source dipole on the UAV, c) limited accuracy of the UAV orientation measured by the on-board Inertial Measurement Unit, which is in the order of 2° as mentioned above.

In this campaign we were also able to measure the near field phase of the embedded beams using a reference antenna outside of the array (see Figure 121). More information available in [RD49].

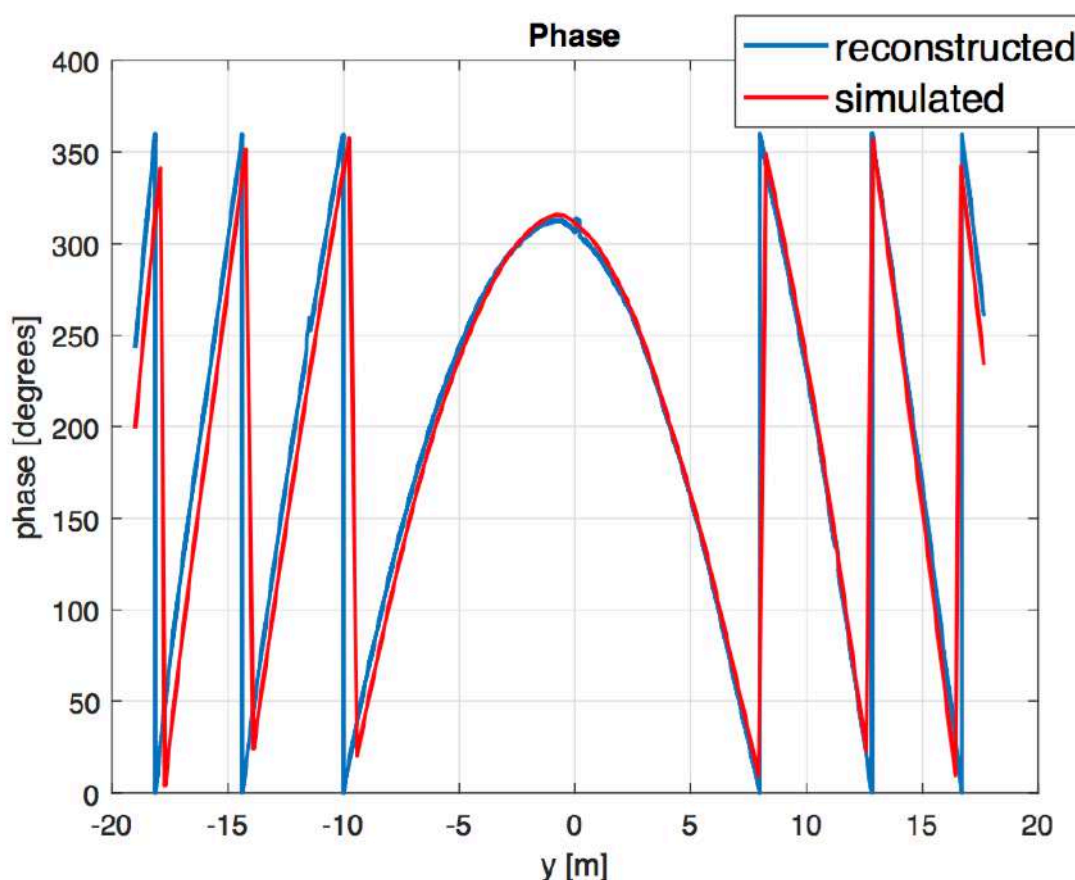


Figure 121: Reconstructed (blue curve) and simulated phase (red curve) of y-component of the AUT near-field along the UAV trajectory.

During a preparatory phase for the preAAVS1 campaign, radiation pattern test on an isolated SKALA-2 antenna were performed in Turin using two spectrum analysers as narrow band receivers. Two result examples are shown in Figure 122: . The scan direction is parallel to one of the two antenna dipole directions. At 50 MHz (left figure) the radiation pattern for the two orthogonal elements exhibit similar levels owing to the polarization rotation at low frequencies of SKALA-2 (see [RD18] for

more details on this aspect). This polarization rotation is no longer present in SKALA-4 owing to the closed-boom design. The rotation is less significant at 350 MHz (right), therefore, a cross-polar separation level of more -15 dB can be observed.

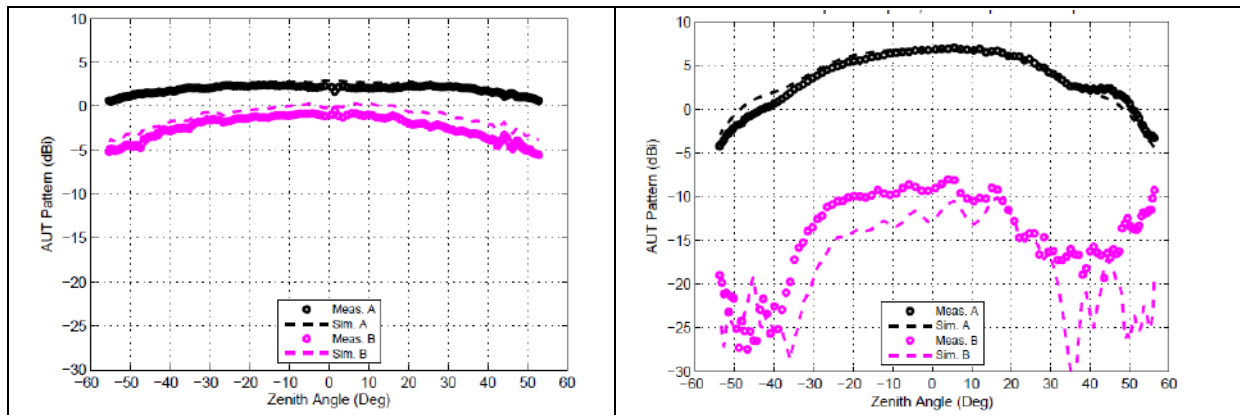


Figure 122: Radiation pattern measurements of an isolated SKALA-2. A (black) and B (magenta) refer to the two antenna ports. Measurements are shown with circular markers, simulations are shown with dashed line. (left) 50 MHz (right) 350 MHz.

The error levels are similar to the ones presented above. It should be noted that the overall cross-polar pattern shape is very consistent between measurement and simulations.

In an earlier campaign [RD18] we were able to explore the effects of phase calibration on the array beam. In the figure below we can see the effect of not doing a phase calibration in the beam. As expected [RD16], this has an effect mainly on the inner side lobes ("coherent" side lobes), while the main beam is almost unaltered as well as the far out side lobes. The rule of thumb is that the number of side lobes belonging to the inner "coherent" region is $\sim \sqrt{N/\pi}$ with N the number of elements in the array.

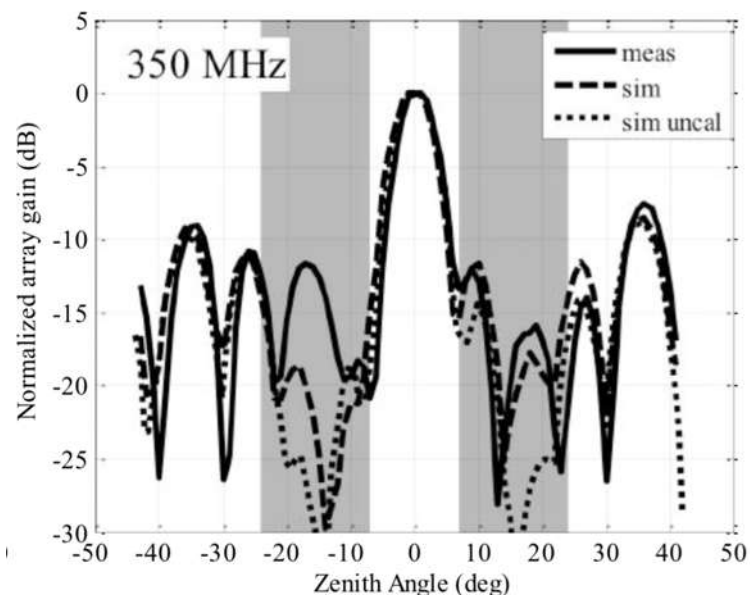


Figure 123: Measurement and simulation of a AAVSO beam cut (with and without phase calibration).

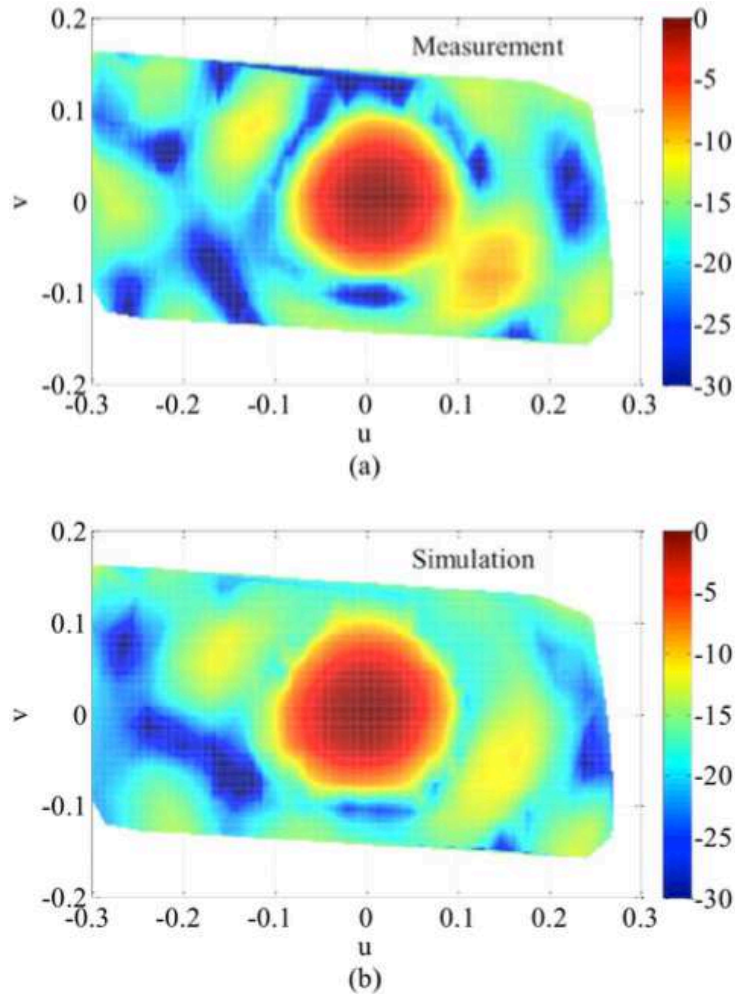


Figure 124: Measurement and simulation of the 2D AAVSO array beam when scanned at zenith.

In conclusion, the consistency between simulations and measurements has been verified at single-element, embedded-element and array levels from 50 to 350 MHz. The experimental embedded-element and array patterns have been measured on a fully-operative system which is a subarray of an SKA1-LOW station.

8.1.2 Satellite measurements

The experiment observed single carrier transmissions from the CASSIOPE satellites (nominal carrier frequency of 150.012 MHz) with help of a spectrum analyser over the combined signal of a single polarisation from the 16 element array. After Doppler shift and free space path loss corrections the main lobe of the array pattern is compared to our simulations. Ionospheric propagation effects were neglected in our study and need further investigation.

The first important thing to do when dealing with beam characterization using satellites is to gain enough knowledge about the satellite's transmission and passes. We did observe several satellites (see **Figure 125**) until concluding that the most stable and predictable was the CASSIOPE satellite.

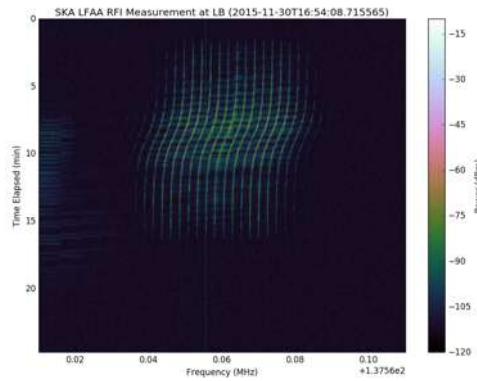


Figure 125: Spectra for a NOAA satellite pass. The signal itself is a 256-level amplitude modulated 2400Hz subcarrier, which is then frequency modulated onto the 137 MHz-band RF carrier. Maximum subcarrier modulation is 87% ($\pm 5\%$), and overall RF bandwidth is 34 kHz. On NOAA POES vehicles, the signal is broadcast at approximately 37dBm (5 watts) effective radiated power.

In **Figure 126** we can see the results for a satellite pass over the AAVS0 array. In the bottom central plot we can see the comparison with simulations showing very good agreement in both the main beam and side lobes.

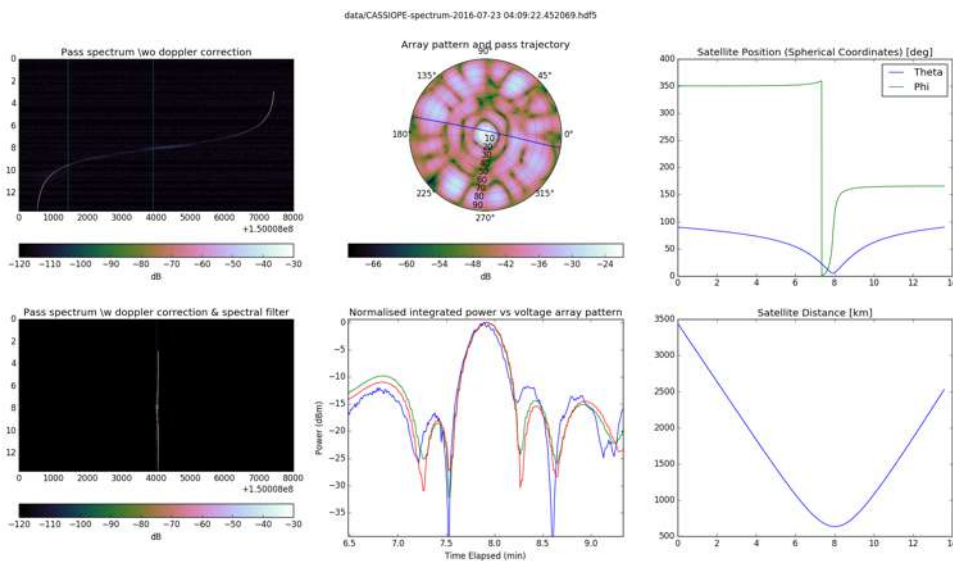


Figure 126: Array beam and satellite data (CASSIOPE satellite). Left column: power spectrum before (top) and after (bottom) Doppler correction, Central column: Satellite pass over the simulated array beam (top) and beam cut measured (blue line) and simulated with 2 different solvers (red and green lines) (bottom), Right column: satellite position (top) and distance to the array (bottom).

Using multiple satellite passes (see **Figure 127**) one can also construct a 2D array beam. This however takes a considerable amount of time until enough passes over the central region of the beam can be obtained.

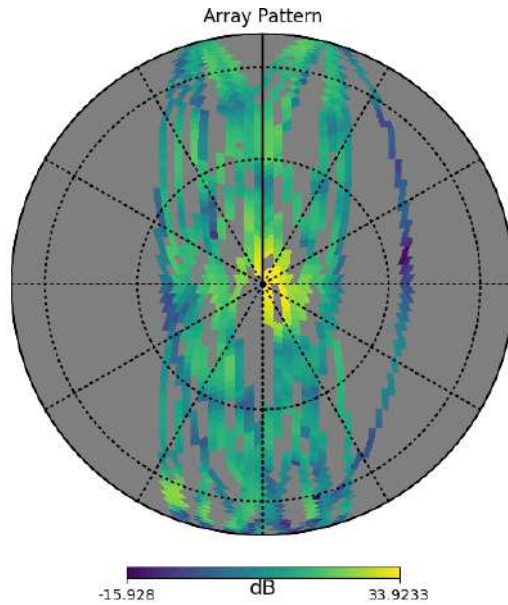


Figure 127: 2D Array beam measured with multiple CASSIOPE satellite passes.

8.1.3 Direct coupling measurements

One of the most revealing measurements to validate electromagnetic simulations is the measurement of the coupling coefficients. Our tests have indicated a very good agreement between simulations and measurements for closely located antennas. This confirms the accuracy of the electromagnetic simulations and their ability to predict the systems performance.

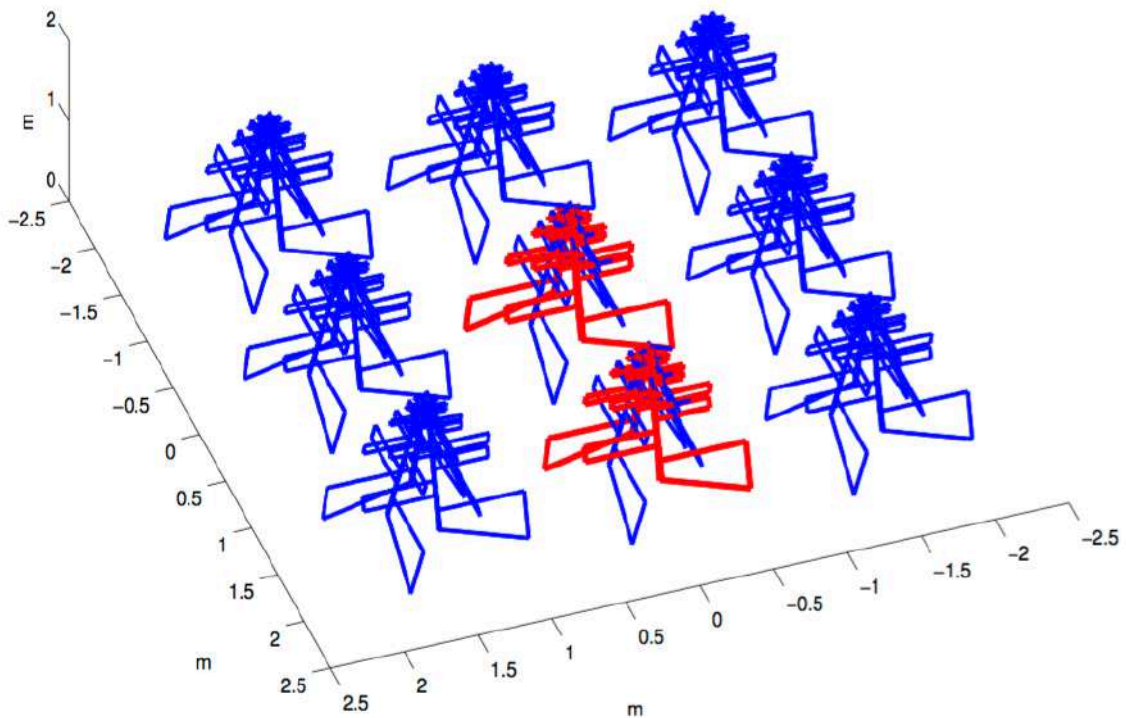


Figure 128: AAVSO array configuration for coupling measurements.

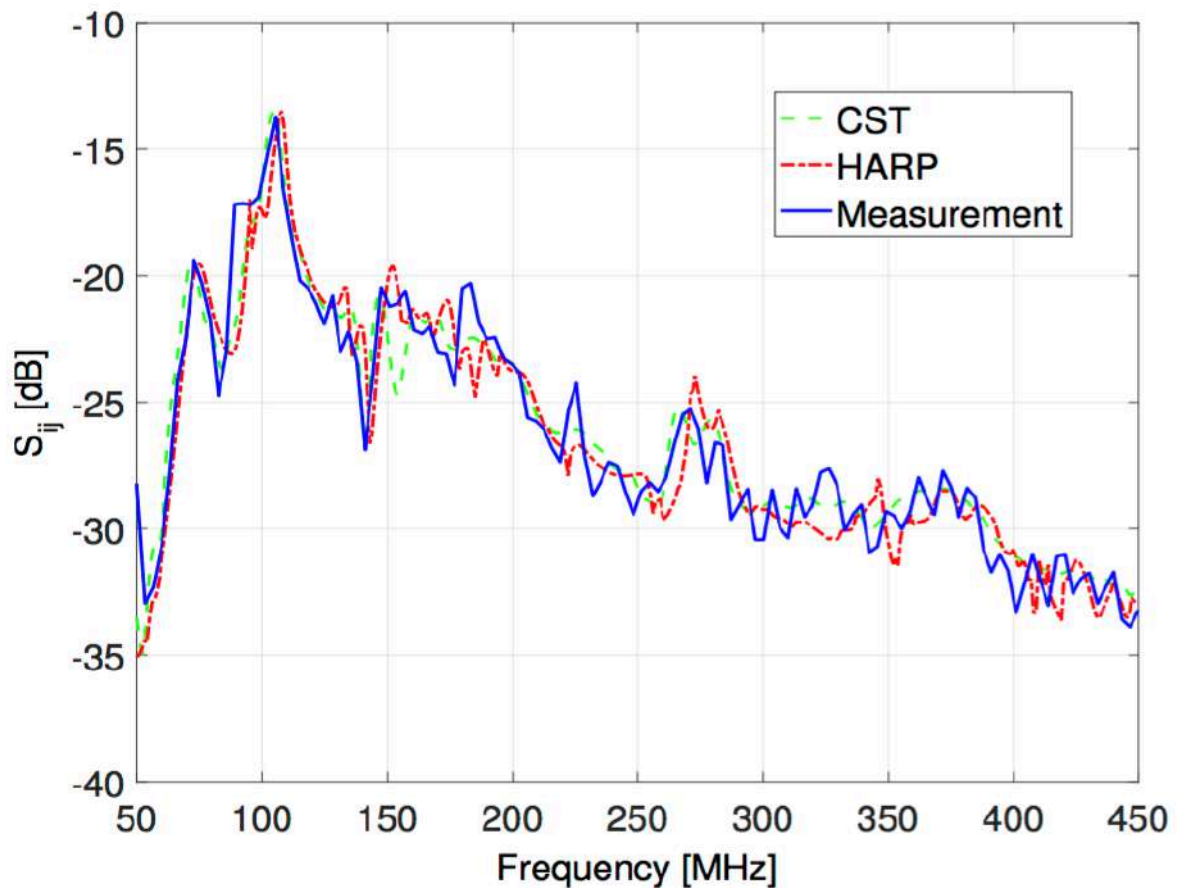


Figure 129: Measured vs simulated coupling using commercial (CST) and in-house (HARP) codes.

8.1.3.1 Other measurements and conclusions

Other measurements of AAVS0 include further drone tests performed by the Chinese KLAASA team [RD50], further coupling and near field measurements [RD51] and polarization measurements using a fix artificial overhead source [RD52] amongst others.

Several other measurements have been done on other prototype arrays, such as the AAVS05 array in Western Australia. Those are described in [RD44] and show good agreement in the sensitivity measurements with the simulations as well as also in array beam measurements. More information on prototype measurements can be found in the AAVS1 demonstrator test report [RD4]. Currently, the AAVS1 prototype station is under commissioning and results are expected soon to complete those presented here.

All these measurements demonstrate our ability to both predict and measure in the field the performance of SKA1-LOW like arrays, including the effects of mutual coupling. Further work shall take place however on continue the improvement of the simulation, modelling and measuring techniques for SKA1-LOW size stations during the construction and commissioning phases of the instrument.

9 Layouts

All the 512 station layouts can be found in the *Antenna engineering data pack / Array folder* attached to this document set.